Magnetostrictive Patches for Guided Wave Inspection of Composites

by

Akram Zitoun

Submitted to the University of Warwick

for the degree of

Ph.D in Engineering

School of Engineering

March 2022

Table of Contents

Chapter 7: Defect detection in composite structures using magnetostrictive patch transducers

List of Figures

Chapter 1:

Chapter 2:

Chapter 3:

Chapter 4:

Chapter 5:

Chapter 6:

Chapter 7:

List of Tables

Acknowledgments

The work reported within this thesis has received funding from the European Commission under the ITN project “NDTonAIR”. My greatest thanks go to the project managers Professor Marco Ricci and Dr. Stefano Laureti for their support, help and insights that greatly helped delivering the outcomes of the project.

I would like to share my greatest honour to being able to work under the supervision of Professor David Hutchins and Professor Steve Dixon. I would like to express my deepest gratitude for their continuous and unconditional support throughout my PhD. Both professors contributed to the successful outcome of the project and the PhD and during the writing of the thesis.

I would like to thank Mr. Graham Edwards at TWI for his supervision while conducting experiments and guiding me to improve my workflow through his vast knowledge.

I would like to express my greatest gratitude and thanks to my parents Khaled and Zina, to my wife Sarra, my brother Oussama and my baby girl Leen for their patience, overwhelming love and support along the full period of me working on the PhD. They were there during my most difficult times providing me with emotional support to overcome all the stress and tears throughout this journey.

Declaration

The research presented in this thesis is my original work, produced under the supervision of Prof. David Hutchins in School of Engineering and Prof. Steve Dixon in the Department of Physics at the University of Warwick, UK, between January 2018 and March 2022. No part of this work has been previously submitted to the University of Warwick, nor to any other academic institution for the purposes of obtaining a higher degree.

Publications arising from the research

[1] Zitoun, A., Dixon, S., Edwards, G. and Hutchins, D., 2020. Experimental Study of the Guided Wave Directivity Patterns of Thin Removable Magnetostrictive Patches. Sensors, 20(24), p.7189.

[2] Zitoun, A., Dixon, S., Kazilas, M. and Hutchins, D., 2022. The Effect of Changes in Magnetic Field and Frequency on the Vibration of a Thin Magnetostrictive Patch as a Tool for Generating Guided Ultrasonic Waves. Sensors, 22(3), p.766.

[3] Zitoun, A., Hutchins, D., Dixon, S. and Kazilas, M., 2022. Defects detection in composite structures using magnetostrictive patch transducers. NDT&E International, 2021 (Draft finalized)

Thesis Summary

The work conducted within this PhD investigated the general characteristics of removable magnetostrictive thin patches for the generation of guided waves in plates that can be used for defect detection in composite structures. Initial experiments measured the directivity of SH, S0 and A0 guided waves modes in a metallic plate while varying the applied static and dynamic magnetic fields. Multiple coil geometries and permanent magnets were used to vary the field parameters, so that both Lorentz and magnetostrictive forces could be created. It was demonstrated through this initial testing that guided waves patterns could be controlled by careful control of these parameters.

Experiments were also conducted to investigate the vibrational characteristics of the magnetostrictive patch itself for variations in both the static and dynamic magnetic fields and the excitation frequency. It was demonstrated that the vibrations within the patch could be controlled and enhanced by varying the excitation frequency and by varying the direction and amplitude of the applied magnetic fields. Another finding was that for low frequencies, the natural frequency of the patch can contribute to the vibration enhancement. However, for higher frequencies of up to 250 kHz, it was shown that the magnetostriction is the main transduction mechanism generating vibrations within the patch.

Finally, the magnetostrictive patch was used to inspect a lab-induced defect in a CFRP sample and then a delamination within a GFRP plate. The optimised excitation parameters were then used to generate guided waves within these composite samples, and images of the defects produced using the synthetic aperture focusing technique (SAFT) for image reconstruction.

List of Abbreviations

AC: Alternating Current
CFRP: Carbon Fibre Reinforced Polymer
DAQ: Data Acquisition System
DC: direct current
EC: Eddy Current
EDX-A: Energy Dispersive X-Ray Analysis
EMAT: ElectroMagnetic Acoustic Transducers
FeCo: Iron Cobalt
FFT: Fast Fourier Transform
GFRP: Glass Fibre Reinforced Polymer
GW: Guided waves
MFL: Magnetic Flux Leakage
MFL: Magnetic Flux Leakage
MPI: Magnetic Particle Inspection
MPTs: Magnetostirctive Patch Transducers
NDE: Non-Destructive Evaluation
NdFeB: neodymium-Iron-Boron
NDT: Non-Destructive Testing
PPM: Periodic permanent magnet.
PTFE: Polytetrafluoroethylene Polymer
PZT: Lead Zirconate Titanate
RF: Radio Frequency
SAFT: Synthetic Aperture Focusing Technique
SEM: Scanning Electron Microscope
SH: Shear Horizontal
SNR: Signal to Noise Ratio
TOF: Time of Flight
TOFD: Time Of Flight Diffraction
UT: Ultrasonic Testing

List of Symbols

μ	Shear modulus (chapter 1), micro (Remaining Chapters)
λ	Wavelength (Chapter 1), Magnetostriction (Remaining Chapters)
ρ	Material density (chapter 1), charge density (chapter 2)
C_L	Bulk longitudinal wave velocity
C_T	Bulk transverse or shear wave velocity
ω	Angular frequency
h	Plate half thickness
k	Wave number
C_p	Guided waves phase velocity
C_g	Guided waves group velocity
n	Mode number
f	Frequency
d	Plate thickness
$\vec{D}$	the electric displacement vector
$\vec{B}$	Magnetic field vector
$\vec{E}$	Electric field vector
$\vec{H}$	Magnetic strength
$\vec{J}$	Current density vector
σ	Electrical conductivity
ϵ_0	Permittivity in free space
ϵ_r	Relative permittivity in material
μ_0	Permeability in the free space
μ_r	relative permeability of a specific material
$\vec{F}$	Lorentz forces vector
q	Electric charge
$\vec{\vartheta}$	vector of the velocity of a charged particle
m	Mass of an electron
e	Electric charge (chapter 2), Strain (Chapter 3)
τ	Time period
$\overrightarrow{\vartheta_{\imath}}$	Velocity vector of an ion
$\vec{F}_M$	Magnetisation forces vector
$\vec{n}$	Out-of-plane direction unit vector
M_n	Magnetisation vector component in the normal direction
i, j	Integer indices when used in index notation
$\vec{M}$	Magnetisation
λ_s	Saturation magnetostriction
$\delta l, \Delta l$	Fraction of changes in length
l	Length
θ	Angle indication
χ	Magnetic susceptibility
λ_0	Spontaneous magnetostriction

$\lambda_{s\parallel}$	magnetostriction parallel to the main alignment direction
$\lambda_{s\perp}$	the magnetostriction perpendicular to the main alignment direction
α_i, β_i	cosine of directions as per equation 3.12
Ω	Ohm symbol
$\lvert A\rvert, Mag_V, magnitude\ \vartheta_i$	Magnitude of a vector
A	Vector potential of the magnetic field – modelling
V	Potential scalar of the electric field (elsewhere), Vanadium (chapter 6)
d_{HT}^{T}, e_{HS}	Peizomagnetic matrices
c_H	Stiffness Matrix
s_H	Compliance matrix
e, ε	Strain generated through magnetostriction transduction mechanism
∇^{*}	Nabla operator
∇	Gradient operator
∇x	Curl operator
$\nabla.$	Divergence operator
$\otimes$	Matrices product symbol

Chapter 1: Introduction

1.1. Motivation

Non-Destructive Testing (NDT), also known as Non-Destructive Evaluation (NDE), is an inspection and quality checks method used across different sectors of industry [1, 2] such as in aerospace, automotive and renewable energy. Such testing is needed as it is important to detect defects and flaws early, in order to avoid major failures. This is especially the case for safety-critical equipment. NDT techniques are used in a wide range of industries, including construction, manufacturing, oil and gas civil infrastructure, power generation, transport and aerospace. A structural or mechanical failure of a component or structure in any of these industries might have significant economic impact but could also endanger human life. By implementing NDT either in the manufacturing process or in-service, the safety and the reliability of the component is improved. Early detection of failure may also reduce downtime for repairs and decrease maintenance costs.

NDT can provide key information related to the health of the component and the presence of any defects, whose type, size and probability of detection will be assessed. In the process of NDT, the results are gathered typically via the transducers that are used during the test. These transducers can be different based on the testing being conducted, such as coils for eddy current testing or piezoelectric transducers in the case of ultrasonic testing or guided waves inspection. It is necessary that these transducers are studied and developed, so that a good understanding is obtained of how they operate and how their sensing capabilities can be optimized.

Among the ultrasonic sensors used in NDT, piezoelectric transducers (often using PZT (lead zirconate titanate) active elements) are very common because of their advantages: simplicity of use, high signal to noise ratio, and the ability to generate relatively high amplitude ultrasonic waves [1]. However, this type of sensor requires coupling to the testing specimen through a coupling agent, which limits the applications in which they can be used, e.g. in high temperature environments [2]. Another drawback is that the PZT is commonly designed and optimized for specific frequencies, and is often limited in terms of frequency range that can be used to test for defects.

In order to overcome these disadvantages, interest has been directed toward contactless ultrasonic sensors for NDT. Examples of non-contact NDT techniques include laser-based sensors and Electromagnetic Acoustic Transducers (EMATs) [1,3] which can be used for high temperature inspection [4]. One limitation of these sensors is the requirement for an electrically conductive specimen or a specimen that has a coating of a magnetostrictive material, such as magnetite (iron oxide) found on high temperature pipework. More details of EMAT design, construction and performance are given in Chapter 2. The ability to inspect non-conducting samples using components similar to those used in EMATs will be the main subject of study in this thesis, via the magnetostriction effect. Particular emphasis will be on the inspection of composite samples such as those used in the aerospace industry.

1.2. Common Non-Destructive Testing (NDT) techniques

There are numerous NDT techniques used to assess safety critical components without damage [5, 6]. The components can be monitored and inspected either while in service or during manufacture. The idea behind performing such tests is to ensure that the component is functioning safely, and that the possibility of failure during service is minimised. NDT is commonly used for defect detection [7,8], defect classification and thickness gauging [9, 10]. In addition to ultrasonic testing, other common techniques include visual inspection, radiography, thermography and electromagnetic testing methods [11]. Each technique is suitable for a limited number of applications. Some are sensitive to surface defects, including visual inspection, magnetic particle inspection (MPI) or magnetic flux leakage, while are others are suited for detection of defects inside the material itself (e.g. thermography). It is of interest to briefly discuss some of these methods.

1.2.1. Visual and optical inspection

Visual inspection is considered the oldest and most basic NDT technique [12]. However, a qualification process and proper training are required in order to consider the results reliable and to correctly assess the health of any components [11]. This method is deemed to be the first choice when a quick and simple inspection is required.

The defects that can be detected should be surface defects with a moderate size. The surface should be cleaned and prepared to avoid wrongful interpretation and understating of the output of the inspection. Although visual inspection is easy and rapid, it has many disadvantages. It is limited in terms of the type of the defect that can be detected (typically the defect must be at the surface for an opaque sample). The technique itself is highly dependent on human factors which decreases the repeatability significantly.

As part of the visual inspection methods applied in NDT, dye penetrant inspection [13] is an advanced and established visual technique. It is often using fluorescence substance applied to the surface being inspected to reveal defects. This technique is slightly different from conventional visual inspection as it uses an additive that needs to be applied to the surface of the tested structure. Surface preparation is necessary and it has difficulties when the surface is rough or where there is paint or a coating present. It is also dependent on the operator which limits the repeatability [14].

1.2.2. Radiography

The radiography technique is a widely-used technique in NDT, especially for thick metallic components [15]. Radiography involves the use of typically either an X-ray or a γ-ray source, where radiation travels through the material of the specimen. The transmitted energy is then captured using either a radiographic film or, more recently, a digital imaging system. A sketch of the experimental configuration used to perform radiography is shown in figure 1.1.

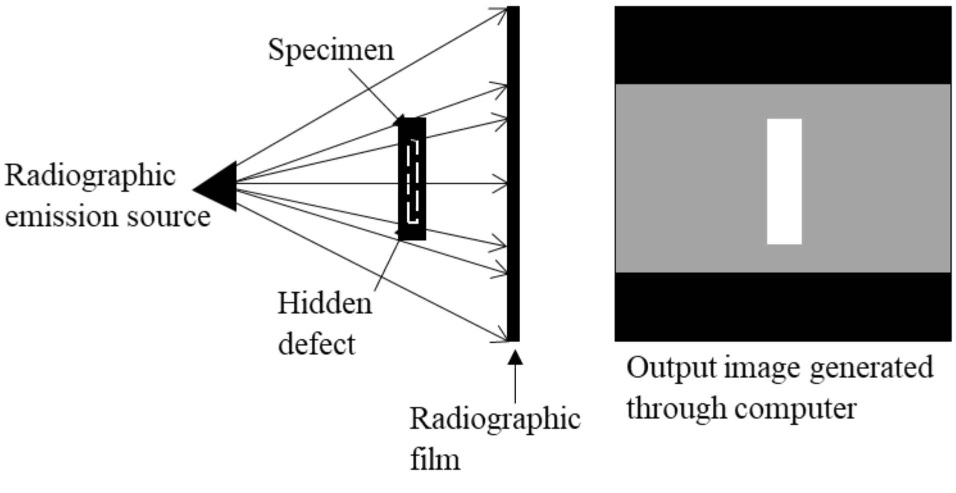

Figure 1.1. *Diagram of the experimental apparatus used for radiography*

Radiography is based on absorption of the emitted signal, and the recorded image represents the attenuation levels of the energy projected on the film [16,17]. In fact, the energy level at the film would be altered if passing through a defect, and thus different colour nuances on the same image would reveal the defect size and location. The selection of which type of radiographic source to use is related to the penetration required, with γ-rays being of higher energy than X-rays. This method is easy to use, and the operator has significant control of the process [18,19]. A radiography test requires a highly qualified operator to ensure a high level of safety due to the use of ionising radiation, and this sometimes restricts its use in an industrial setting [20]. Furthermore, the equipment used for radiography is expensive, and interpretation of images can sometimes be difficult [18, 19].

1.2.3. Active and Passive Thermography

Thermography is a well-developed technique in NDT and attracts both research and industrial interest. In fact, thermography consists of using a source to generate thermal energy which propagates within the inspected structure. The propagation of the energy is conducted through diffusion. This technique proved its efficiency in detecting internal flaws in a component while scanning large areas as defects were detected at a depth of 1mm with a dimeter ranging from 0.25 to 30 mm both in steel and in carbon fibre reinforced polymers samples [7]. The thermal energy would interact with the defect as a thermal gradient is noticed due to the differences of the thermal coefficients between the defect area and the material. This gradient is used to evaluate the defect.

Thermography is widely used to inspect layered structures such as composite materials. It is used to detect delaminations [21] or damage that has occurred following an impact, which is particularly of interest to the aerospace industry [22]. Active thermography uses external heating sources such as lamps to generate thermal changes within the sample. Resultant surface temperatures can then be detected as a function of time using an infra-red camera, allowing defects to be revealed. A typical measurement is shown in Figure 1.2, where the active heating is performed by placing a heat lamp as shown, and then monitoring the change in temperature at the surface.

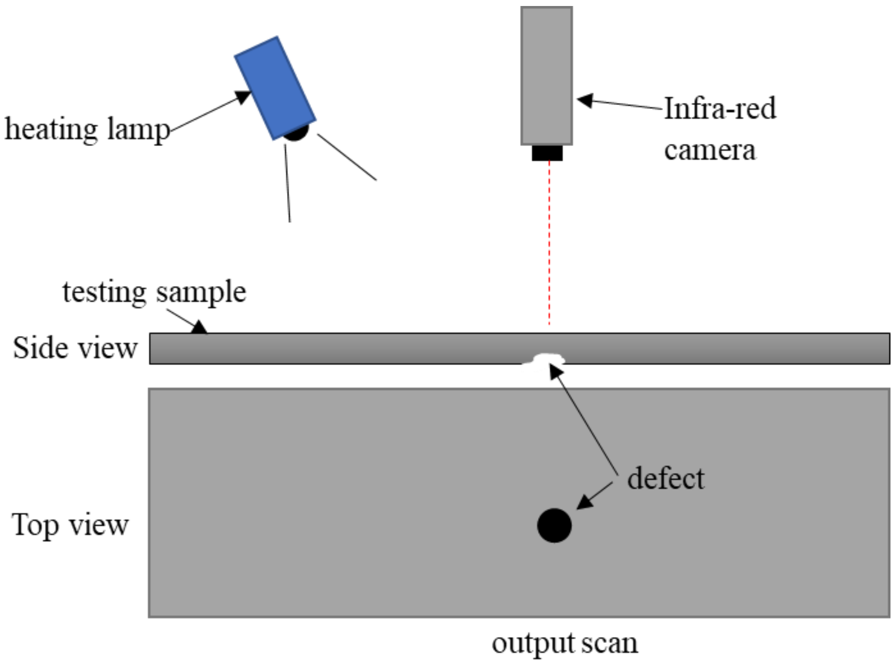

Figure 1.2. *Schematic diagram of a thermography experiment to detect a volumetric defect*

1.2.4. Electromagnetic methods

<u>Magnetic Flux Leakage</u>

Magnetic flux leakage (MFL) is a well-established technique, having been used by a wide range of industries since the 1960s [23], e.g. as an inspection technique for the oil and gas, transportation and energy industries [23, 24]. It can be used to detect corrosion in piping during manufacture and in-service [25]. Figure 1.3. is a schematic diagram showing a conventional magnetic flux leakage test. Within this configuration, a magnetic field is applied to the test part. The magnetic field can be generated using a Yoke magnetic field generator. As the inspected part is ferromagnetic, the magnetic lines are saturated and no leakage would occur in the case no defect is present. In the presence of a defects, the magnetic lines will be leaked and the magnetic flux density of the magnetic field intensity can be detected by placing a magnetic sensor such as a Hall effect sensor in proximity of the tested part.

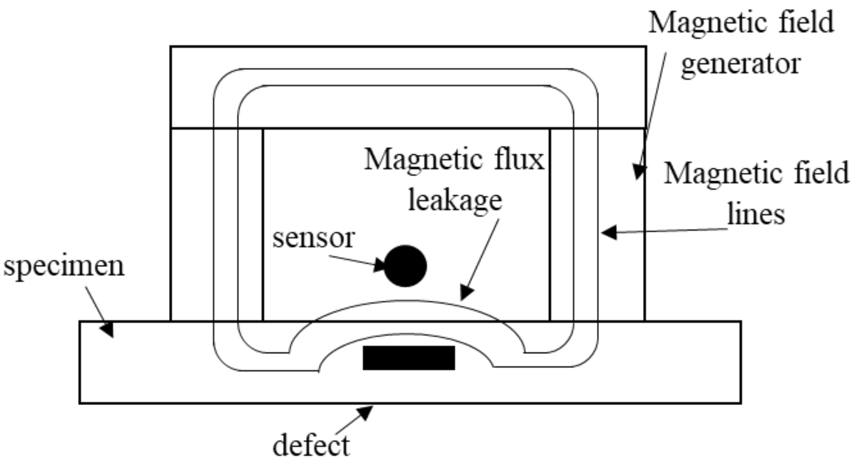

Figure 1.3. *Diagram showing the detection of a defect using the magnetic flux leakage method.*

The magnetic field lines would follow a closed path through the ferromagnetic steel if the specimen was defect free and the sample was not magnetically saturated. When a loss of material reduces sample thickness, this can cause magnetic saturation within the sample and will tend to expel more magnetic flux from the steel, which can be detected by a magnetic field sensor. Magnetic flux leakage will occur in the vicinity of the defect. The method does not require contact, but is only applicable to ferromagnetic and magnetically permeable materials. Another limitation is that this technique is well suited only for surface defects or near surface defects for thick structures. Nevertheless, this limitation is not considered in the case of thin structure or in the case of reaching the magnetic saturation for the defect free sample. Background noise is a problem and new studies are looking at better post-processing methods to deal with this [26,27].

Eddy current (EC) inspection

Eddy current (EC) inspection can be used for coating or sample thickness measurement and surface and sub-surface defect detection. Eddy currents are generated by placing an alternating current (AC) passing through a copper coil near the surface of the component, which generates an alternating magnetic field. An induced electrical current is then generated within the skin of depth of the tested sample [28]. The current induced will generate a magnetic field that is generally opposed to the one generated by the energised coil. Figure 1.4. represents a basic schematic diagram of EC testing, showing the dynamic field generated from the coil, the eddy current generated in the specimen and the opposing dynamic field generated from the induced currents. The new generated magnetic field will interfere with the coil's magnetic field which results in impedance reduction of the main coil or a secondary coil if a two-coil probe is used [29].

A diagram of the EC technique is illustrated in figure 1.4. If a flaw exists either at the surface or within the skin depth, the eddy current distribution will change, which results in disruption of the dynamic field generated from the induced current. This leads to changes in the amplitude and phase of the received signal [30]. By capturing the amplitude and the phase of the received signal, the defect can be located and sized.

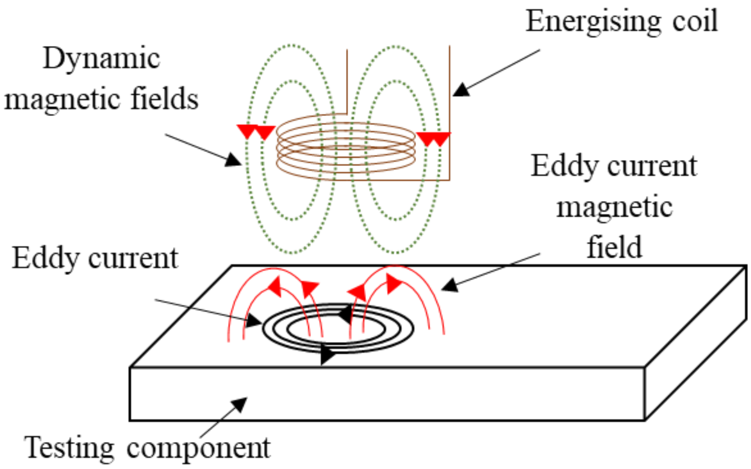

Figure 1.4. *The Eddy current method*

The EC technique can be applied in various ways, such as pulsed eddy current sensors [31-33], eddy current arrays [32] and numerous variations of coil types and arrangements for various applications. The pulsed eddy current can offer an alternative to the fixed frequency and skin depth issue [33]. The method uses a range of frequencies, which offers a scan for different depths, while keeping a good sensitivity for defects developed on the surface [34, 35]. The transient signal of the pulsed eddy current contains a vast amount of information that can size and analyse a given defect. However, the data processing is still challenging, generating very different responses depending on whether the component is conductive or ferromagnetic [36].

1.2.5. Ultrasonic testing

Ultrasound and ultrasonic waves describe the key elements used to perform ultrasonic inspection to reveal any potential defect in samples. The ultrasonic range is covering the frequency spectrum beyond the audible range. Usually, ultrasonic waves are generated with an excitation frequency exceeding 20 kHz and can reach higher frequency range exceeding 200 MHz. Ultrasound in general is used in multiple applications such as industrial inspection of in-service parts, defect detection during manufacturing, and medical applications (e.g. imaging) [37, 38]. In NDT, the ultrasonic waves have different modes that can be distinguished based on direction of motions of particles, particle velocities and the direction of propagation of the ultrasonic wave [39, 40].

In order to define the ultrasonic waves, an isotropic material with no boundary conditions is considered [40, 41]. As these waves are used in non-destructive applications, the generated waves amplitudes should remain as low as not to exceed the elastic range of the test sample. The waves can be also defined as stress and strain applied to particles within the structure. The relation between stress and strain can be given as:

$$\sigma_{ij} = C_{ijkl}\epsilon_{kl} \tag{1.1}$$

Where σ_{ij} describes the stress tensor and C_{ijkl} is the stiffness tensor.

As discussed earlier in this section, ultrasound waves, in the bulk of a material, can manifest as two distinct wave modes, either longitudinal waves or shear (transverse) waves. This statement was derived from the general wave mode given as:

$$\nabla\left(\frac{\partial^2\phi}{\partial t^2} - c_{11}\nabla^2\phi\right) + \nabla\times\left(\rho\frac{\partial^2\psi}{\partial t^2} - c_{44}\nabla^2\psi\right) = 0 \tag{1.2}$$

where ϕ and ψ are scalar potential and vector potential respectively. $c_{11}$and c_{44} are defined as follows:

$$c_{11} = \lambda + 2\mu \tag{1.3}$$

$$c_{44} = \mu$$

where λ and μ are Lamé constants.

The main ultrasonic waves modes are longitudinal waves and transverse waves in a bulk material. The equations describing longitudinal waves and shear waves are:

$$C_L = \sqrt{\frac{c_{11}}{\rho}} = \sqrt{\frac{\lambda + 2\mu}{\rho}} \tag{1.4}$$

$$C_T = \sqrt{\frac{c_{44}}{\rho}} = \sqrt{\frac{\mu}{\rho}} \tag{1.5}$$

where C_L is the wave longitudinal velocity while C_T is the shear velocity in a bulk material. The shear motion of the waves has two orthogonal polarization components forming the shear vertical and shear horizontal direction of particle motion. It is important to report the fact that longitudinal waves are parallel to the direction of the wave propagation while transverse motion is perpendicular to the wave propagation direction.

Ultrasonic testing (UT) using elastic waves within the ultrasound range is an established NDT method [42, 43]. In a typical test, the signal from an ultrasonic transducer is emitted into the sample, and the ultrasonic wave arrival is detected using the same device (i.e. it is used in the pulse-echo mode or a dual probe mode). This allows different parameters to be measured, such as material properties, sample thickness and the presence of a defect [44], as shown in figure 1.5. The most common ultrasonic mode used is the longitudinal wave. However, some inspections use shear waves, where the signal can be generated using different technologies. In fact, the signal can be generated using a compression wave that is passed through a polymer wedge [45] or cutting the quartz in a very specific direction leading to the generation of shear waves. The polymer wedge is very specific as it can result in the generation of surface waves rather than through thickness shear waves. Note that EMATs are also a good way of generating shear waves [46].

The ultrasonic method uses different geometries for different inspection scenarios. One example is time of flight diffraction (TOFD) [47], whereby the signal diffracted by the crack tip is detected as well as a back-wall echo, using a separate source and receiver. Another is the increasing use of ultrasonic phased arrays [48].

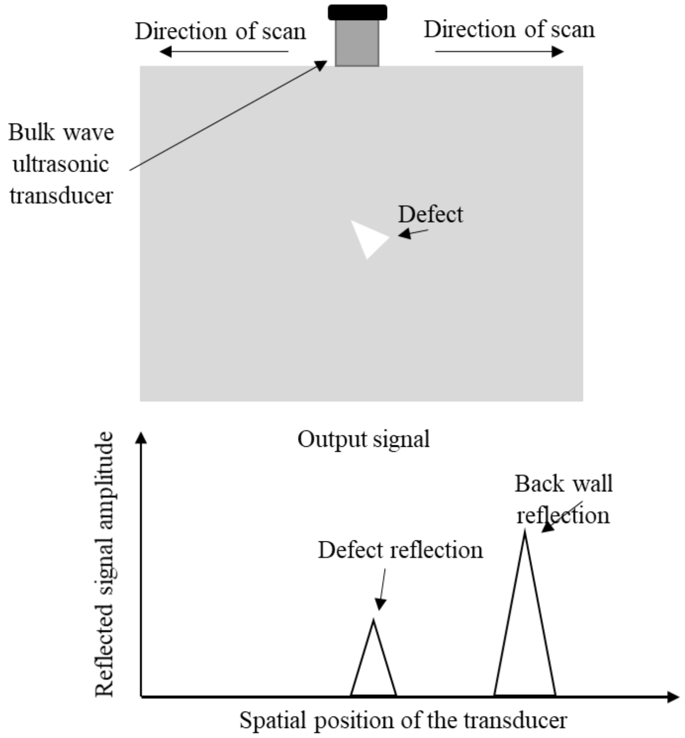

Figure 1.5. *Typical pulse-echo ultrasonic measurement, represented in this case via rectified signals.*

1.3. Ultrasonic guided waves

The ultrasonic testing described so far uses bulk wave modes i.e. longitudinal or shear waves. Guided waves exist in structures where the propagating waves interact with the boundaries of a material, e.g. in a plate or pipe [49, 50]. Amplitude and the phase are key parameters needed to identify different types of guided waves travelling through a material. In general, the guide-wave modes allowed for a particular parallel-sided plate can be considered within two main groups: Lamb Waves and Shear Horizontal (SH) waves [51, 52]. In the following sections, an overview will be given regarding the different guided waves modes, with a focus on Lamb waves and SH waves, and how they can be preferentially generated or detected. In addition, a brief discussion of velocity analysis, attenuation and dispersion curves will be given.

1.3.1. General overview of Lamb Waves:

Lamb waves are elastic waves travelling within a waveguide where the generated strain is interacting with both upper and lower boundaries of the plate. The in-plane and out-of-plane strain is used to differentiate two types of Lamb wave mode: symmetrical modes and antisymmetric modes. The antisymmetric mode has a flexural type of wave motion, whereas the symmetrical mode is symmetrical with regards to the mid-plane (see figure 1.6). Both have particle motion in both the direction of travel and perpendicular to the plate surface [43].

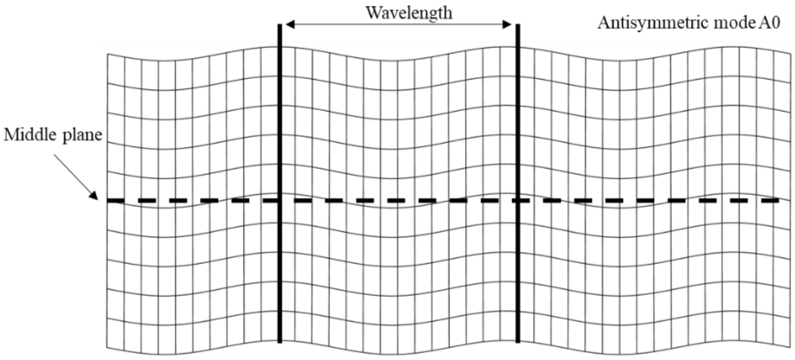

(a)

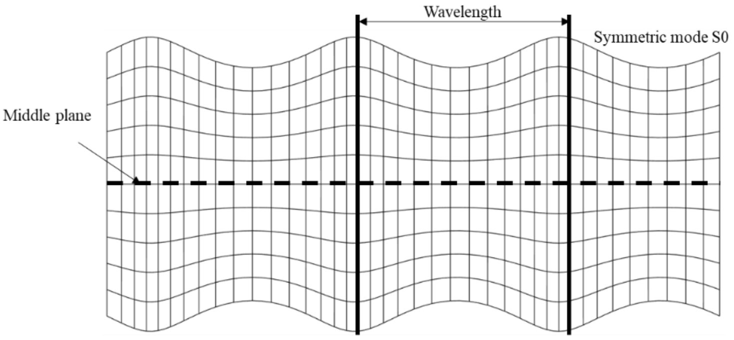

(b)

Figure 1.6. *Schematic diagram showing the particle motion for (a) the A0 mode and (b) the S0 mode in a plate for a given frequency*

Lamb waves are generally dispersive, meaning that the phase and group velocities are frequency-dependent. Understanding this dispersion is essential in any analysis of the received signal [51, 53]. Lamb waves can also exist at different modes such as the fundamental modes or higher order modes. Lamb waves can be identified through two distinct velocities: phase velocity and group velocity. The phase velocity is measured by determining the time of travel of a one chosen part of a signal, whereas group velocity measures the velocity of the whole wave packet [43] as can be seen in figure 1.7.

The expressions for phase and group velocity are derived from the equations of motion for guided waves. A common approach to solve the general equation of displacement and the free plate problem is through the method of potentials. The equations describing the displacement of Lamb waves are given through the Rayleigh-Lamb equations which are valid for isotropic materials:

$$\frac{\tan(qh)}{\tan(ph)} = -\frac{4k^2pq}{(q^2-k^2)^2} \qquad \text{For Lamb wave symmetric modes} \tag{1.6}$$

$$\frac{\tan(qh)}{\tan(ph)} = -\frac{(q^2-k^2)^2}{4k^2pq} \qquad \text{For Lamb waves antisymmetric modes} \tag{1.7}$$

where p and q are obtained through the equations:

$$p^2 = \frac{\omega^2}{C_L^2} - k^2 \tag{1.8}$$

$$q^2 = \frac{\omega^2}{C_T^2} - k^2 \tag{1.9}$$

Here, $C_L, C_T, \omega, h\ and\ k$ are the bulk longitudinal wave velocity, transverse or shear wave velocity, angular frequency, half of the thickness of the plate and wavenumber respectively. However, for shear horizontal guided waves, the equations describing the motion of a given particle must meet Navier’s criterion, and the equation of motion can be expressed as:

$$\mu\nabla^2 u(x,t) + (\lambda+\mu)\nabla\nabla\cdot \mathrm{u(x,t)} = \rho\frac{d^2u(x,t)}{dt^2} \tag{1.10}$$

where μ, λ are Lamé parameters and ρ is the material density.

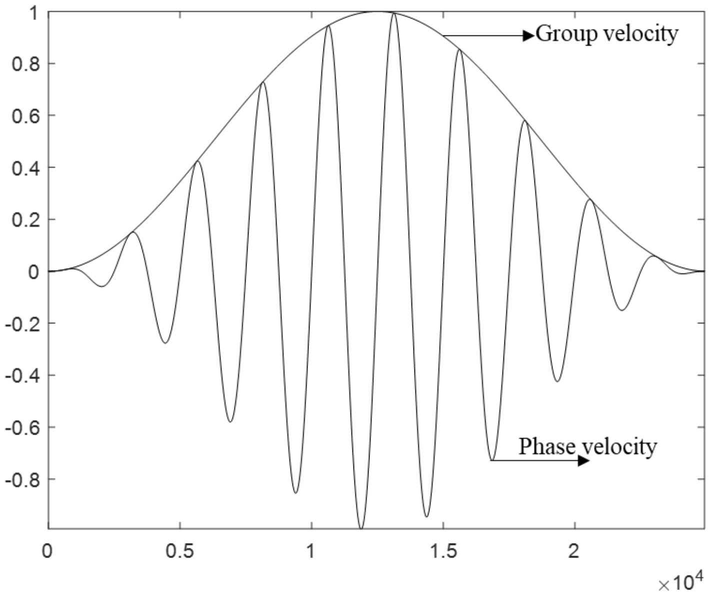

Figure 1.7. *Illustration of group velocity and phase velocity for windowed signal*

Lamb waves are dispersive and hence dispersion curves are needed to determine their properties for practical use. Examples for Lamb waves dispersion curves are shown in figure 1.8 for phase and group velocities in a 1 mm thick aluminium plate, over a frequency of 20 kHz - 3.5 MHz. Figures 1.8 shows the predictions of phase and group velocities for Lamb and SH guided waves. It is noticeable that for low frequencies, the phase velocity of the fundamental symmetric mode S0 is almost non-dispersive. The cut-off frequency for the A1 mode is also indicated by the vertical dashed line. At frequencies below this, only the A0 and S0 modes will propagate.

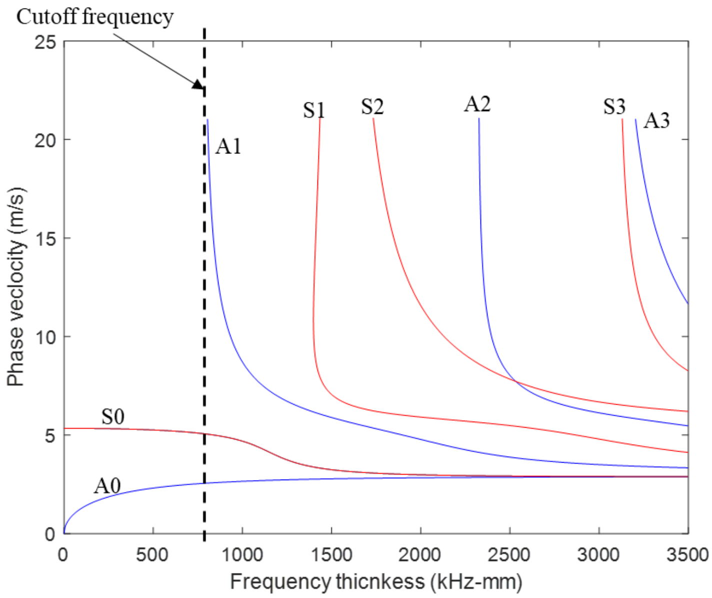

(a)

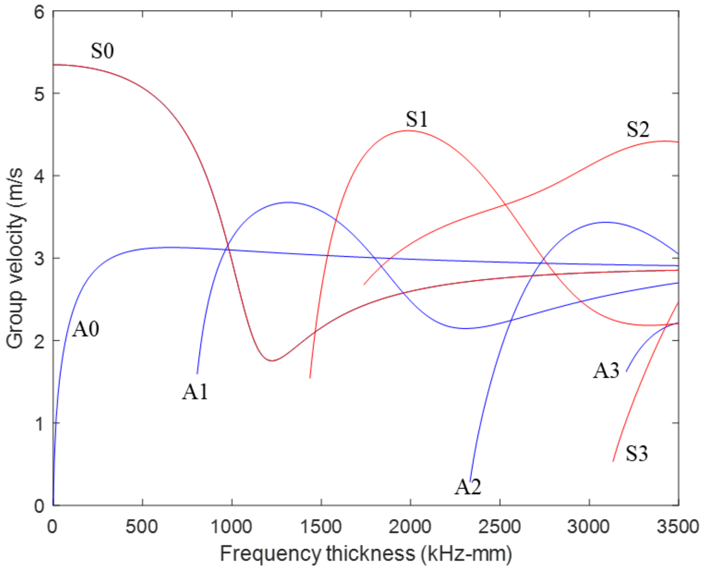

(b)

Figure 1.8. *Lamb waves calculated velocities for an aluminium plate, 1mm thickness, showing higher modes for both symmetrical mode and antisymmetric mode for both (a) phase velocity and (b) group velocity*

1.3.2. General overview of Shear horizontal waves:

Similar to Lamb waves, the Shear horizontal (SH) waves are used to detect defect and anomalies within structures. They are fundamentally different from Lamb waves as to how the wave is generated and propagating. They have a particle motion parallel to the boundaries of the plate. The motion is occurring in the perpendicular direction to the direction of the generated wave propagation. Conversely to Lamb waves, the SH0 mode is non-dispersive in flat parallel sides plates, but higher order modes (SH1, SH2 etc) are dispersive [43].

Although the Lamb wave equations of motion must be solved analytically, the shear horizontal waves displacement equations can be obtained through equations (1.11) and (1.12)

$$\sin(qh) = 0 \qquad \text{For shear horizontal symmetric modes} \tag{1.11}$$

$$\cos\,(qh) = 0 \qquad \text{For shear horizontal antisymmetric modes} \tag{1.12}$$

where

$$q = \sqrt{\frac{\omega^2}{C_T^2} - k^2} \tag{1.13}$$

As can be seen, the equations of displacement describing the shear horizontal waves are straight forward, and the group velocity (C_g) and phase velocity (C_p) can be expressed explicitly in function of the frequency and the plate-thickness product. The shear horizontal wave velocities are given in equations (1.14) and (1.15):

$$C_p(fd) = \pm 2C_T \left\{ \frac{fd}{\sqrt{4(fd)^2 - n^2 C_T^2}} \right\} \qquad \text{Phase velocity for shear horizontal waves} \tag{1.14}$$

$$C_g(fd) = C_T \sqrt{1 - \frac{(\frac{n}{2})^2}{(\frac{fd}{C_T})^2}} \qquad \text{Group velocity for shear horizontal waves} \tag{1.15}$$

where $C_T, n, f\ and\ d$ are the transverse or shear wave velocity, mode number, frequency and plate thickness respectively. An interesting feature is that when $n = 0$,

$C_p(fd) = C_T$. This demonstrates that the SH0 mode is non-dispersive and travels at the shear wave velocity. All the higher order modes (SH1, SH2 etc) are dispersive, and have a cut-off frequency below which they cannot propagate [43].

Figures 1.9 shows the predictions of phase and group velocities for SH guided waves in a 1-mm aluminium plate. As it can be seen, in the case of SH0, the phase and group velocity are equal for the fundamental mode SH0.

Higher order modes have a cut-off frequency which can be calculated for shear horizontal waves explicitly using the equation (1.16) [43]

$$(fd)_n = \frac{nC_T}{2} \tag{1.16}$$

In practice, a frequency is selected and the displacement at the surface is analysed and then the dispersion curve is checked in order to define the velocities of interest that will be used to post-process the received data while the displacement is analysed to understand the favourable forces required to be applied in order to enhance defect detection. The selection of the frequency is crucial, as it might engender generating higher modes based on the need and the experiment conducted. In fact, if the frequency is higher than the cut-off frequency, then higher order modes are generated within the waveguide which can make the inspection slightly more complicated as different modes can co-exist within the same inspection operation for defect detections based on pulse-echo configuration where a reflected signal is detected. Higher modes can be useful for other applications such as thickness gauging using a cut-off frequency. Thus, prior knowledge of the testing to be done, the environmental parameters such as material and excitation frequency are critical to perform a successful NDT inspection.

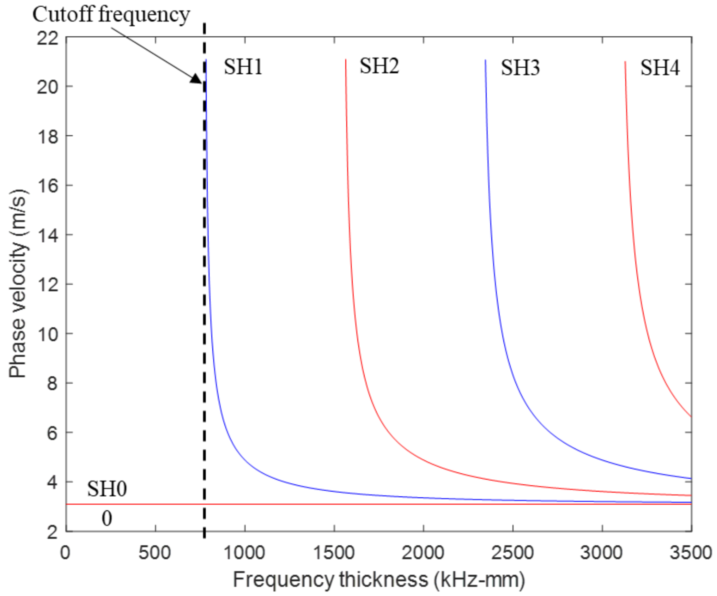

(a)

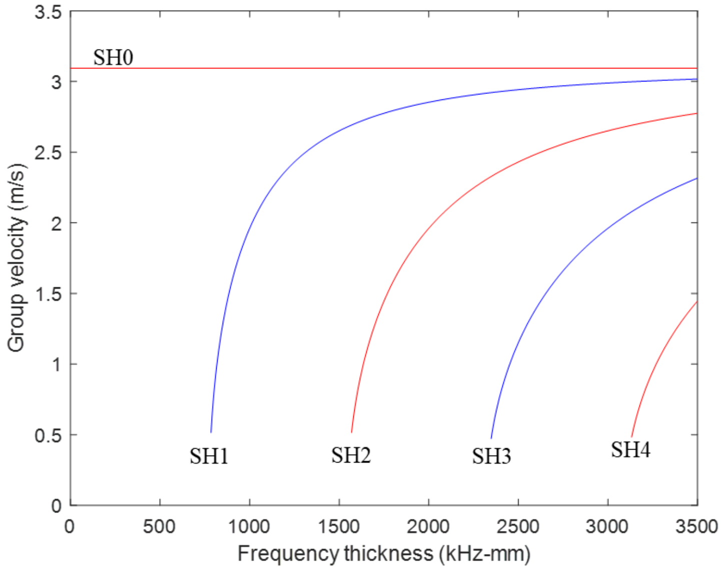

(b)

Figure 1.9. *Shear horizontal waves velocities for an aluminium plate, 1mm thickness, showing higher modes for both symmetrical mode and antisymmetric mode for both phase velocity (a) and group velocity (b)*

1.3.3. Practical considerations for guided waves modes selection:

With respect to NDT, it is conventional to operate below the cut-off frequency for either cases when Lamb waves are used or shear horizontal waves are used so to ensure that a minimum number of modes is induced in the material and most industries are referring to the use of the SH0 mode as it is non-dispersive and induces one mode only

[54]. Higher modes are used in other applications such as thickness analysis and prediction but it is highly depending on what is being achieved by the inspection operation. This was illustrated in figure 1.9 for both phase and group velocity.

1.3.4. Guided wave mode selection

Guided waves ultrasonic NDT is used in inspection of large areas due to their ability to travel following a waveguide. As mentioned before, guided waves can manifest in different shapes in terms of particle displacement and velocity engendering two main groups of guided waves: Lamb waves and shear horizontal waves. As there are multiple guided waves forms and modes, the evaluation of the suitability of one mode rather than another is vital for a correct inspection and trustworthy result. In addition, within the same mode, the analysis of the surface displacement is critical to enhance inspection results. In fact, a favourable surface displacement is selected initially and then a frequency range within the non-dispersive region is used as excitation frequency to generate the elastic waves used for inspection to make the inspection operation and the data collection and analysis easier to interpret. The use of this technique would limit the number of wave modes co-exiting in the structure and also would enhance the signal reflected from defects.

As a practical rule, guided waves should have good sensitivity to defects. So no small size defect are missed, the wave should have enough energy so to overcome the attenuation problems and in a typical inspection environment simple excitation and frequency selection for the induced wave is desired.

Depending on the phase velocity the selection of a high frequency may decrease the wavelength which allows the detection of small defects but as seen before, with high frequencies, higher modes are generated which makes the inspection more complex and decreases the induced wave energy [54].

In the case when the fundamental shear horizontal mode SH0 is chosen, the operation of parts inspection would be more straightforward for interpretation and analysis as the mode is non-dispersive. However, if either the A0 or S0 mode is selected, the level of dispersion must be taken into consideration. The S0 mode is relatively less dispersive for low frequencies while the A0 mode is massively dispersive for the same frequency range. The A0 mode is slower than the S0 mode, and thus the received waveform of the A0 can often be distinguished in the time domain, depending on the type of excitation used. Furthermore, the A0 wavelength is smaller than the S0 wavelength at the same frequency, which may make the A0 mode suitable for detecting smaller size defects in some cases. Longer wavelengths can be adopted to minimise the attenuation of the waves when travelling through the structures but the detection resolution can be altered. In the case of multiple defects, the wavelength should be smaller than the distance separating the detects of interest to be properly detected [55].

Figures 1.10, 1.11 and 1.12 provide schematic diagrams of the through thickness relative displacement profiles of Lamb waves and shear horizontal waves in a 2-mm thickness aluminium plate at 200 kHz frequency. The figures were obtained through an open-source MATLAB code where the thickness of the sample and the mechanical properties of the sample were introduced as input parameters. The frequency range and the displacement profiles were selected as output to be plotted as shown in the figures below:

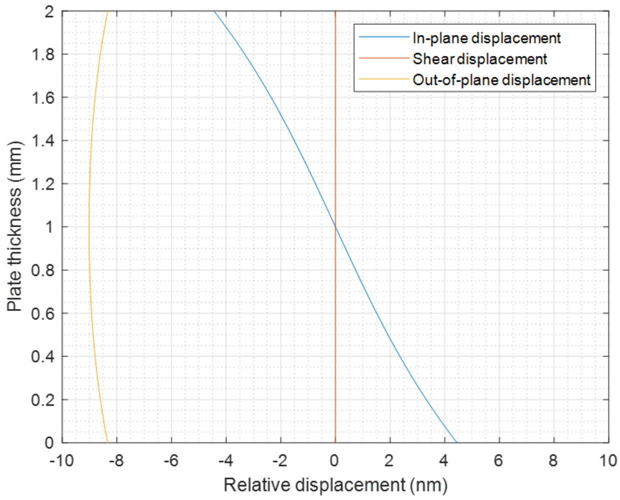

Figure 1.10. *Lamb wave fundamental antisymmetric mode A0 showing out-of-plane relative displacement, in-plane displacement and shear horizontal relative displacement*

The relative displacement profiles for different guided waves show that the elastic motion extends through the full thickness for an isotropic material. In the case of a composite plate, the detectability and reflection of the S0 mode is dependent mainly on the position of the defect in the composite plate. In fact, due to the reflection and attenuation levels, S0 mode is less favourable for the detection of delamination in composite materials [56].

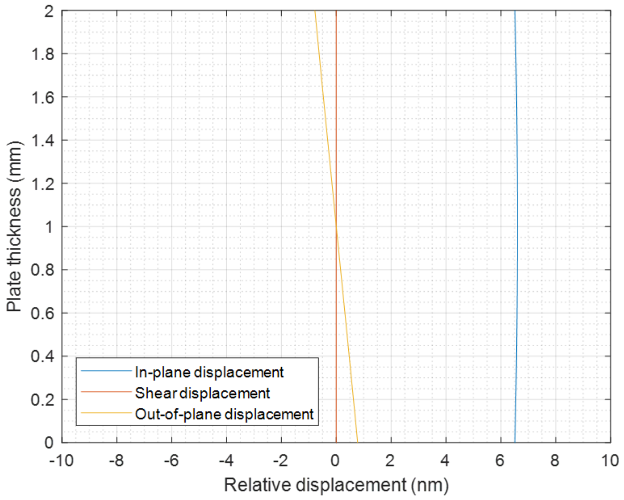

Figure 1.11. *Lamb wave fundamental symmetrical mode S0 showing out-of-plane relative displacement, in-pane relative displacement and shear horizontal relative displacement*

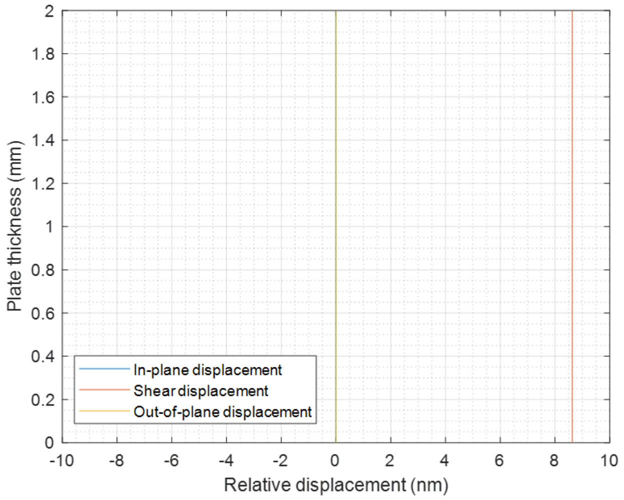

Figure 1.12. *Shear horizontal fundamental mode SH0 showing out-of-plane relative displacement, in-pane relative displacement and shear horizontal relative displacement (all displacement lines are overlapping)*

1.3.5. Generation of guided waves

Guided waves are widely used for inspection and can be generated using piezoelectric transducers [57], contactless methods such as air-couple sensors [58], laser-based techniques [59] and EMATs [60]. Each of these has its own advantages, weaknesses and area of applications. The most widely-used sensors are piezoelectric transducers due to their high signal to noise ratio, market availability and simple operation. However, this type of sensors requires contact to the testing surface and the application of couplant, which limits its field of applications. Laser-based sensors can be used to generate guided waves in a lab environment because of health and safety issues, as they tend to use high power, class IV laser beams, and sample surface preparation is often needed for the detection of the waves while for generation, the surface preparation is not required. The laser systems used to generate guided waves in an industrial environment require further shielding for health and safety purposes. Lasers interferometers or beam deflectors systems can also be used to detect guided waves propagation at a surface [61, 62] providing a non-contact technique. These technologies are capable of generating both Lamb waves and shear horizontal waves. A common practice for the pitch-catch technique is to generate guided waves using one of the above methods while detecting the reflections using a laser-based system [63]. Such a technique is described later in this thesis. EMATs can also be used to generate a wide range of Lamb waves and SH waves by careful selection of coil and static magnetic field characteristics [64, 65], but they are limited in that they are only suitable for conductive plates [66]. To overcome such an issue, conducting patches can be applied to the surface [67].

1.3.6. Guided waves in composites

General overview of composite materials:

Composite material is a general term used to describe the combination of 2 or more different materials to construct an integral structure. The materials are required to be chemically different [68]. Generally, composite materials can be found in different forms. In fact, they can be manufactured as a solid laminate either in carbon or glass or bonded structures such panels using honeycomb design or a sandwich structure using ceramic matrix and foam [69].

With the current progress in material science, composite materials are attracting more interest due to their numerous advantages. They are used in numerous applications mainly in aerospace structures, new generation of automotive structures and in renewable energy sector. It is important to note that most of the main body for newer aircraft is mad of composite material such as the A350 or the Boeing 787 [70]. The main two families for composite material used in industry are distinguishable by the type of fibres used thus composite materials can be carbon fibre reinforced polymers CFRP or glass fibres reinforced polymers GFRP. For the wider application, composite materials are a reference to fibre reinforced polymers as they may contain different types of fibres (Aramid, Kevlar or graphite) based on the design and the application [68]. On the other hand, the resin system used as the matrix to hold the distributed fibres can be obtained from different materials such as polyamide, phenolic and epoxy [71]

Based on the design, composite materials can be manufactured using multiple processes but a global process consists of placing multiple lay-ups and then apply a resin system to build the final product. Such a design provides multiple advantages such as design flexibility and higher strength. However, in some instances like in the case of unidirectional composites, where the fibres are along one specific direction, the structure have extremely low tensile strength in the direction perpendicular to the fibre’s direction. In order to overcome such a limitation, as the material design is flexible, different layers of composite can be applied in different configurations such as 0^{o},90^{o} or $+45^{o}$, -45^{o} to increase the tensile strength in different orientations [66, 72].

While in service, different defects can be developed. These defects can be located either on the surface or within the thickness of the structure. Defects can be delaminations resulting from matrix cracking, fibre fracture or impact damage. In addition to that, defects related to the manufacturing can be developed such as fibre misalignment, voids or porosities. In order to detect these defects and maintain the integrity of the structure, NDT methods are used to inspect composite materials similar to conventional metallic structures [73].

In practice, although NDT methods are being used to inspect composite structures, they are still considered challenging materials for NDT applications. Most of the conventional NDT methods can be applicable to inspect composite material apart from magnetic flux leakage as composites are not ferromagnetic materials. In fact, the use of UT inspection can be difficult due to large acoustic impedance difference in honeycomb structures for example [74]. Also, UT inspection is considered a lengthy process in terms of time and resources which limits its application to inspect large parts. Another limitation linked to the use of UT inspection methods for composite material is called the shadow effect. In fact, large delaminations located near the surface of the structure would lead to the reflection of the almost the entire acoustic energy which reduces the detection capabilities of the method [75].

Eddy currents can also be used to inspect composite materials but their performance is reduced significantly. In fact, eddy current methods are only used when the fibre of the structure is conductive (CFRP) but their conductivity is very low which limits the detection capability of eddy current in a way that distinguishing interlaminar cracks to delaminations can be challenging [73].

Another method which is thermography can be used to inspect composite materials both in passive configuration or active configuration. However, the use of the method is only limited to near surface defect detection [76]. In addition to that, due to irregularities within the material that can form during manufacturing, a similar thermal response can be obtained for delaminations and healthy structures [77] which significantly reduces the accuracy of detection of thermography.

Guided waves generation in composite materials:

Guided waves are used extensively for the inspection of composite structures. Prior knowledge of the material parameters and how guided waves are travelling in a specific manner within composite plate is essential to implement an NDE inspection [78]. Anisotropy within these materials can introduce complications, such as direction-dependent velocity, beam steering and attenuation [79]. Aspects such as the lay-up configuration, the plate geometry and the properties of the material must be known to perform a successful guided waves inspection [80]. The velocity changes for different directions and knowledge of the group velocity is essential to calculate time of flight (TOF) when analysing defect location.

The second feature of interest is beam steering, where the wave energy can be concentrated in some preferred direction. [81, 82]. Different guided wave modes will be affected by the composite lay-up sequence, tending to travel along the fibre direction. This must be taken into consideration while designing guided waves experiments [83, 84].

1.3.7. Interaction of guided waves with defects

When a delamination occurs, it can be detected using guided waves by recording the reflected wave and calculating the velocity and time of arrival [85]. Additionally, parameters of the delaminations such as size can also be measured. When the elastic guided waves interact with a delamination, mode conversion may occur and by measuring the characteristics of the mode-converted waves, the size and location of a delamination can be estimated [86]. Researchers have shown that the A0 and the S0 modes can be used to detect a delamination using a transformation of the wavelet of the received signal and multiple signal processing techniques [87, 88]. In the case where the composite has a cross-ply lay-up, the delamination was successfully detected using B-scan imaging of the detected Lamb wave A0 mode [89].

Impact damage is considered a more complex problem for guided wave inspection [90, 91]. Impact damage occurs when an object hits the composite plate causing plastic deformation. The deformation profile varies with different impact energies, and damage within a unidirectional plate will be significantly different to that for a quasi-isotropic sample [92]. Impact damage is a simple event leading to complex results and plate behaviour for composite materials.

Impact damage in cross-ply plates has been studied using the A0 mode excited at 20 kHz, although noise levels were high [93]. It was reported in the literature that the amplitude of the A0 mode can decrease significantly near the impacted area due to attenuation [94], although the spatial pattern of attenuation was complex [95, 96]. The impact damage location can be predicted if the travelling wave velocity is known [97].

1.4. Thesis Outline

A new approach for generating and detecting guided waves in composites would be a welcome addition, especially if control over the wave mode was available. This thesis describes one approach using removable magnetostrictive patches which are attached to the surface of the sample.

The use of magnetostriction in NDT applications is established, but a greater knowledge of how the different parameters variation can affect magnetostriction is lacking. In fact, knowledge about how the input parameters such as the excitation frequency or the direction of the applied magnetic fields enhance the performance of the magnetic patch is limited. In addition, the use of magnetostrictive patches provide greater advantages compared to piezoelectric transducers in terms of design flexibility and their ability to generate multiple modes across a wide range of frequencies using the same patch, while modifying the combination of the applied magnetic fields without the need to redesign the system as with PZTs.

Chapter 2 gives a summary of the different ultrasonic transduction methods. It outlines the basics of EMAT operation by briefly explaining their history and development, followed by the principle of operation presentation detailing how EMATs work in terms of excitation and detection of different ultrasonic waves. Finally, a detailed description of the Lorentz force, magnetization and magnetostriction generation mechanism are included in the thesis. A discussion of EMATs is relevant, as similar AC coil and static magnetic field geometries are used for interacting with the magnetostrictive patch.

In Chapter 3, the theory of magnetostriction is outlined and the equations governing magnetostriction are presented. A special focus is given to the transfer equation linking strain generation to the presence of a magnetic field, and the different factors affecting magnetostriction are described. Finally, different materials that could be of use in the present experiments are discussed.

The subject of Chapter 4 is study of the effect of magnetic field direction on the generation of S0, A0 and SH0 guided waves modes by a magnetostrictive patch. Different magnetic field configurations and directions were examined experimentally so as to understand the effect of different combination of the generation mechanisms within a magnetostrictive patch.

In Chapter 5, the numerical modelling (supporting the experimental work reported in chapters 4, 6 and 7) of the different parameters affecting the transduction mechanism is presented. The governing equations and the steps used in modelling the dynamic magnetic field and the static magnetic field are presented. As the process includes different physics and commercial software, the workflow of integrating different aspects of the model is summarized. Finally, the interaction of the different magnetic fields and the magnetostrictive curve for the ferromagnetic material used within the patch are presented.

Chapter 6 presents a study of the effect of different parameters on magnetostriction induced ultrasonic generation. These included excitation frequency, static magnetic field and dynamic magnetic field magnitude and direction. Chapter 6 also includes an observation of magnetostriction at low static magnetic fields levels leading to interesting behaviour at different magnetic fields combinations.

Chapter 7 examines the potential of the magnetostrictive patches for the detection of defects in composite plates using guided waves in pulse-echo configuration. A lab-induced defect and then a delamination are investigated and the defect images were reconstructed using the Synthetic Aperture Focusing Technique (SAFT).

Finally, Chapter 8 highlights the main achievements of the work, and the ways in which the research can be taken forward as Future Work.

References for Chapter 1

[1] Cawley, P., 2001. Non-destructive testing—current capabilities and future directions. Proceedings of the I MECH E Part L Journal of Materials:Design and Applications, 215(4), pp.213-223.
[2] L. W. Schmerr. Fundamentals of Ultrasonic Non-destructive Evaluation: A Modeling Approach. Plenum Press, Norwell, 1998.
[3] B. W. Maxfield and C. M. Fortunko. The design and use of electromagnetic acoustic wave transducers (EMATs). Materials Evaluation, 41:1399–1408, 1983.
[4] Hernandez-Valle, F. and Dixon, S., 2011. Pulsed electromagnet EMAT for ultrasonic measurements at elevated temperatures. Insight - Non-Destructive Testing and Condition Monitoring, 53(2), pp.96-99.
[5] G. Brekow. Non-destructive testing. Radiography, ultrasonics, liquid penetrant, magnetic particle, eddy current. Materials and Corrosion/Werkstoffe und Korrosion, 47(10):579–579, October 1996
[6] P. E. Mix. Introduction to Nondestructive Testing: A Training Guide. Wiley, 2005.

[7] Almond, D.P. and Pickering, S.G., 2012. An analytical study of the pulsed thermography defect detection limit. Journal of applied physics, 111(9), p.093510.

[8] A. Demma, P. Cawley, M. Lowe, A.G. Roosenbrand, and B. Pavlakovic. The reflection of guided waves from notches in pipes: a guide for interpreting corrosion measurements. NDT & E International, 37(3):167–180, 2004.

[9] S. Dixon, C. Edwards, and S. B. Palmer. High accuracy non-contact ultrasonic thickness gauging of aluminium sheet using electromagnetic acoustic transducers. Ultrasonics, 39(6):445–453, 2001.

[10] S. Dixon, P. A. Petcher, Y. Fan, D. Maisey, and P. Nickolds. Ultrasonic metal sheet thickness measurement without prior wave speed calibration. Journal of Physics D: Applied Physics, 46(44):445502, 2013.

[11] D.E. Bray and D. McBride. Nondestructive testing techniques. New dimensions in engineering. John Wiley & Sons, Inc., 1992

[12] P. E. Mix. Introduction to Nondestructive Testing: A Training Guide. Wiley, 2005.

[13] D.E. Bray and D. McBride. Nondestructive testing techniques. New dimensions in engineering. John Wiley & Sons, Inc., 1992

[13] M. J. Lovejoy. Penetrant Testing: A practical guide. Springer Netherlands, 1991.

[14] Idris, A., 1995. Non-contact ultrasonic study on thixotropic alloys (Doctoral dissertation, University of Warwick).

[15] Dhakal, H.N. and Ismail, S.O., 2020. Sustainable composites for lightweight applications.

[16] R. Halmshaw. Industrial Radiology: Theory and practice. Non-Destructive Evaluation Series. Springer Netherlands, 2012.

[17] D. E. Bray and D. McBride. Nondestructive Testing Techniques. New Dimensions In Engineering Series. Wiley, 1992.

[18] T. Matsumoto and H. Mimura. Point x-ray source using graphite nanofibers and its application to x-ray radiography. Applied Physics Letters, 82(10):1637– 1639, 2003.

[19] Shull, P.J., 2002. Nondestructive evaluation: theory, techniques, and applications. CRC press.

[20] Regulations, Ionising Radiations., 1999. Statutory instrument 1999 no. 3232. London: Her Majesty's Stationary Office.

[22] T. Matsumoto and H. Mimura. Point x-ray source using graphite nanofibers and its application to x-ray radiography. Applied Physics Letters, 82(10):1637– 1639, 2003 .

[23] Almond, D.P. and Pickerin g, S.G., 2012. An analytical study of the pulsed thermography defect detection limit. Journal of applied physics, 111(9), p.093510.

[21] D. P. Almond and S. G. Pickering. Analysis of the defect detection capabilities of pulse stimulated thermographic NDE techniques. AIP Conference Proceedings, 1581(33):1617–1623, 2014.

[22] S.R. Baughman. Application for thermal NDT on advanced composites in aerospace structures. Proc. SPIE 3361, Thermosense XX, 3361:311–319, 1998.

[23] Wang, Z., Gu, Y. and Wang, Y., 2012. A review of three magnetic NDT technologies. Journal of Magnetism and Magnetic Materials, 324(4), pp.382-388.

[24] Pandey, M., 1998. Probabilistic models for condition assessment of oil and gas pipelines. NDT & E International, 31(5), pp.349-358.

[25] Babbar, V. and Clapham, L., 2006. Modeling the Effects of Pit Corner Geometry on Magnetic Flux Leakage Signals. Research in Nondestructive Evaluation, 17(3), pp.161-175.

[26] F. F¨orster. On the way from the know-how to know-why in the magnetic flux leakage field method of nondestructive testing. Materials Evaluation, 43:1154–1162; 1398–1404, 1985.

[27] Mandache, C. and Clapham, L., 2003. A model for magnetic flux leakage signal predictions. Journal of Physics D: Applied Physics, 36(20), pp.2427-2431.

[28] D. E. Bray and R. K. Stanley. Non-destructive Evaluation: A Tool in Design, Manufacturing and Service. Taylor & Francis, 1996

[29] Sophian, A., Tian, G. and Fan, M., 2017. Pulsed Eddy Current Non-destructive Testing and Evaluation: A Review. Chinese Journal of Mechanical Engineering, 30(3), pp.500-514.

[30] R. Halmshaw. Non-destructive Testing. Metallurgy and materials science. Edward Arnold, 1991.

[31] B. Lebrun, Y. Jayet, and J.-C. Baboux. Pulsed eddy current signal analysis: application to the experimental detection and characterization of deep flaws in highly conductive materials. NDT & E International, 30:163–170, 1997.

[32] A. McNab and J. Thomson. An eddy current array instrument for application on ferritic welds. NDT & E International, 28(2):103–112, 1995

[33] H.A. Wheeler. Formulas for the Skin Effect. Proceedings of the IRE, 30(9):412–424, 1942.

[34] B. Lebrun, Y. Jayet, and J.-C. Baboux. Pulsed eddy current signal analysis: application to the experimental detection and characterization of deep flaws in highly conductive materials. NDT & E International, 30:163–170, 1997.

[35] D. G. Park, C. S. Angani, and Y. M. Cheong. Differential Pulsed eddy current probe to detect the sub surface Cracks in a Stainless Steel Pipe. In 18th World Conference on Nondestructive Testing, Durban, 2012.

[36] T. Chen, G.Y. Tian, A. Sophian, and P.W Que. Feature extraction and selection for defect classification of pulsed eddy current NDT. NDT&E International, 41 (6):467–476, 2008.

[37] Wells, P.N.T., 1970. The medical applications of ultrasonics. Reports on Progress in Physics, 33(1), p.45.

[38] Saitoh, S., Izumi, M. and Mine, Y., 1995. A dual frequency ultrasonic probe for medical applications. IEEE transactions on ultrasonics, ferroelectrics, and frequency control, 42(2), pp.294-300.

[39] Blitz, J. and Simpson, G., 1996. Ultrasonic methods of non-destructive testing. London: Chapman & Hall.

[40] Clough, M.A., 2016. Defect screening of pipelines using circumferential guided waves (Doctoral dissertation, University of Warwick).

[41] Slaughter, W.S., 2012. The linearized theory of elasticity. Springer Science & Business Media.

[42] J. Blitz and G. Simpson. Ultrasonic Methods of Non-destructive Testing. NonDestructive Evaluation Series. Springer Netherlands, 1995.

[43] Rose, J., 2014. Ultrasonic waves in solid media. Cambridge: Cambridge University Press.

[44] F. Benmeddour, S. Grondel, J. Assaad, and E. Moulin. Experimental study of the A0 and S0 Lamb waves interaction with symmetrical notches. Ultrasonics, 49(2):202–5, 2009.

[45] Farhat, H., 2021. NDT processes: Applications and limitations. Operation, Maintenance, and Repair of Land-Based Gas Turbines, pp.159-174.

[46] Parra-Raad, J., Khalili, P. and Cegla, F., 2020. Shear waves with orthogonal polarisations for thickness measurement and crack detection using EMATs. NDT & E International, 111, p.102212.

[47] M. G. Silk and B. H. Lidington. The potential of scattered or diffracted ultrasound in the determination of crack depth. Non-Destructive Testing, 8(June):146–151, 1975.

[48] L. W. Schmerr. Fundamentals of Ultrasonic Phased Arrays. Solid Mechanics and Its Applications. Springer International Publishing, 2014.

[49] G. R. Liu and Z. C. Xi, Elastic Waves in Anisotropic Laminates. Boca Raton: CRC Press LLC, 2000.

[50] J. D. Achenbach, Wave propagation in elastic solids. Amsterdam and New York: North-Holland Pub. Co., 1973.

[51] P. Wilcox, M. Lowe, and P. Cawley, “The effect of dispersion on long-range inspection using ultrasonic guided waves,” NDT E Int., vol. 34, no. 1, pp. 1–9, Jan. 2001.

[52] J. L. Rose, “Ultrasonic guided waves in structural health monitoring,” Key Eng. Mater., vol. 270–273, pp. 14–21, 2004.

[53] W. H. Prosser, M. D. Seale, and B. T. Smith, “Time-frequency analysis of the dispersion of Lamb modes.,” J. Acoust. Soc. Am., vol. 105, no. 5, pp. 2669–76, May 1999.

[54] D. N. Alleyne and P. Cawley, “Optimization of Lamb wave inspection techniques,” NDT E Int., vol. 25, no. 1, pp. 11–22, Jan. 1992.

[55] R. A. Kline, Nondestructive characterization of composite media. Pennsylvania: Technomic Publishing Company, 1992

[56] N. Guo and P. Cawley, “The interaction of Lamb waves with delaminations in composite laminates,” J. Acoust. Soc. Am., vol. 94, no. 4, p. 2240, Oct. 1993.

[57] H. Duflo, B. Morvan, and J. L. Izbicki, “Interaction of Lamb waves on bonded composite plates with defects,” Compos. Struct., vol. 79, no. 2, pp. 229–233, Jul. 2007.

[58] Nsengiyumva, W., Zhong, S., Lin, J., Zhang, Q., Zhong, J. and Huang, Y., 2021. Advances, limitations and prospects of nondestructive testing and evaluation of thick composites and sandwich structures: A state-of-the-art review. Composite Structures, 256, p.112951.

[59] S. E. Burrows, B. Dutton, and S. Dixon. Laser generation of Lamb waves for defect detection: experimental methods and finite element modeling. IEEE transactions on ultrasonics, ferroelectrics, and frequency control, 59(1):82–9, 2012.

[60] M. Hirao and H. Ogi. EMATs for science and industry: noncontacting ultrasonic measurements. Kluwer Academic Publishers, London, 2003.

[61] W. Gao, C. Glorieux, and J. Thoen, “Laser ultrasonic study of Lamb waves: determination of the thickness and velocities of a thin plate,” Int. J. Eng. Sci., vol. 41, no. 2, pp. 219–228, Jan. 2003.

[62] J. Pohl and G. Mook, “Laser-vibrometric analysis of propagation and interaction of Lamb waves in CFRP-plates,” CEAS Aeronaut. J., vol. 4, no. 1, pp. 77–85, Jan. 2013.

[63] Zhang, K. and Zhou, Z., 2018. Quantitative characterization of disbonds in multilayered bonded composites using laser ultrasonic guided waves. NDT & E International, 97, pp.42-50.

[64] Xie, C., Liu, T., Pei, C., Jin, Y. and Chen, Z., 2021. A new longitudinal mode guided-wave EMAT with periodic pulsed electromagnets for non-ferromagnetic pipe. Sensors and Actuators A: Physical, 331, p.112991.

[65] Zhang, Y., Liu, W., Li, N., Qian, Z., Wang, B., Liu, D. and Li, X., 2021. Design of a new type of omnidirectional shear-horizontal EMAT by the use of half-ring magnets and PCB technology. Ultrasonics, 115, p.106465.

[66] O. Putkis, R. P. Dalton, and A. J. Croxford, “The anisotropic propagation of ultrasonic guided waves in composite materials and implications for practical applications.,” in press, corrected proof, doi:10.1016/j.ultras.2014.11.013

[67] Amato, S., 2021. Inspection of composite aerospace structures using capacitive imaging and guided waves. PhD. University of Warwick.

[68] Hull, D. and Clyne, T., 2003. An introduction to composite materials. Cambridge: Cambridge University Press.

[69] Mineo, C., 2015. Automated ndt inspection for large and complex geometries of composite materials. PhD. University of Strathclyde Glasgow.

[70] Cooper, P. I. Nicholson, D. Yan, B. Wright, and C. Mineo, "Development of a Fast Inspection System for Aerospace Composite Materials - The IntACom Project," 9th International Conference on Composite Science and Technology (ICCST-9), Sorrento (Italy), 2013.

[71] Bunsell, A. R. and Renard, J., 2005. Fundamentals of Fibre Reinforced Composite Materials. Materials Today, 8(9), p.51.

[72] Cook, L., 2009. Visual inspection reliability for composite aircraft structures. Ph.D. Cranfield University.

[73] Towsyfyan, H., biguri, A., boardman, R. and blumensath, T., 2020. Successes and challenges in non-destructive testing of aircraft composite structures. Chinese Journal of Aeronautics, 33(3), pp.771-791.

[74] Adams, R. and Cawley, P., 1989. Defect types and non-destructive testing techniques for composites and bonded joints. Construction and Building Materials, 3(4), pp.170-183.

[75] Collins, D.J., 2010. Damage detection in composite materials using acoustic emission and self-sensing fibres (Doctoral dissertation, University of Birmingham).

[76] Maierhofer, C., Myrach, P., Reischel, M., Steinfurth, H., Röllig, M. and Kunert, M., 2014. Characterizing damage in CFRP structures using flash thermography in reflection and transmission configurations. Composites Part B: Engineering, 57, pp.35-46.

[77] Meola, C., Boccardi, S., Carlomagno, G., Boffa, N., Ricci, F., Simeoli, G. and Russo, P., 2017. Impact damaging of composites through online monitoring and non-destructive evaluation with infrared thermography. NDT & E International, 85, pp.34-42.

[78] Lowe, M.J.S., Neau, G. and Deschamps, M., 2004, February. Properties of guided waves in composite plates, and implications for NDE. In AIP Conference Proceedings (Vol. 700, No. 1, pp. 214-221). American Institute of Physics.

[79] M. Castaings and B. Hosten, “Guided waves propagating in sandwich structures made of anisotropic, viscoelastic, composite materials,” J. Acoust. Soc. Am., vol. 113, no. 5, p. 2622, May 2003.

[80] M. J. S. Lowe, G. Neau, and M. Deschamps, “Properties of Guided Waves in Composite Plates, and Implications for NDE,” AIP Conf. Proc., vol. 700, no. 1, pp. 214–221, Feb. 2004

[81] B. Chapuis, N. Terrien, and D. Royer, “Excitation and focusing of Lamb waves in a multilayered anisotropic plate.,” J. Acoust. Soc. Am., vol. 127, no. 1, pp. 198–203, Jan. 2010.

[82] E. Glushkov, N. Glushkova, A. Eremin, R. Lammering, and M. Neumann, “Frequency dependent directivity of guided waves excited by circular transducers in anisotropic composite plates,” J. Acoust. Soc. Am., vol. 132, no. 2, pp. 119–24, Aug. 2012.

[83] E. Glushkov, N. Glushkova, A. Eremin, R. Lammering, and M. Neumann, “Frequency dependent directivity of guided waves excited by circular transducers in

anisotropic composite plates," J. Acoust. Soc. Am., vol. 132, no. 2, pp. 119–24, Aug. 2012.

[84] S. K. Datta and A. H. Shah, Elastic Waves in Composite Media and Structures: With Applications to Ultrasonic Nondestructive Evaluation. Boca Raton: Taylor & Francis, 2008.

[85] D. Wang, L. Ye, Z. Su, and Y. Lu, "Quantitative identification of multiple damage in laminated composite beams using A0 Lamb mode," J. Compos. Mater., vol. 45, no. 20, pp. 2061–2069, Jun. 2011.

[86] C. Ramadas, M. Janardhan Padiyar, K. Balasubramaniam, M. Joshi, and C. V. Krishnamurthy, "Delamination Size Detection using Time of Flight of Anti-symmetric (A0) and Mode Converted Ao mode of Guided Lamb Waves," J. Intell. Mater. Syst. Struct., vol. 21, no. 8, pp. 817–825, May 2010.

[87] N. Hu, J. Li, Y. Cai, C. Yan, Y. Zhang, J. Qiu, K. Sakai, Y. Liu, X. Peng, and B. Yan, "Locating delamination in compositelaminated beams using the A0 Lamb mode," Mech. Adv. Mater. Struct., vol. 19, no. 6, pp. 431–440, 2012.

[88] K. Kang, H. Chun, J. Son, J. Byun, M. Um, and S. Lee, "Quantitative Accessibility of Delamination in Composite Using Lamb Wave by Experiments and FEA," Adv. Compos. Mater., vol. 20, pp. 361–373, 2011

[89] C. Ramadas, K. Balasubramaniam, M. Joshi, and C. V. Krishnamurthy, "Characterisation of rectangular type delaminations in composite laminates through B- and D-scan images generated using Lamb waves," NDT E Int., vol. 44, no. 3, pp. 281–289, May 2011.

[90] T. Kundu, S. Das, S. A. Martin, and K. V. Jata, "Locating point of impact in anisotropic fiber reinforced composite plates.," Ultrasonics, vol. 48, no. 3, pp. 193–201, Jul. 2008.

[91] R. Kazys, A. Demcenko, E. Zukauskas, and L. Mazeika, "Air-coupled ultrasonic investigation of multi-layered composite materials.," Ultrasonics, vol. 44, pp. 819– 22, Dec. 2006.

[92] H. Y. Choi, H. T. Wu, and F. Chang, "A new approach toward understanding damage mechanisms and mechanics of laminated composites due to low-velocity impact: Part II--analysis," J. Compos. Mater., vol. 25, no. 8, pp. 1012–1038, Aug. 1991.

[93] K. Diamanti, J. M. Hodgkinson, and C. Soutis, “Detection of low-velocity impact damage in composite plates using Lamb waves,” Struct. Heal. Monit., vol. 3, no. 1, pp. 33–41, Mar. 2004.

[94] H. Kaczmarek, “Lamb wave interaction with impact-induced damage in aircraft composite: Use of A0 mode excited by air-coupled transducer,” J. Compos. Mater., vol. 37, no. 3, pp. 217–232, 2003.

[95] B. I. S. Murat, P. Khalili, and P. Fromme, “Impact damage detection in composite panels using guided ultrasonic waves,” AIP Conf. Proc., vol. 1581, no. 1, pp. 286–293, Feb. 2014.

[96] B. I. S. Murat and P. Fromme, “Detection of impact damage in composite panels using guided ultrasonic waves,” Proc. SPIE, vol. 8695, pp. 1–8, Apr. 2013.

[97] Kundu, T., Das, S., Martin, S.A. and Jata, K.V., 2008. Locating point of impact in anisotropic fiber reinforced composite plates. Ultrasonics, 48(3), pp.193-201.

Chapter 2: Ultrasonic transduction and Electro-Magnetic Acoustic Transducers (EMATs)

This chapter presents an extended overview of electromagnetic acoustic transducers, covering their fundamental operating principle and listing their advantages and drawbacks. An overview of piezoelectric and laser transduction mechanism is first introduced, followed by a description of the historical advances and development of EMATs. Finally, the working principle and the transduction mechanism for EMATs is discussed.

2.1. Common methods of ultrasonic transduction

2.1.1. Piezoelectric transducers

Piezoelectric transducers are the most widely used transducers for generating ultrasonic waves as both bulk waves and guided waves. In most cases, these use lead zirconate titanate (PZT) as the piezoelectric material. They are low cost and can be provided with different sizes. When an electrical potential is applied, the piezo-element start to vibrate thus when connected to the surface of a structure, the vibration is transmitted and while interacting with the boundary conditions of the sample, guided waves are generated. the inverse phenomenon is used to detect reflected waves.

One of the main characteristics of piezoelectric transducers is that physical contact through a coupling gel is required to establish full contact, allowing the transmission of the ultrasonic wave from the piezoelectric element to the sample [1]. Alternatively, dry contact is possible, where the transducer is coupled to the sample by applying a force so that the surface of the transducer can be in partial contact with the surface of the specimen [2]. The use of this dry-coupled method, and the applied force required to prevent any transmission loss of the energy, is limited by the condition that the transduction element does not break [1]. Unfortunately, moving structures and specimens in hostile environments such as high temperatures cannot be inspected easily using regular transducers, although high-temperature piezoelectric materials have been developed [3]. There is still a need for specially designed transducers that are suitable for generating elastic waves and allowing the inspection and monitoring for any defect in these environments.

The piezoelectric effect describes the response of the piezoelectric material when subject to an applied external load. An electric charge is generated when the piezoelectric crystals (which are elements forming the transduction layer within the sensor) are subject to externally applied forces. In fact, the crystals are naturally electrically balanced but a charge is created when a load is applied thus the electrical charges is altered. This effect constitutes the operating principal of a piezoelectric detector. Conversely, when an electrical field is applied to the crystals, a strain will be generated within the piezoelectric elements allowing the transducer to vibrate leading to the generation of elastic waves known as the inverse or reverse piezoelectric effect [4].

Single crystal quartz is one of the natural materials used to manufacture piezoelectric transducers. It was historically the first material studied exhibiting the piezoelectric effect [5]. Synthetic materials such as PZT ceramics [5] in the initial state are formed of randomly oriented domains without any centre of symmetry imposing no polarity. In the presence of an externally applied electrical field and at temperatures above the Curie point, the dipoles start to align with the field lines. The polarisation of the piezoelectric elements can be defined as the dipoles maintain their alignment with respect to the electrical fields when the high temperature is removed.

The generation of the ultrasonic waves through piezoelectric transducers, shown in figure 2.1., is mainly affected by multiple parameters such as the coefficient of piezoelectric voltage, the coefficient of the piezoelectric strain and the factor of the shear coupling thickness. The ultrasonic generation efficiency can also be affected by the testing environment temperature. The frequency, size and shape and piezoelectric properties of the transducer have a strong influence on the efficiency of guided wave generation.

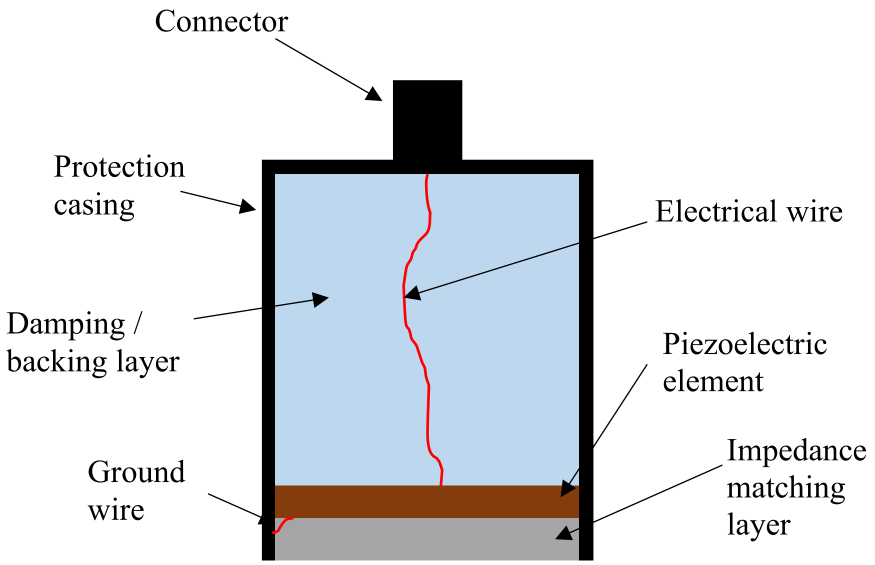

Figure 2.1. *Main components of a generic piezoelectric transducer used in ultrasonic testing inspection*

In addition to the piezoelectric and elastic properties of the piezoelectric elements, the environment temperature is critical to the operation of the transducer. In fact, when the operating temperature exceeds the Curie temperature of the piezoelectric element, the alignment of the dipoles is lost and the initial state is regained. Performance of the piezoelectric material will generally start to noticeably degrade at temperatures above half the Curie temperature, with some irreversible level of degradation. The increase in temperature leads to an increase in the internal kinetic energy of the transducer and thus the domains are no longer aligned and they become randomly oriented leading in a significant decrease in the system performances. Practically, the standard maximum operating temperature of a piezoelectric element is selected to be half of its Curie temperature. Overall, piezoelectric transducers are the most widely-used transducers for generating elastic waves in different media. Various geometries and poling directions are available (e.g. to generate shearing stress), although coupling shear stress to a sample usually requires a special couplant material and the application of a high load to push the transducer onto the sample. Various wave modes can be generated (including guided-wave modes), but there is some limited flexibility in terms of design when using piezoelectric transducers.

The design of the piezo-element is critical as that would define the operating frequency range and based on the polarization, it would affect the wave mode generated.

Conversely, EMATs, being contact-free sensors, offer greater flexibility in terms of design as different modes can be generated using the same setup. They are also contact free thus they offer a wider range of application especially in harsh environment, high temperature environment or rotating structures. In fact, the generation of guided waves using piezoelectric sensor is complicated especially for shear horizontal modes as it requires special polarisation and also a special coupling permitting the shear motion to be transmitted from the sensor to the surface of the tested sample.

In addition to that, a continuous contact is required during the inspection process, which limits the application range for such systems, such as when the sample is at a high temperature or moving. To overcome such limitations, contactless technologies have been developed, and two examples are laser ultrasonics and electromagnetic acoustic transducers (EMATs).

2.1.2. Contact-free laser-based technology for ultrasonic generation and detection

The generation of ultrasonic waves using pulsed or temporally modulated laser beams has been well-known in the industry and the research community for several years [6, 7], and similarly the use of laser interferometry [8] for detection of vibrations at the surface of a sample associated with the arrival of an ultrasonic wave. Such systems have been used for defect detection and for the characterization of various materials [9]. One of the biggest advantages of using laser-based ultrasound is the remote and contact-free nature of the technique. A distance of a few centimetres to metres between sample and laser-based equipment and optics is possible, and laser beams used for both generation and detection can also be fibre coupled.

Pulsed laser systems for the generation of elastic waves in materials and laser interferometry as a wave detector have been used to measure the elastic constants in metallic alloys over a wide range of temperatures [10, 11]. Later, laser systems were used to identify the effect of temperature variation up to 1000°C on the velocity of the longitudinal bulk waves in different media, using both a laser beam source and an interferometer detector [12]. Research has shown that laser-based systems can be used to measure ultrasonic velocity, attenuation and detection sensitivity when the temperature of the material is up to 1200°C, taking advantage of the contact-free measurement technique [13].

Although using lasers to generate and detect ultrasonic waves has numerous advantages, the method presents potential drawbacks. A highly machined and polished surface may be required to have the best sensitivity but that is not an absolute requirement as different laser technologies will tolerate a rougher surface such as the Fabry-Perot laser [14] and when two-wave mixer interferometer are used [15, 16]. The sensitivity is affected by the surface quality, as it reduces greatly when the surface roughness is increased which can be overcome if scatter is used. In addition, the sensitivity decays rapidly when the beam is projected on a dirty surface due to the laser energy being absorbed, but that is depending on different factors such as the material and the laser wavelength, and not reflected back to the detector. The polished surface is required during NDT inspection for current systems where the motion in three directions is captured; the two-wave mixer interferometer is not suitable for this operation.

The requirement of a polished and clean surface is challenging especially in an industrial environment. This makes an inspection using laser systems expensive, time consuming and demanding extra levels of preparation when compared to other inspection techniques. In order to overcome such limitations, new design of interferometer and detector have been suggested such as the Fabry-Perot detector which is less sensitive to the roughness of the inspected surface. Additionally, Fabry-Perot detectors can perform inspection without the need of a precise focusing on the specimen surface making them a suitable option to inspect challenging parts. [17, 18]. These interferometers were proven suitable in an industrial environment to inspect rough surface such as an oxidised tube wall [19].

An alternative to the system using laser both as a generator and a detector was introduced by using a pulsed laser system to generate and an EMAT for detection which both can operate in a contact-free configuration. The system was initially used to inspect a stainless-steel specimen [20, 21]. More recent work employed an EMAT formed of rare earth magnets such as the Neodymium-Iron-Boron (NdFeB) and a coil enclosed in cooled shields to allow the operation in high temperature environments. The pulsed laser beam was used as a generator, while the EMATs were used as detectors for the generated ultrasonic waves [22-26]. Switching from a laser generation and laser-based detection system to a laser-EMAT system allowed some challenges to be overcome, especially the sensitivity of laser interferometry toward the quality and the cleanliness of the inspected surface. In fact, both the pulsed laser beam generation source and the EMAT are less sensitive to the roughness of the surface compared to other generation or detection mechanisms such as piezoelectric transducers as good contact to surface is required, while providing a non-contact inspection method. Unfortunately, the operating costs of the laser system and the pre-testing tasks and procedures (health and safety concerns) limited the deployment of such systems significantly in the industrial environment compared to EMATs, which are widely used in various environments to conduct ultrasonic inspections.

In conclusion, laser-based ultrasound systems offer the advantage of being contactless compared to piezoelectric transducers for generating ultrasonic waves. The physics behind the generation of ultrasound waves using laser systems is well developed and understood allowing advancement in the generation of different waves modes by tuning the pulse parameters. However, the use of a laser system is costly and the large size of the laser systems limit their deployment in specific environments where space is restricted. In addition, if ablation is used in the generation process, there is the likelihood that damage to the material's surface could occur, and this is not desirable. Consequently, although guided waves generation using laser system is still an area of research within a lab environment, scientists have switched to a more affordable solution based on the use of electromagnetic acoustic transducers (EMATs).

2.1.3. Electro-Magnetic Acoustic Transducers

Electromagnetic acoustic transducers, as shown in figure 2.2, are transducers capable of generating ultrasonic waves within a conductive material without the need to have contact with the tested sample. EMATs do however need to be within a few millimetres of the sample surface. They are considered low-cost and highly customisable transducers that can act both as a generator and a detector of elastic waves.

In the case of non-ferromagnetic samples, the ultrasound waves are generated through the interaction of the eddy current fields in the sample generated by an alternating current through a coil generating a dynamic magnetic field and an externally applied static magnetic field [27]. In the case of ferromagnetic materials, the ultrasonic generation mechanism is more complex, as additional physical phenomena are occurring such as magnetostriction in addition to the generation of Lorentz forces. Note that this will be further developed in chapter 3 and the different mechanisms are detailed in section 2.3.

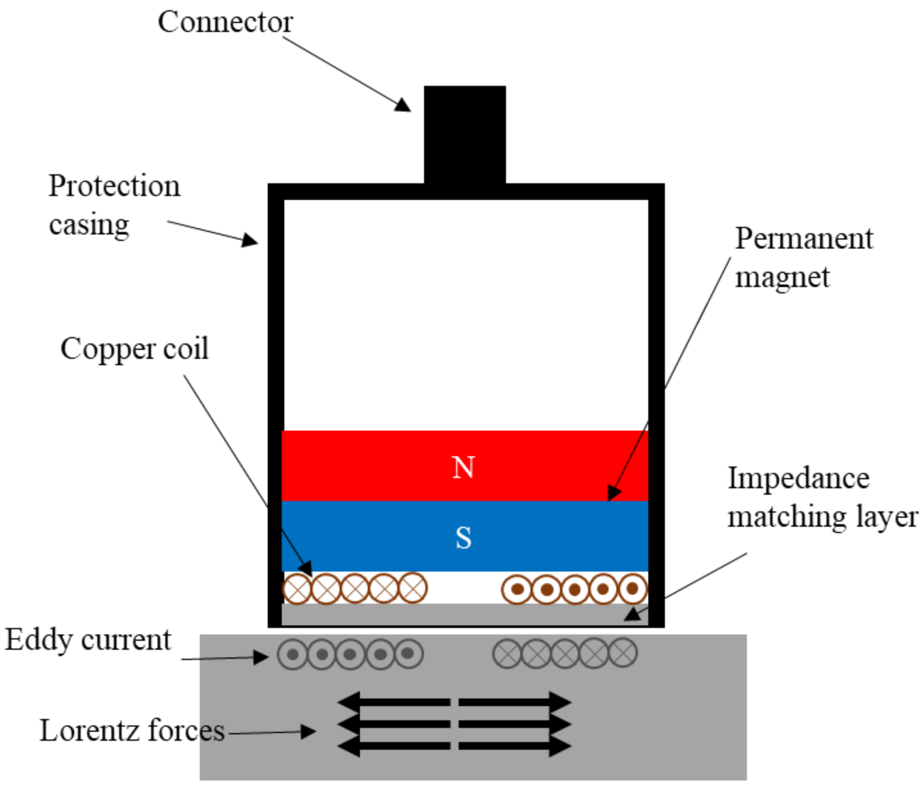

Figure 2.2. *Main components of a generic EMAT used in UT inspection*

The dynamic magnetic field is a varying magnetic field generated by placing a coil in the vicinity of the part. The field is generated by passing an alternating current through a coil. It is important to mention that the dynamic magnetic field can affect the generation of Lorentz forces in addition to the applied static magnetic field. In practice, the current amplitude is relatively high, reaching the level of up to around 1000A to increase the generated ultrasonic wave amplitude, although many systems operate at significantly lower pulsed current levels. Eddy currents are then generated by placing the RF coil near the surface of the tested sample, which will interact with a static or pseudo-static magnetic field. This static magnetic field is provided by a permanent magnet or an electromagnet in proximity of the surface of the specimen. The permanent magnet needs to be strong enough to enhance the amplitude of the generated signal, and typically an EMAT will use a rare-earth material such as the neodymium-Iron-Boron (NdFeB) [28].

The direction, amplitude and geometry of both the dynamic and the static magnetic fields need to be designed carefully so as to generate a specific ultrasonic mode within the specimen as field direction can significantly affect the generation of Lorentz forces initially and subsequently the generation of magnetostriction. These considerations offer one of the key advantages of EMATs, which is the flexibility of design and the possibility of generating specific wave modes. Within this thesis, different RF coil geometries are designed and tested, as well as various configurations of static magnetic fields.

EMAT principle of operation:

A major advantage of EMATs is their simplistic design. The coil is subject to a high amplitude RF current signal (e.g. a toneburst, an impulse or some other waveform) to generate a dynamic magnetic field in the surface of the target sample. A permanent magnet or electromagnet is used to generate a static magnetic field. In the case where the transducer is placed near to a conductive, non-ferromagnetic sample, eddy currents are generated within the skin depth of the material. The externally applied static magnetic field interacts with the generated eddy current, resulting in the generation of a body force (the Lorentz force) within the tested specimen’s skin depth, leading in turn to the generation of elastic waves for NDT applications [29-32].

The main generated Lorentz forces and associated basic EMAT design are summarized in figure 2.3 for an EMAT designed to generate normal incidence shear waves (a) and compression waves (b).

At the microscopic level, Coulomb forces are exerted on the electrons above the Fermi energy that are free to carry charge within the material, due to the dynamic magnetic field from the current flowing the coil. This forms the eddy current in the sample’s skin-depth. As the current has a direction of travel that is perpendicular to the external static magnetic field, the electrons in the eddy current are then also subject to a Lorentz force from the cross product of the eddy current density and the static magnetic field. The mathematical formulation is presented in the subsequent sections. In the case where the sample tested is ferromagnetic, additional forces are generated alongside the Lorentz forces, which are the magnetization forces and the magnetostriction forces. These forces are a physical interaction of the ferromagnetic material with the applied magnetic fields. Magnetostriction is further discussed in Chapter 3. Strictly speaking, it is the motion of the atoms that constitutes the ultrasonic wave, and the following section will describe in more detail how the Lorentz force linked to the motion of the electrons, resulting in the coherent vibration of atoms, and hence generation of an ultrasonic wave.

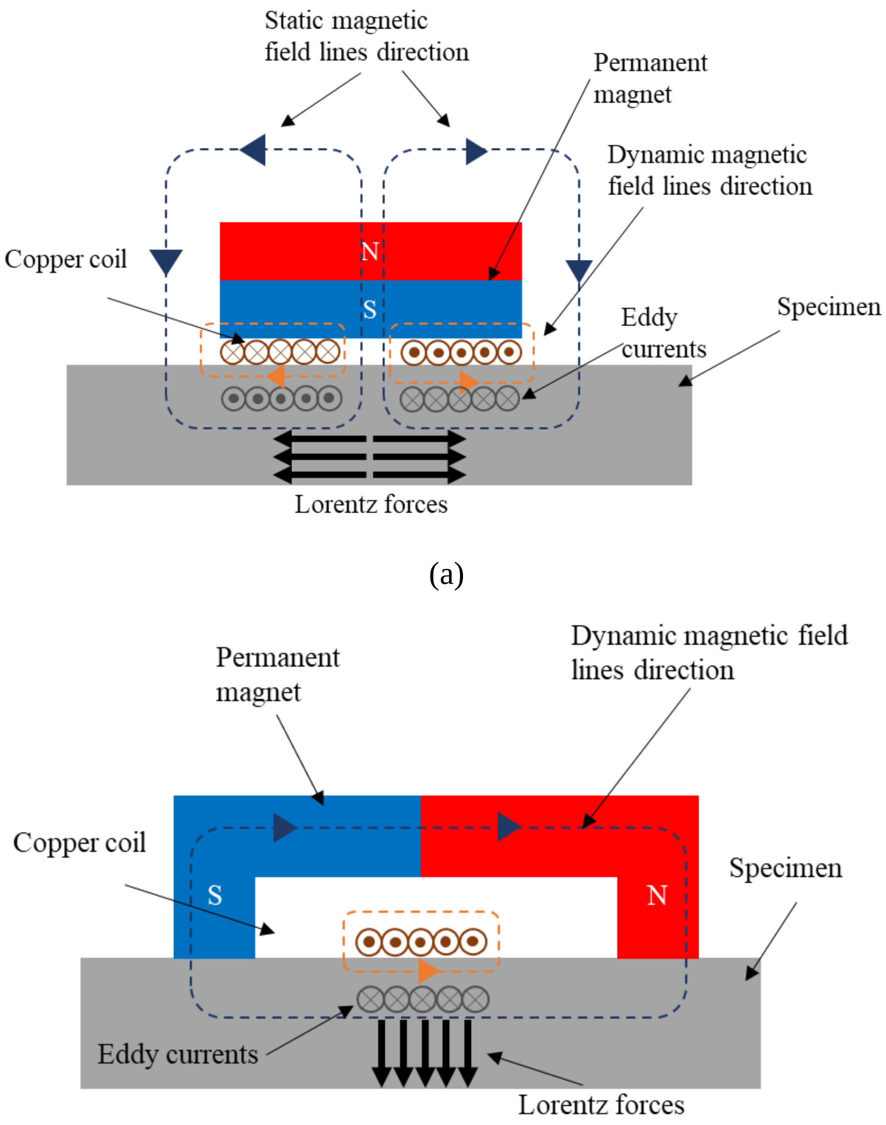

(a)

(b)

Figure 2.3. *Main coil and permanent magnet configurations to generate: (a) in plane Lorentz forces and (b) out-of-plane Lorentz forces*

History and development of EMATs

The working principle of EMATs is based on the interaction of eddy currents generated by an alternating current flowing through a coil, placed in proximity to a permanent magnet and a conductive sample. Initial studies examined the vibrational behaviour of brass by driving a low frequency current through a coil [33]. The experiment led to the generation and detection of both the longitudinal and torsional wave modes in the specimen. Later, researchers worked on determining the grain size in brass by upgrading the measurement apparatus [34]. Similarly, it was proven that the generation of longitudinal and shear waves can be optimised separately, based on the fact that the static field can be applied either parallel or perpendicular to the surface of the sample [34].

EMATs have been used for multiple applications, from material characterisation to structural health monitoring and inspection applications [35-38]. EMATs are currently a powerful method for measuring anisotropy in materials that can arise from their crystallographic texture [39] or residual stresses using directional shear waves or guided waves. They have been used inspect rail tracks [40], find hidden defects under pipe supports [41], measure high temperature piping systems [42] and find defects in stainless steel welds [43]. Some of the advantages and drawbacks of using EMATs for ultrasonic measurements are summarized in Table 2.1.

Over the last decade, major advancements in EMATs technology have been achieved. The instrumentation and the design of the actual sensor were upgraded by using models to analyse the performance of the transducer [44, 45]. Both magnetostriction and Lorentz forces generation mechanisms were included within the same framework, while multiple analytical models were established to describe the working mechanisms of the different transduction methods present within the EMAT system. This led to different applications such as the spectrometric approach [46], used for the detection of rolling texture in thin metals [47], initially at frequencies of up to 50 MHz which was later increased to 120 MHz in the case of investigating aluminium foil [48].

Table 2.1. *Advantages and drawback of EMATs*

Advantages of EMATs	Drawbacks of EMATs
• Low sensitivity to surface quality • Non-contact inspection method • Ability to generate multiple wave modes • Can operate at high temperatures in challenging environments • Ability to measure physical properties by operating a single transducer • Wideband in nature	• Limited area of application to conductive materials only • Low transduction efficiency • Low energy transfer ratio compared to piezoelectric transducers • Generated signal affected by the conductivity of the material • Complex generation mechanism for ferromagnetic materials

Dixon et al’s work has focused on the analysis and enhancement of EMAT performance by optimising different design parameters [49, 50]. Research was conducted on analysing the effect of modifying the dynamic magnetic field generated through the coil on the generation of the Rayleigh waves [51]. It was proven that by accurately modifying the orientation of just the static magnetic field applied on the sample, the Lorentz forces generated through the dynamic field can interact constructively with the static magnetic field in order to enhance the generated signal within the tested sample [52-54]. The work performed by Dixon and colleagues extended to the modelling of EMATs by trying to limit the generation of waves in the permanent magnet placed in proximity to the coil. The model described the inclusion of a conductive layer placed between the coil and the magnet which led to the generation of eddy current in the newly added component. This modification affected significantly the impedance analysis of the coil, reflecting that previous seminal work conducted by Dodd and Deeds for eddy current sensors would need to be adapted to accurately calculate the coil impedance in finite element modelling [55].

2.2. Applications and challenges of EMATs

Although EMATs offer key advantages compared to piezoelectric transducers and laser systems, the low efficiency of the transduction mechanism presents one of the major disadvantages limiting the wider use of such transducers. This lack of efficiency compared to other technologies has limited their use as ultrasonic generators and detectors, where more efficient systems can be designed and adopted [56,57]. The use of EMATs is limited due to their low transduction efficiency, particular as generators.

This is despite successful demonstrations of generation and detection of ultrasonic waves on steel samples and at high temperatures, where they do not require contact with the tested specimen [58, 59]. In addition, EMATs require advanced optimisation and design technique to enhance the signal-to-noise ratio and enhance the transduction efficiency to be applied on both the transducer (coil shape, direction of the static field) and the driving electronics [60-63].

Ultrasonic generation and detection via EMATs are not possible in non-conductive samples using the normal Lorentz force mechanisms. To overcome these limitations, the use of additional modifications is required. To provide the capability of testing non-conductive materials, conductive thin films can be attached to the sample [64]. Among these patches, magnetostrictive patches [64] are attracting more attention due to their higher sensitivity as ultrasonic generators and detector when compared to EMATs, and this approach is studied in this thesis.

2.3. Maxwell Governing Equations

The operation of EMATs is described via the Maxwell's equations (which is including the Ampere's law and the Faraday's law) [65] presented below:

$$\nabla . \vec{D} = \rho \tag{2.1}$$

$$\nabla . \vec{B} = 0 \tag{2.2}$$

$$\nabla . \vec{E} = -\frac{\partial \vec{B}}{\partial t} \tag{2.3}$$

$$\nabla . \vec{H} = \vec{J} + \frac{\partial \vec{D}}{\partial t} \tag{2.4}$$

where $\vec{D}$ describes the electric displacement vector, ρ is the free charge density, $\vec{B}$ is the magnetic flux density, $\vec{E}$ is the electric field vector, $\vec{H}$ is the strength of the magnetic field and finally $\vec{J}$ is the current density vector. A method to quantify $\vec{J}$, $\vec{D}$ and $\vec{B}$ is through using the equations below:

$$\vec{J} = \sigma \vec{E} \tag{2.5}$$

$$\vec{D} = \epsilon_0 \epsilon_r \vec{E} \tag{2.6}$$

$$\vec{B} = \mu_0 (H + M). \tag{2.7}$$

Here, σ is the corresponding electrical conductivity of the tested material, ϵ_0 and ϵ_r are the permittivity in free space and relative permittivity of the material respectively, μ_0 is the permeability in the free space and M describes the magnetization vector. The magnetic field $\vec{B}$ can be written in function of μ_0, μ_r which is the relative permeability of the material and the magnetic field strength $\vec{H}$ as follows:

$$\vec{B} = \mu_0 \mu_r \vec{H}. \tag{2.8}$$

Equations 2.1 to 2.8 describe the governing equations of the electromagnetic interaction when an EMAT is placed near a conductive material. Further equations are presented in the next section to describe the mathematical framework describing the forces generated leading to the generation of ultrasonic waves

2.4. Lorentz, Magnetization and Magnetostriction Forces

2.4.1. Lorentz Forces

Maxwell's equations [65], Faraday's law and Ampere's law construct the mathematical framework describing the generation of a magnetic field within the conductive sample, when a coil driven by an alternating current is placed close to the sample surface. The direction of the resulting through thickness averaged eddy current is generally opposed to the direction of the initial current vector, if we consider the current to effectively be acting at the sample surface. Strictly speaking the effective average eddy current can be considered to be in antiphase to the generating current. One should remember that amplitude and phase of the eddy current varies with depth, and externally one sees the resultant magnetic field of the eddy current from all depths. The Lorentz force on the electrons from the interaction between the generated eddy current and the externally applied static magnetic field can be expressed using the following equation:

$$\vec{F} = q(\vec{E} + \vec{\vartheta} \times \vec{B}) \tag{2.9}$$

where $\vec{F}$ is the Lorentz force, q is the electric charge value, $\vec{E}$ represents the electric field vector, $\vec{\vartheta}$ is the vector of the velocity of the corresponding charged particle and

$\vec{B}$ is the vector of the full applied magnetic field including the static and dynamic magnetic fields. In the case where the sample is static in terms of electrical charges, then:

$$\vec{E} = 0 \tag{2.10}$$

which simplifies the equation describing the Lorentz forces. The latter can be re-written as follows:

$$\vec{F} = q\vec{\vartheta} \times \vec{B} \tag{2.11}$$

As mentioned before, the electrical charges are subject to Coulomb forces originating from the applied dynamic electrical field through the coil and are simultaneously subject to the Lorentz forces when a static magnetic field is present, so that the general equation describing the motion of a single electron is as follows:

$$m\frac{d\overrightarrow{\vartheta_e}}{dt} = -e\left(\vec{E} + \overrightarrow{\vartheta_e} \times \vec{B}\right) - \frac{m\overrightarrow{\vartheta_e}}{\tau} \tag{2.12}$$

where m presents the mass of the electron, ϑ_e is the mean velocity of a single electron, e is the corresponding electronic charge, and τ is the average time between the electrons scattering between successive atoms or ions in the conductor, assuming that the electron loses all its momentum when scattered. The average distance between such scattering event is called the mean free path of the electron.

In the special situation where this velocity of the electron remains constant, i.e. when

$$m\frac{d\overrightarrow{\vartheta_e}}{dt} = 0 \tag{2.13}$$

then equation (2.12) can be simplified as follows:

$$-e\left(\vec{E} + \overrightarrow{\vartheta_e} \times \vec{B}\right) = \frac{m\overrightarrow{\vartheta_e}}{\tau} \tag{2.14}$$

Consider a volume of a conductive material which includes a defined value of ions density N_i,and consider the charge of an ion Z_i and $n_e$as an electron charge density . The force generated per unit volume due to the transfer of momentum can be expressed by utilising the equation 2.15 [66]:

$$\vec{F} = N_i Z_i\left(\vec{E} + \vec{\vartheta_\iota} \times \vec{B}\right) + \frac{m\overrightarrow{\vartheta_e}}{\tau} n_e \tag{2.15}$$

where $\overrightarrow{\vartheta_\iota}$ is the mean velocity of the corresponding ion. If the sample is electrically neutral, the eddy current density vector $\vec{J}$ is as follows:

$$\vec{J} = -n_e e\overrightarrow{\vartheta_e} \tag{2.16}$$

The velocity of the electrons is orders of magnitude greater than that of ions, as the ions are typically 4 orders of magnitude heavier than the electrons and the atoms have strong forces holding them in their equilibrium positions, so that equation 2.15 can be expressed as follows:

$$\vec{F} = -n_e e\overrightarrow{\vartheta_e} \times \vec{B} = \vec{J} \times \vec{B} \tag{2.17}$$

As explained above, both the static dynamic field generated from the magnet, and the dynamic magnetic field generated from the coil, interact with the sample so that in a way the sum of both magnetic fields constitutes the overall magnetic field applied to the sample. In practice, the magnetic field generated from the magnet is greater than that generated from the coil, and thus the static field has a greater effect on the generation of Lorentz forces compared to the dynamic field generated by the coil.

In conclusion, the Lorentz forces generated through the interaction of eddy currents and an externally applied magnetic field, represents the main transduction mechanism used in EMATs.

In the case of ferromagnetic materials, the applied magnetic fields have additional magnetoelastic effects on the material. These are due to magnetization which is introduced in the next subsection, and magnetostriction, which is fully developed in Chapter 3.

2.4.2. *Magnetization Force*

In the case where EMATs are used in a proximity of a ferromagnetic material, magnetization occurs within the sample, as the external magnetic field is present. Historically, the effect of magnetization on the generation of the ultrasonic waves through the use of EMATs was first investigated in the 1970s [67, 68]. The magnetization force is expressed as a function of magnetization $\vec{M}$ and the applied field $\vec{H}$ as follows:

$$\vec{F}_M = \int_V \nabla^* (\vec{\mathrm{M}}.\vec{\mathrm{H}})\,\mathrm{dv} + \frac{1}{2}\mu_0 \int_S \vec{n} M_n^2 \mathrm{dS} \tag{2.18}$$

where $\vec{F}_M$ represents the forces generated due to the magnetization, ∇^* is the nabla operator, $\vec{n}$ is the out-of-plane direction with regards to the sample surface and M_n is the magnetization vector component in the normal direction of the surface. It is important to mention that the first expression in equation 2.18, $\int_V \nabla^* (\vec{\mathrm{M}}.\vec{\mathrm{H}})\,\mathrm{dv}$ corresponds to the magnetization force and the second expression in the equation $\frac{1}{2}\mu_0 \int_S \vec{n} M_n^2 \mathrm{dS}$ corresponds to the collection of electromagnetic forces that appear on the surface of the sample and rapidly decrease in the direction of the bulk of the structure.

Original work conducted by researchers [28, 69-70] showed that in certain arrangements, the elastic waves generated from the magnetization can almost cancel those originating from Lorentz forces. Yet, waves generated from the magnetostriction presented in the next section can significantly affect the testing thus cannot be neglected.

2.4.3. *The effect of Magnetostriction*

Magnetostriction is a physical property of every ferromagnetic material [71]. It is due to the interaction of electrons, at a quantum level, leading to the alignment of the magnetic spins that constitute the magnetic domains, when an external magnetic field is applied to a ferromagnetic material, such as iron or cobalt [72]. In fact, when an external magnetic field is applied, the magnetic domains tend to align with the direction of the applied magnetic field. Through the spin of the domain, an internal strain is created leading to the extension of the dimension of the sample in the direction of the applied magnetic field.

Magnetostriction occurs in environments where the specimen temperature does not exceed its Curie temperature. If the latter is exceeded, the thermal energy would supersede the magnetic properties of the material which, by becoming paramagnetic, lose its magnetostrictive properties.

In the situation where the temperature is below the Curie temperature, the interactions leading to the magnetostriction are resumed naturally, resulting in natural changes to the ferromagnetic specimen. The process is known as the spontaneous magnetostriction.

Magnetostriction is usually defined as λ (the same symbol that is often used for wavelength) and it is equal to the ratio of the changes in length of δl to the original length in the case of ferromagnetic materials as provided below:

$$\lambda = \frac{\delta l}{l} \tag{2.19}$$

The change in length is the measurement of the specimen dimension changes after an external magnetic field is applied to the ferromagnetic sample. As an example, the equation describing the magnetostriction in an isotropic ferromagnetic material (nickel) can be written as:

$$\lambda = \frac{\delta l}{l} = \frac{3}{2}\lambda_s\left(cos^2\theta - \frac{1}{3}\right) \tag{2.20}$$

where θ is the angle between the measurement direction and the magnetization direction; λ_s is the saturation magnetostriction when the magnetostriction effect is no longer manifesting while the applied magnetic field is still increasing. The saturation magnetostriction varies between materials and is equal to -34x10^{-6} for nickel and is -7x10^{-6} for iron. As can be seen from equation 2.20, magnetostriction is dependent on the angle θ which can introduce two specific cases, i.e. where θ = 0° and θ = 90°. In the case of θ = 0°, the magnetostriction is equal to the saturation magnetostriction, whereas if θ = 90° then $\lambda = \frac{-1}{2}\lambda_s$.

Magnetostriction in ferromagnetic materials can be used to overcome some of the disadvantages of EMATs listed in section 2.3 [73-75]. Ferromagnetic materials in thin film form can exhibit high levels of magnetostriction, and can be used in conjunction with EMATs to generate ultrasonic waves in non-conductive samples.

A more in-depth analysis of the effect of magnetostriction in both ferromagnetic materials and thin film ferromagnetic materials will be introduced in the next chapter “Theory of Magnetostriction”.

2.5. Conclusions

In this chapter, some background to the operation of Electromagnetic acoustic transducers (EMATs) and their historical development has been provided. In addition, the main equations describing the three operating mechanisms (Lorentz forces, Magnetization and Magnetostriction) have also been given. The main interest to the work of this thesis is the magnetostriction effect. Chapter 3 will investigate this phenomenon in more detail, and will describe how this effect can contribute to design of transducers using thin magnetostrictive films that can be used to perform NDT operations.

References for Chapter 2

[1] D. Alleyne, P. Cawley, “The excitation of Lamb waves in pipes using dry coupled piezoelectric transducers,” Journal of Nondestructive Evaluation, vol. 15, p. 11–20, 1996.

[2] Zheng, Y., Liu, K., Wu, Z., Gao, D., Gorgin, R., Ma, S. and Lei, Z., 2019. Lamb waves and electro-mechanical impedance-based damage detection using a mobile PZT transducer set. Ultrasonics, 92, pp.13-20.

[3] Ji, W., Fang, B., Zhao, X., Zhang, S., Lu, X. and Ding, J., 2019. Enhancing electrical properties of high-Curie temperature piezoelectric ceramics BNT-PZT and their mechanism. Current Applied Physics, 19(12), pp.1367-1373.

[4] R.C. Turner, P.A. Fruierer, R.E. Newnham, T.R. Shrout, “Materials for high temperature acoustic and vibration sensors: A review,” Applied Acoustics, vol. 41, p. 299–324, 1994.

[5] Uchino, K. ed., 2017. Advanced piezoelectric materials: Science and technology. Woodhead Publishing.

[6] R.M. White. Generation of elastic waves by transient surface heating. Journal of Applied Physics, 34(12):3559–3567, 1963.

[7] C.B. Scruby, R.J. Dewhurst, D.A. Hutchins, and S.B. Palmer. Quantitative studies of thermally generated elastic-waves in laser-irradiated metals. Journal of Applied Physics, 51(12):6210 6216, 1980.

[8] C.H. Palmer and R.E. Green. Optical detection of acoustic emission waves. Applied optics, 16(9):2333–2334, 1977.

[9] C.B. Scruby and L.E. Drain. Laser ultrasonics. Techniques and applications. Adam Hilger, 1990.

[10] C.A. Calder and W.W. Wilcox. Noncontact material testing using laser energy deposition and interferometry. Materials Evaluation, 38(1):86, 1980.

[11] C.A. Calder, E.C. Draney, and W.W. Wilcox. Noncontact measurement of the elastic-constants of plutonium at elevated-temperatures. Journal of nuclear materials, 97(1-2):126–136, 1981.

[12] R.J. Dewhurst, C. Edwards, A.D.W. McKie, and S.B. Palmer. A remote laser system for ultrasonic velocity measurement at high temperatures. Journal of Applied Physics, 63(4):1225 1227, 1988.

[13] C.B. Scruby and B.C. Moss. Non-contact ultrasonic measurements on steel at elevated temperatures. NDT&E International, 26(4):177–188, 1993.

[14] Reardon, K.P. and Cavallini, F., 2008. Characterization of Fabry-Perot interferometers and multi-etalon transmission profiles-The IBIS instrumental profile. Astronomy & Astrophysics, 481(3), pp.897-912.

[15] Shcherbin, K. and Klein, M.B., 2009. Adaptive interferometers with no external field using reflection gratings in CdTe: Ge at 1550 nm. Optics communications, 282(13), pp.2580-2585.

[16] Shcherbin, K., Danylyuk, V. and Klein, M., 2013. Characteristics of two-wave mixing adaptive interferometer with CdTe: Ge at 1.06 and 1.55 μm and improved temporal adaptability with temperature control. Applied optics, 52(12), pp.2729-2734.

[17] R.J. Dewhurst and Q. Shan. Modelling of confocal Fabry-Perot interferometers for the measurement of ultrasound. Measurement Science and Technology, 5 (6):655, 1994.

[18] Cand, A., Monchalin, J.P. and Jia, X., 1994. Detection of in-plane and out-of-plane ultrasonic displacements by a two-channel confocal Fabry–Perot interferometer. Applied physics letters, 64(4), pp.414-416.

[19] J.P. Monchalin, C. Nron, J.F. Bussire, P. Bouchard, C. Padioleau, R. Hon, M. Choquet, J.D. Aussel, G. Durou, and J.A. Nilson. Laser-Ultrasonics: From the Laboratory to the Shop Floor. Advanced Performance Materials, 5:7–23, 1998.

[20] G.A. Alers and H.N.G. Wadley. Pulsed laser/electromagnetic acoustic transducer approach to ultrasonic sensor needs for steel processing. In D.O. Thompson and D.E. Chimenti, editors, Review of progress in quantitative non-destructive evaluation, Volume 6A, pages 627–638, 1987.

[21] L.R. Burns, G.A. Alers, and D.T. MacLauchlan. A compact EMAT receiver for ultrasonic testing at elevated temperatures. In D.O. Thompson and D.E. Chimenti, editors, Review of progress in quantitative nondestructive evaluation, Volume 7B, pages 1677–1683, 1988.

[22] A. Idris. Non-contact ultrasonic study on thixotropic alloys. PhD thesis, University of Warwick, 1995.

[23] C. Edwards, S. Dixon, A. Idris, J. Reed, and S.B. Palmer. Applications of non-contact ultrasonic evaluation. In D.O. Thompson and D.E. Chimenti, editors, Review of progress in quantitative nondestructive evaluation, Volume 14B, pages 2253–2260, 1995.

[24] Md.S. Rohani. The development of non-contact laser and EMAT ultrasound measurement systems for hot steel. PhD thesis, University of Warwick, 1996.

[25] I. Baillie, P. Griffith, X. Jian, and S. Dixon. Implementing an ultrasonic inspection system to find surface and internal defects in hot, moving steel using EMATs. Insight, 49(2):87–92, 2007.

[26] I. Baillie. The development of a laser-EMAT system suitable for on-line inspection in the continuous casting plant-Innovation report. PhD thesis, University of Warwick, 2008.

[27] Kawashima, K., 1976. Theory and numerical calculation of the acoustic field produced in metal by an electromagnetic ultrasonic transducer. The Journal of the Acoustical Society of America, 60(5), pp.1089-1099

[28] Hirao, M. and Ogi, H., 2003. EMATs for science and industry: noncontacting ultrasonic measurements. Springer Science & Business Media.

[29] B. W. Maxfield and C. M. Fortunko. The design and use of electromagnetic acoustic wave transducers (EMATs). Materials Evaluation, 41:1399-1408, 1983.

[30] E. R. Dobbs. Electromagnetic generation of ultrasonic waves. In W. P. Mason and R. N. Thurston, editors, Physical Acoustics, volume X, pages 127{189. Academic Press, New York, 1973.

[31] R. B. Thompson. A model for the electromagnetic generation and detection of rayleigh and lamb waves. IEEE Transactions on Sonics and Ultrasonics, SU-20(4):340{346, 1973.

[32] K. Kawashima. Theory and numerical calculation of the acoustic _eld produced in metal by an electromagnetic ultrasonic transducer. The Journal of the Acoustical Society of America, 60:1089-1099, 1976.

[33] R. L. Wegel and H. Walther, "Internal Dissipation in Solids for Small Cyclic Strains," Physics, vol. 6, pp. 141-157, 1935.

[34] R. H. Randall, F. C. Rose and C. Zener, "Intercrystalline Thermal Currents as a Source of Internal Friction," Phys. Rev., vol. 56, pp. 343- 348, Aug. 1939.

[35] Tu, J., Zhong, Z., Song, X., Zhang, X., Deng, Z. and Liu, M., 2021. An external through type RA-EMAT for steel pipe inspection. Sensors and Actuators A: Physical, 331, p.113053.

[36] Liu, T., Pei, C., Cheng, X., Zhou, H., Xiao, P. and Chen, Z., 2018. Adhesive debonding inspection with a small EMAT in resonant mode. NDT & E International, 98, pp.110-116.

[37] Liu, T., Pei, C., Cai, R., Li, Y. and Chen, Z., 2020. A flexible and noncontact guided-wave transducer based on coils-only EMAT for pipe inspection. Sensors and Actuators A: Physical, 314, p.112213.

[38] Wang, P., Zhang, Y., Yao, E., Mi, Y., Zheng, Y. and Tang, C., 2021. Method of measuring the mechanical properties of ferromagnetic materials based on magnetostrictive EMAT characteristic parameters. Measurement, 168, p.108187.

[39] Potter, M., Dixon, S., Morrison, J. and Suliamann, A., 2006. Development of an advanced multimode automatic ultrasonic texture measurement system for laboratory and production line application. Ultrasonics, 44, pp.e813-e817.

[40] Li, Y., Liu, Z., Miao, Y., Yuan, W. and Liu, Z., 2020. Study of a spiral-coil EMAT for rail subsurface inspection. Ultrasonics, 108, p.106169.

[41] Clough, Matthew, Fleming, Matthew and Dixon, Steve M. (2017) Circumferential guided wave system for pipeline screening using shear horizontal ultrasound. NDT & E International, 86 . pp. 20-27.

[42] Lunn, N., Dixon, S. and Potter, M., 2017. High temperature EMAT design for scanning or fixed point operation on magnetite coated steel. NDT & E International, 89, pp.74-80.

[43] Petcher, P. and Dixon, S., 2015. Weld defect detection using PPM EMAT generated shear horizontal ultrasound. NDT & E International, 74, pp.58-65.

[44] W. P. Mason, R. N. Thurston and A. D. Pierce, Physical Acoustics,' Principles and Methods. London: Academic Press, 1990.

[45] H." Ogi, "Field dependence of coupling efficiency between electromagnetic field and ultrasonic bulk waves," J. Appl. Phys., vol. 82, pp. 3940-9, 10/15. 1997.

[46] A. Migliori and J. L. Sarrao, Resonant Ultrasound Spectroscopy. Chichester: Wiley, 1997.

[47] K. Kawashima, "Nondestructive characterization of texture and plastic strain ratio of metal sheets with electromagnetic acoustic transducers," J. Acoust. Soc. Am., vol. 87, pp. 681-90,02. 1990.

[48] K. Kawashima and O. B. Wright, "Resonant electromagnetic excitation and detection of ultrasonic waves in thin sheets," J. Appl. Phys., vol. 72, pp. 4830-9, 11115. 1992.

[49] Jian, X. and Dixon, S., 2007. Enhancement of EMAT and eddy current using a ferrite back-plate. Sensors and Actuators A: Physical, 136(1), pp.132-136.

[50] Ren, W., He, J., Dixon, S. and Xu, K., 2018. Enhancement of EMAT's efficiency by using silicon steel laminations back-plate. Sensors and Actuators A: Physical, 274, pp.189-198.

[51] Jian, X., Dixon, S., Grattan, K.T.V. and Edwards, R.S., 2006. A model for pulsed Rayleigh wave and optimal EMAT design. Sensors and Actuators A: Physical, 128(2), pp.296-304.

[52] X. Jian, S. Dixon, K. T. V. Grattan, and R. S. Edwards. A model for pulsed Rayleigh wave and optimal EMAT design. Sensors and Actuators: A Physical, 128(2):296-304, 2006.

[53] S. Dixon and S. B. Palmer. Wideband low frequency generation and detection of Lamb and Rayleigh waves using electromagnetic acoustic transducers (EMATs). Ultrasonics, 42(10):1129-1136, 2004.

[54] X. Jian, S. Dixon, R. S. Edwards, and J. Reed. Coupling mechanism of electromagnetic acoustical transducers for ultrasonic generation. The Journal of the Acoustical Society of America, 119(5):2693-2701, 2006.

[55] X. Jian, S. Dixon, and S. B. Palmer. In-plane and out-of-plane particle velocity measurement using electromagnetic acoustical transducers. IEEE Ultrasonic Symposium, pages 1276-1279, 2005.

[56] R J. Dewhurst, C. Edwards and S. B. Palmer; Appl. Phys. Lett. 49, pp 374 – 376 (1986).

[57] D. A. Hutchins, F. Hauser and Thomas Goetz; IEEE Trans Ultrasonics UFFC-33, pp 478 - 483 (1986).

[58] D. R. Bilson, C. Edwards, M. S. Rohani and S. B. Palmer; Rev. Prog. in QNDE. 15, pp 2281 - 2287 (1995).

[59] P. Crowther, C. Edwards, S. B. Palmer and S. D. Kenney; Insight 39, pp 618 - 622 (1997).

[60] S. Dixon; PhD Thesis; Warwick University (1995).

[61] Liu, J., Liu, S., Zhang, C., Jin, L. and Zhao, G., 2022. A New Focused EMAT Design With Narrow Magnet to Achieve Both A0-Lamb Signal Enhancement and Waveform Distortion Correction. IEEE Sensors Journal, 22(15), pp.14786-14798.

[62] Boonsang, S. and Dewhurst, R.J., 2005. Signal enhancement in Rayleigh wave interactions using a laser-ultrasound/EMAT imaging system. Ultrasonics, 43(7), pp.512-523.

[63] Wu, J., Tang, Z., Yang, K. and Lv, F., 2019. Signal strength enhancement of magnetostrictive patch transducers for guided wave inspection by magnetic circuit optimization. Applied Sciences, 9(7), p.1477.

[64] Liu, Z., Zhong, X., Xie, M., Liu, X., He, C. and Wu, B., 2017. Damage imaging in composite plate by using double-turn coil omnidirectional shear-horizontal wave magnetostrictive patch transducer array. Advanced Composite Materials, 26(sup1), pp.67-78.

[65] J.C. Maxwell, “On physical lines of force,” vol. 21, 1861.

[66] J.V.F. Hernandez, “Pulsed-electromagnet EMAT for high temperature applications,” Ph.D. Thesis, The University of Warwick, 2011.

[67] R.B. Thompson, “Mechanisms of electromagnetic generation and detection of ultrasonic Lamb waves in iron – nickel alloy polycrystals,” Journal of Applied Physics, vol. 48, no. 12, 4942-4950, 1977.

[68] R.B. Thompson, “A model for the electromagnetic generation of ultrasonic guided waves in ferromagnetic metal polycrystals,” IEEE Transactions on Sonics and Ultrasonics, vol. 25, no. 1, p. 7 15, 1978.

[69] Whittington, K.R., 1978. Ultrasonic testing at high temperatures. Physics in Technology, 9(2), p.62.

[70] S. S. Lee and B. Y. Ahn. EMAT application at high temperature. Non-destructive Testing and Evaluation, 7(1):253-261

[71] Lee, E.W., 1955. Magnetostriction and magnetomechanical effects. Reports on progress in physics, 18(1), p.184.

[72] Eisberg, R. and Resnick, R., 1985. Quantum physics of atoms, molecules, solids, nuclei, and particles (p. 864).

[73] Thompson, R.B., 1976. Strain dependence of electromagnetic generation of ultrasonic surface waves in ferrous metals. Applied Physics Letters, 28(9), pp.483-485.

[74] M. B. Gitis; Soviet Physics - Solid State; 14, pp 2992 - 2995 (1973).

[75] Hanabusa, M., Kushida, T. and Murphy, J.C., 1973. Electromagnetic generation of ultrasonic waves in 3-d transition metals. Journal of Applied Physics, 44(11), pp.5106-5110.

Chapter 3: The Magnetostriction phenomenon

This thesis describes the use of magnetostrictive thin films in ultrasonic guided wave NDT applications. The first section of this chapter will provide an explanation of the different physical aspects involved in magnetostriction. This is followed by an overview of the properties of thin magnetostrictive films and a review of their applications

3.1. Magnetism and ferromagnetic material

Magnetism is defined as the combination of changes and interactions occurring in a material which may be subject to an applied magnetic field. Magnetic materials can be classified under multiple forms based on the atomic magnetic moment coupling. Examples include paramagnetic, ferromagnetic, antiferromagnetic or ferrimagnetic materials. Paramagnetic behaviour occurs when the atomic magnetic moments are randomly orientated and their sum at the level of the bulk material is zero when no external magnetic field is applied. This is due to the fact that they don't have a specific order or orientation at the bulk material level. The magnetic susceptibility χ (dimensionless in S. I. Units) of paramagnet materials is within the range of 10^{-5} to 10^{-2} and the magnetization level in such material is considered to be low.

The equations describing the magnetic flux density and the magnetic susceptibility in a magnetic material are:

$$\chi = \frac{M}{H} \tag{3.1}$$

$$B = \mu_0(H + M) \tag{3.2}$$

where M is the magnetization, H is the applied magnetic field, B is the magnetic flux density and μ_0 is the permeability in the free space $\mu_0 = 4\pi \times 10^{-7}$ Hm^{-1}.

When the magnetic moments are coupled at the atomic level, the resulting magnetic states can be described as ferromagnetic, antiferromagnetic or ferrimagnetic as presented in figure 3.1. A system will adopt a state that has the lowest free energy for particular conditions, and the underpinning reasons for why a system adopts a particular magnetic state is tied up in the quantum mechanics and thermodynamics of that system. Magnetic materials will generally exhibit a range of different magnetic states as temperature and/or applied magnetic field are varied. A common feature for these materials is that they can also exhibit a level of magnetic arrangement when an external magnetic field is absent, which means that the sum of the magnetic atomic moments when an external magnetic field is absent can be different from zero, except in the case of antiferromagnetic materials (figure 3.1). The thin films used in the present work are ferromagnetic [1], where the orientation of the magnetic spins for a ferromagnetic material remains parallel even when there is no external applied magnetic field applied. When used below the material's Curie Temperature, χ ranges from 10^1 to 10^4; at higher temperatures, χ drops significantly to the 10^{-5} to 10^{-3} range. At these levels of susceptibility, the material is no longer ferromagnetic and becomes paramagnetic.

When an external magnetic field is applied to a ferromagnetic material, the magnetic dipoles tend to align with the applied field direction. This effect is limited to a value known as saturation magnetization, where all the magnetic dipoles of a ferromagnetic material are fully aligned with the field. The saturation magnetization can be obtained mathematically by multiplying the number of atoms constituting a material per volume unit by the magnetic moment of each atom. In the case of isotropic material, the saturation magnetization remains the same in all directions; and it may be different only if the material exhibits a level of magnetic anisotropy.

By definition, the magnetic moment is formed by considering the spinning of the electron in an orbital motion. A material is ferromagnetic when all the magnetic moments are parallel and aligned in the same direction (figure 3.1(a)). The situation for an antiferromagnetic material is shown in figure 3.1(b), where the dipole moments are antiparallel and tend to cancel each other out.

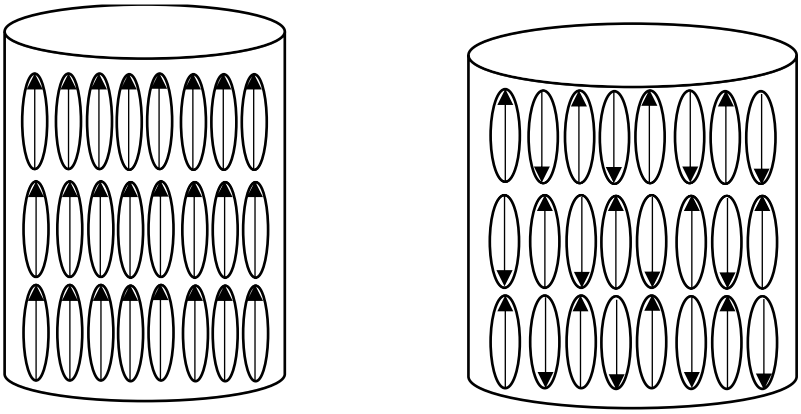
(a) (b)

Figure 3.1. *A simple representation for the magnetic moments within (a) a ferromagnetic material and (b) an antiferromagnetic material.*

3.2. Origins of magnetostriction

When an external magnetic field is applied to a ferromagnetic material, the dimensions of the sample change, a phenomenon known as magnetostriction described by λ [2]. This can be defined as:

$$\lambda = \frac{\delta l}{l_0}, \tag{3.3}$$

where Δl is the fractional change in dimension observed in the material when the magnetic field is applied, and l_0 is the original length with no magnetic field present. This is the *Joule effect* [3], which was first reported 1842, where λ can be either positive or negative. In the case where the observed change of length is positive, $\Delta l > 0$ and λ is positive, and conversely, when $\Delta l < 0, \lambda$ is negative. The *Villari effect* [4] is the inverse of the Joule effect, and is observed when stress is applied to a ferromagnetic material so that the magnetisation of the material changes. There are other variations that have been reported: The *Wiedemann effect* [5] is associated with the torsional interaction of the ferromagnetic material with an applied magnetic field. It is mainly observed when an external magnetic field generated by a passing current in the proximity of the material which leads to a rotated magnetisation around the axis similar to the applied current. Its inverse is known as the *Matteucci effect*, where changes are induced by mechanically-induced twisting.

3.3. Governing Equations for Magnetostriction

3.3.1. Spontaneous Magnetostriction

It was defined previously that magnetostriction can be either positive or negative [1], but it can also be spontaneous or induced. Although spontaneous magnetostriction is usually a negligible effect in ferromagnetic materials, it is described here for completeness. To explain this effect, consider a material which is initially above the Curie Temperature (and is thus paramagnetic). In developing the argument, we assume that the material will be isotropic and there is no external stress, and the domains are randomly shaped. If the temperature now drops below the Curie temperature, ferromagnetism conversion is initiated. In fact, at the beginning of the change from a paramagnetic material to a ferromagnetic material, a magnetisation occurs spontaneously as the magnetic dipoles are formed. The ordering of the newly formed magnetic domains engenders an internal strain and thus spontaneous magnetostriction, which occurs in a specific direction. Although magnetostriction is occurring spontaneously, the bulk magnetostriction value of the specimen remains equal to zero.

In order to mathematically model the magnetostriction [2, 6], a single magnetic domain in the form of a sphere of a radius 1 is considered when no magnetic field is applied. When the magnetic field is applied, the sphere is elongated with the main axis parallel to the direction of the applied magnetic field, as shown in figure 3.2. The saturation of the magnetostriction is denoted by e. If a random point P is considered at a random angle θ overlapping on the radius of the sphere thus, it will be elongated to the new point P’ along the X axis as shown in the figure 3.2. In addition to that, a new point P’’ can also be considered which is the elongation of the point P along the main axis OA. The direction of the strain generating the spontaneous magnetostriction is in an offset angle compared to the direction of the magnetisation in each domain. The equation describing the angle θ between the strain and the magnetisation (based on the geometrical representation obtaining the distance PP’’) in a single domain in an isotropic material can be written as follows shown in the figure below :

$$\frac{\delta l}{l} = ecos^2\theta \tag{3.4}$$

where e represents the strain generated spontaneously when a material is transformed from a paramagnetic material to a ferromagnetic material.

In the case of a polycrystalline sample, the spontaneous magnetostriction λ_0 associated with the spontaneous strain generated when a material is transformed from a paramagnetic material to a ferromagnetic material. In fact, the magnetic domains are oriented at random orientations, and thus the spontaneous magnetostriction λ_0 can be obtained by averaging Eq.3.4 [2]:

$$\lambda_0 = \int_0^{\frac{\pi}{2}} ecos^2\theta sin\theta d\theta$$

$$\lambda_0 = e \int_0^1 x^2 dx \text{ where } x = cos\theta \tag{3.5}$$

$$\lambda_0 = e \left| \frac{x^3}{3} \right|_0^1$$

Then, equation (3.5) can be further simplified considering that all domains are randomly oriented thus θ variation is negligible and the variation in all directions would remain the same:

$$\lambda_0 = \frac{e}{3} \tag{3.6}$$

Assuming that the material is isotropic, the magnetic domains are randomly distributed with equal probabilities in all directions. It is important to mention that the internal strain generating the magnetostriction occurs randomly in all directions in such a way that the overall volume of the sample remains constant.

3.3.2. Magnetostriction in isotropic materials

The material forming the patch used in the thesis is in the ferromagnetic state and thus the field-induced magnetostriction is the dominant effect. Figure 3.2 illustrates what happens when a magnetic field is applied, so that the magnetic domains become aligned up to the point at which magnetic saturation is reached.

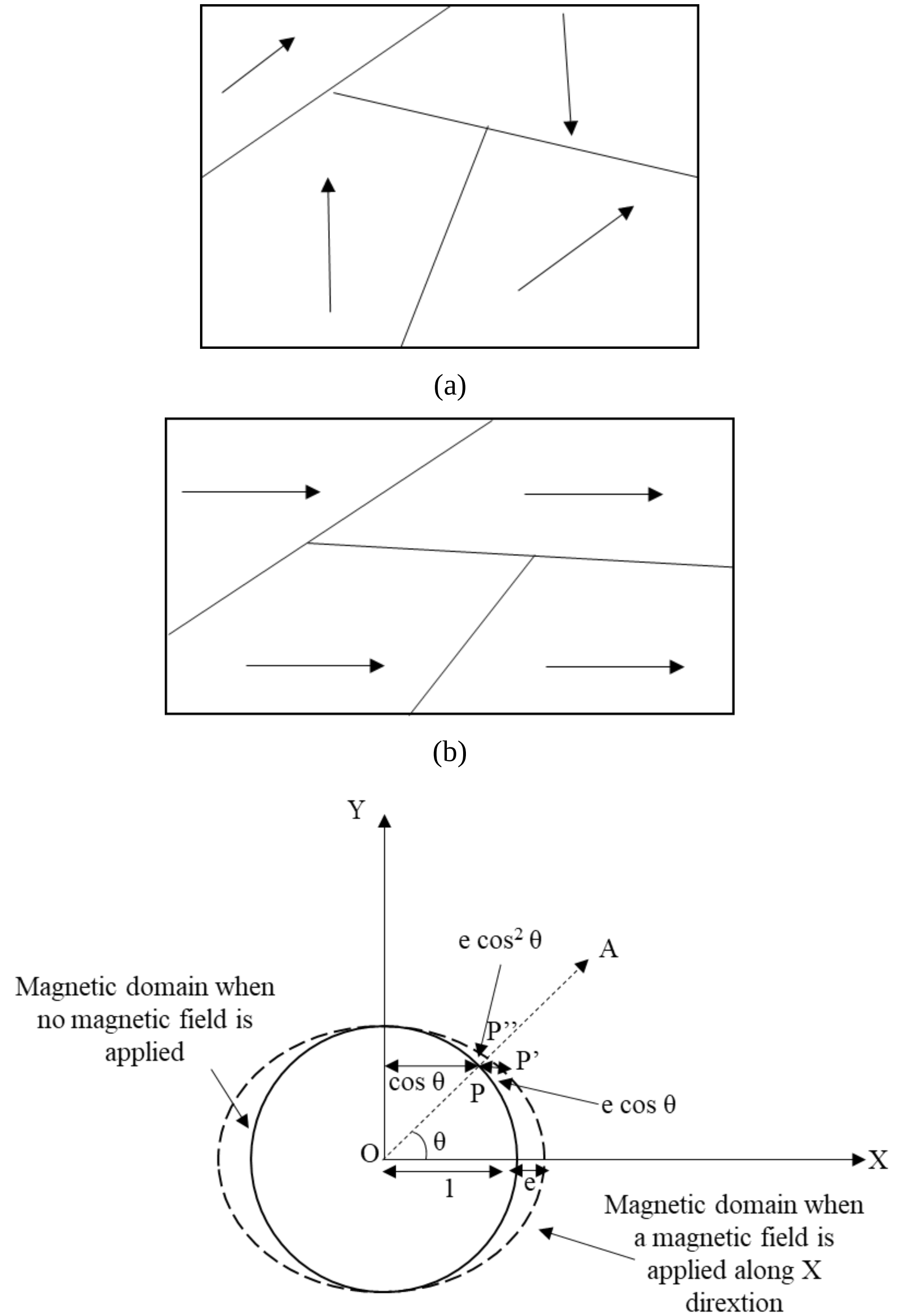
(a)

(b)

(c)

Figure 3.2. *Illustration showing the magnetostriction induced by an external magnetic field: (a) magnetic domains in a ferromagnetic material without any external magnetic field applied and (b) the effect of applying a static magnetic field and the geometrical representation of a single magnetic domain at both states when no magnetic field is applied and when a magnetic field is applied (dotted line) [2].*

When the material is magnetically saturated, all magnetic domains are aligned in the same direction as the applied magnetic field. This led to the strain being generated in parallel to the applied magnetic field. Then, the magnetostriction can be calculated using the following equation:

$$\lambda = \lambda_s - \lambda_0 \tag{3.7}$$

Equation (3.6) gives λ_0 and hence the magnetostriction can be further written as follows:

$$\lambda = e - \frac{e}{3} = \frac{2}{3}e \tag{3.8}$$

$$e = \frac{2}{3}\lambda$$

where λ is the ratio of magnetostriction, λ_s is the saturation magnetostriction and λ_0 is the spontaneous magnetostriction

By using the set of equations (3.6) – (3.8), the spontaneous magnetostriction can be calculated by knowing the saturation magnetostriction. In fact, as presented by Lee [7], the magnetostriction is remaining constant when θ is varied for angles between 0º and 180º. In addition to that, is assumed that the vectors of magnetization are equally distributed in space. Thus, the mean value of $cos^2\theta$ when the vectors are distributed and forming a sphere is equal to $\frac{1}{3}$. Based on all the assumptions, the field induced magnetostriction $\lambda_s(\theta)$ can be written in function of θ as follows:

$$\lambda_s(\theta) = \frac{3}{2}\lambda_s(cos^2\theta - \frac{1}{3}) \tag{3.9}$$

when magnetostrictive material is used in practice, the external magnetic field can be applied either in any direction relative to the sample. If $\lambda_{s/\!/}$ is the magnetostriction parallel to the main alignment direction and $\lambda_{s\perp}$that perpendicular to it, then we can write [6]:

$$\lambda_{s/\!/} = \lambda_s(\theta = 0º) = \frac{3}{2}\lambda_s\left(cos^2(\theta = 0) - \frac{1}{3}\right) = \lambda_s$$
$$\lambda_{s\perp} = \lambda_s(\theta = 90º) = \frac{3}{2}\lambda_s\left(cos^2(\theta = 0) - \frac{1}{3}\right) = -\frac{\lambda_s}{2} \tag{3.10}$$
$$\lambda_{s/\!/} - \lambda_{s\perp} = \lambda_s + \frac{\lambda_s}{2}$$

As the material studied is an isotropic material, then the fractional change in strain generated through the magnetostriction can be deduced from the equations (3.8) and (3.10) as follows:

$$\lambda_{s/\!/} - \lambda_{s\perp} = e. \tag{3.11}$$

3.3.3. Magnetostriction in magnetically anisotropic materials

In practice, ferromagnetic materials exhibit a magnetisation easy axis. The easy axis is the direction in which the minimum energy is needed to align the magnetic moments. The direction of this axis depends on the crystallographic structure and shape (demagnetisation factor) of the material. When an external magnetic field is applied to the bulk sample, the alignment of magnetic moments can change. In fact, when the applied magnetic field is rotated from the initial direction, the amplitude of the rotation of the domains can vary and would not remain the same in all directions. This is called magnetic anisotropy. In practice, most ferromagnetic materials contain a certain level of anisotropy; thus, the equations describing magnetostriction in an isotropic material are no longer valid, and the saturation magnetostriction needs to be defined based on the magnetisation direction. In the case of a single crystal cubic structures the magnetostriction occurring in the <100> or the <111> directions can be defined as λ_{100} and λ_{111} respectively. The saturation magnetostriction in a single domain is provided by equation (3.12) [6]:

$$\lambda_s = \frac{3}{2}\lambda_{100}\left(\alpha_1^2\beta_1^2 + \alpha_2^2\beta_2^2 + \alpha_3^2\beta_3^2 - \frac{1}{3}\right) + 3\lambda_{111}(\alpha_1\alpha_2\beta_1\beta_2 + \alpha_2\alpha_3\beta_2\beta_3 + \alpha_3\alpha_1\beta_3\beta_1) \tag{3.12}$$

where α_i (i = 1, 2 or 3) are the cosine of the direction following which the saturation of the magnetic moments is occurring relative to the applied field direction and β_i are the cosines of the direction following which the magnetostriction was measured relative to the applied magnetic field. λ_{100} and λ_{111} are the saturation magnetostriction values in the directions <100> and <111> respectively.

3.4. Magnetostrictive patch materials

3.4.1. Iron-Cobalt Alloys based Magnetostrictive patches

Materials such as the Terfenol-D ($Tb_{0.3}Dy_{0.7}Fe_2$) and the Galfenol (Iron and gallium alloy) are well known as highly magnetostrictive materials. The saturation magnetostriction for these materials is higher than other common materials such as iron. Although Terfenol-D or Galfenol exhibit relatively good magnetic properties, their application is still limited as they are considered brittle materials [8]. The limited mechanical properties excluded the ability for these materials to be used as thin patches in the required NDT applications.

Studies on bulk material Fe-Co alloys have shown that high magnetostriction levels are possible [9, 10]. The highest magnetostriction values were recorded for $Co_{0.7}Fe_{0.3}$. More recent work showed that magnetostriction can be enhanced by modifying the structure so that it has almost zero anisotropy [11, 12]. Since the reporting of those results, more work was conducted on the iron-cobalt alloys with an equal composition distribution between iron and cobalt to the point where the saturation magnetostriction can reach up to 150 ppm [13, 15]. $Co_{0.7}Fe_{0.3}$ alloy shows similar magnetostriction levels compared to the Galfenol, but offers better mechanical properties for the production of thin samples that could be used as thin removable patches for NDT applications. In this thesis, a commercially available iron-cobalt alloy was used as the patch material.

3.4.2. Applications of magnetostrictive thin patches

Magnetostrictive thin films are used in microelectromechanical systems (MEMS), acting as transducers for multiple subsystems such as the microactuators [16-19]. Magnetostrictive patches can also be used in contactless control, remote operations that don’t require wiring, and can be used for actuation systems in low temperature environments. Due to their compatibility with electronics, these patches can be integrated as part of the manufacturing process, using the Joule effect without the need for direct contact [20-24]. To be suitable for this application, the magnetostrictive material should have low magnetisation saturation levels [25]. Alternatively, the Villari effect allows the material to be used in sensing applications [26].

For ultrasonic NDT, the most widely used transducers for generation and detection are piezoelectric devices. Those systems have numerous limitations as their design flexibility is limited and due to their design, the operational frequency range is restricted. Further investigations focused on piezocomposite thin films but the latter didn’t solve issues related to the amplitude of the generated waves and the need for direct wiring to the transducer to be controlled [27]. This led researchers to investigate alternative technologies such as the magnetostrictive patch transducers (MPTs) to generate and detect guided waves [28-30]. These show high level of sensitivity, and provide the capability to perform the inspection without the need for direct wiring access to the active transducing element (the patch). MPTs are easy to implement and they offer great design flexibility and low manufacturing cost [31]. Practically, MPTs are used on samples of any type of material and research has shown that the patches are able to provide higher transduction efficiency than in the case where EMATs only are used [32].

MPTs are flexible, and thus can be applied to curved structures such as pipes or plates. In the case of pipes or rods, as shown in figure 3.3, the patches are attached usually on the outer diameter of the pipe, as rectangular patches or custom-designed shapes as presented in figure 3.4. Torsional waves which are non-dispersive were easily generated by attaching the patches around the circumference of a pipe, compared to the need for complex and expensive design or piezoelectric array transducers that need clamping to the pipe under tension if they are required to generate the same type of waves [33]. The design flexibility of piezoelectric transducers is limited, and thus multiple sensors are required and advanced hardware and a voltage pulsing unit is used to synchronise the generation of the waves from the array of piezoelectric transducers. In addition to torsional waves, longitudinal wavs in pipes were generated using magnetostrictive patches [34]. As the waves travelling in a circular-shaped pattern, the

Wiedemann effect was mainly used to generate the waves [35-39]. Furthermore, MPTs were used to inspect rods [40], shafts [41] and mechanical attachment for pipelines [42]. Additionally, extensive work was conducted on the data post-processing for defect detection and successful imaging of defects was reported . In fact, a single-mode waveform mode extraction method combined with spatial waveforms of the pipes during arbitrary time steps was used to reconstruct an image of the defect using guided waves generated through MPTs [43]. In a different application to detect thickness reduction due to corrosion, the reflection from torsional waves was used to detect any inconsistencies related to the pipe wall thickness. The reflected torsional waves signal will have no phase changes thus making the inspection methods more straightforward [44]. A different configuration to detect defect was by employing an array of segmented magnetostrictive patches generating SH waves allowing a dual inspection of the pipe both axially and circumferentially [45-48].

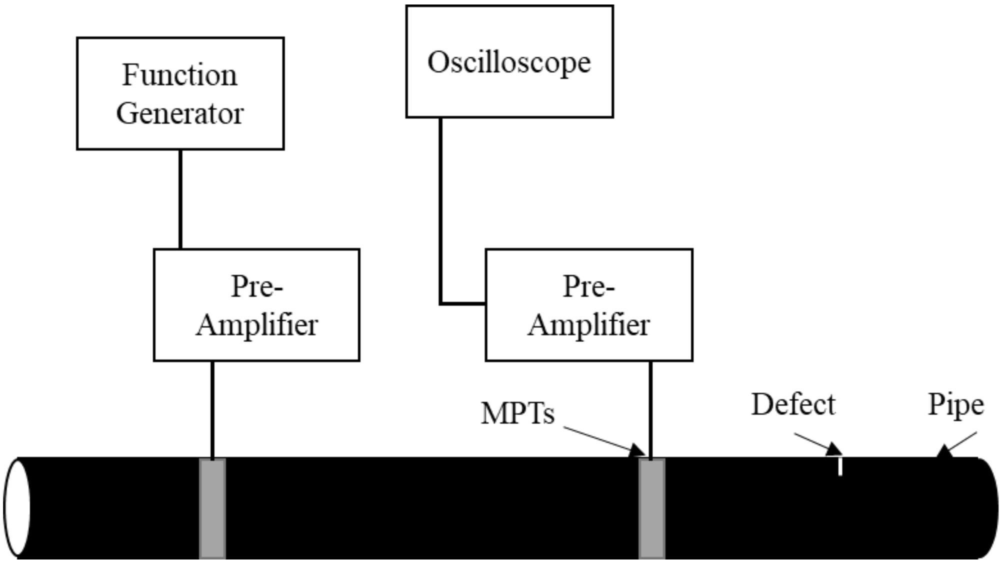

Figure 3.3. *Generic experimental setup to detect a defect using magnetostrictive patch attached to a pipe generating torsional waves as reported in [36]*

Although the Wiedemann effect was mostly used to generate waves in cylindrically-shaped structures, researchers reported the use of the Joule effect for the inspection of different structures [49-51] and to design an in-situ system for defect detection [54]. These used different patch geometries, as illustrated in figure 3.4. The magnetic patch shapes shown in the figure below were used to generate torsional waves in pipes.

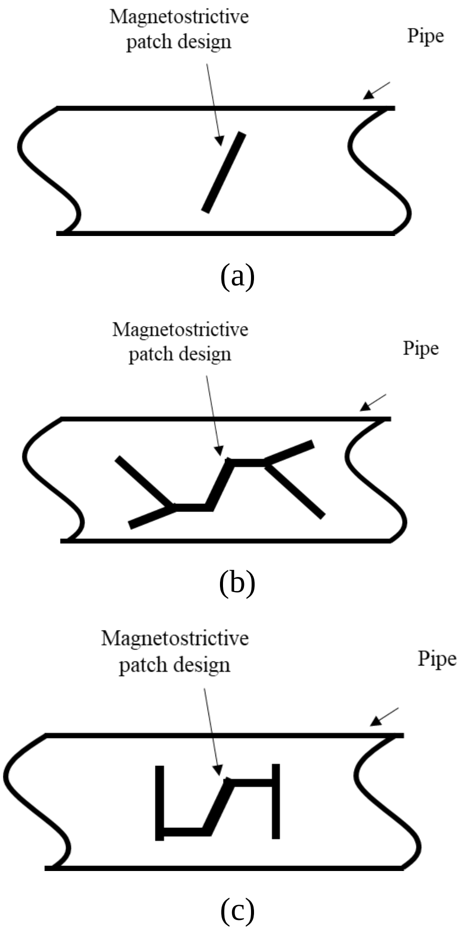

(a)

(b)

(c)

Figure 3.4. *Examples of shapes of custom-designed magnetostrictive patches showing (a) the rectangular regular strip [47], (b) V-shaped strips [48] and (c) patch design in a Z-shape [52]*

The use of MPTs on plates has been reported for some time to generate guided waves for long range inspection on plates using a magnetostrictive patch combined with a coil and permanent magnet [53]. MPTs were used on plates to generate guided waves either as unidirectional waves [54-58] or omnidirectional waves [59, 60], and can also be used for bulk waves [61, 62]. The use of MPTs in plates was extended to be used in elasticity modulus calculations [63], not only for NDT applications but also for structural health monitoring systems [64-66]. Other aspects that have been investigated include impedance matching [64], concentration of the applied magnetic field [65], and the use of arrays of sensors to enhance the generated waves [66].

In recent years, researchers were interested in applying magnetostrictive material on composite structures either by applying the material on the surface of the structure or embedded within the composite sample. In fact, researchers used modified magnetostriction patches to inspect composite plates in an array configuration. They used a dual design coil distributed in a circular shape to detect defects in a 16-plies composite plate. The magnetostrictive patch with the coil and the magnet system were applied at the surface of the composite plate [67]. Conversely, Embedded magnetostrictive materials were mainly used for inductive heating applications as they can provide a conductive medium to generate heat within the composite structure while also providing an active element to conduct structure monitoring for defect development [68]. Within the work reported in the thesis, a magnetostrictive patch transducer will be used to investigate the effect of modifying the input parameters controlling magnetostriction on the generation of different guided waves modes in composite plates as work within this area is very limited.

3.5. Contribution of this thesis

It will be seen from the above that magnetostriction is relatively well-understood in some ways, and that MPTs have been investigated for many ultrasonic measurement systems. However, it is also evident in looking at the literature that there are still many gaps in knowledge. One example is the complicated interaction of static and dynamic magnetic fields that can be used for generation. The work included in this thesis will contribute to the understanding of how magnetostriction can respond to the changes in direction and amplitude of the applied magnetic fields and the driving frequency of the dynamic magnetic field for an FeCo alloy. In addition, the behaviour of the various guided wave modes that could be generated in a plate have not been studied, as a result of changing these parameters. To date, researchers have not taken full advantage of the properties provided by magnetostrictive patches, including the high level of responsiveness of the material and the design flexibility for multiple mode generation. In order to generate guided waves, magnetostrictive patches are required to be subject to both a dynamic magnetic field generated by a Radio frequency (RF) coil and a static magnetic field. This interaction and the guided waves that result, are studied in subsequent chapters.

References for Chapter 3

[1] Shimizu, M., 1977. Ferromagnetism in iron, cobalt, nickel and their alloys. Physica B+C, 91, pp.14-23.

[2] Chikazumi, S., 2010. Physics of ferromagnetism. Oxford: Oxford Univ. Press.

[3] Joule, J. P. On a new class of magnetic forces. Ann. Electr. Magn. Chem. 8, 219-224, (1842).

[4] Villari, E. Change of magnetization by tension and electric current. Ann. Phys. Chem. 126, 87-122, (1865).

[5] Wiedemann, G. Uber die torsion und die beiziehung derselben zum magnetismus. Pogg. Ann. 106, 161-201, (1860).

[6] Jiles, D., 2017. Introduction to magnetism and magnetic materials. [Place of publication not identified]: CRC Press.

[7] Lee, E.W., 1955. Magnetostriction and magnetomechanical effects. Reports on progress in physics, 18(1), p.184.

[8] Guruswamy, S., Srisukhumbowornchai, N., Clark, A. E., Restorff, J. B. & Wun-Fogle, M. Strong, ductile, and low-field-magnetostrictive alloys based on Fe-Ga. Scripta Materialia 43, 239-244, (2000).

[9] Masiyama, Y. Magnetostriction in Cobalt-Iron alloys. Sci. Rpts. of Tohoku Imperial U. 21, (1932).

[10] Williams, S. R. The Joule magnetostrictive effect in a group of cobalt & iron alloys. Review of Scientific Instruments 3, 675-683, (1932).

[11] Hall, R. C. Single crystal anisotropy and magnetostriction constants of several ferromagnetic materials including alloys of NiFe, SiFe, AlFe, CoNi, and CoFe. Journal of Applied Physics 30, 816-819, (1959).

[12] Hall, R.C., 1960. Magnetic anisotropy and magnetostriction of ordered and disordered cobalt-iron alloys. Journal of Applied Physics, 31(5), pp.S157-S158.

[13] Cooke, M. D., Gibbs, M. R. J. & Pettifer, R. F. Sputter deposition of compositional gradient magnetostrictive FeCo based thin films. Journal of Magnetism and Magnetic Materials 237, 175-180, (2001).

[14] Domyshev, V. A., Ashchepkov, V. T., Osipov, A. Y., Kuznetsova, I. N. & Kuznetsov, N. A. Dependence of magnetostriction of iron-cobalt alloys on deformation texture, recrystallization and ordering heat-treatment. Fiz. Metallov Metalloved. 57, 1116-1121, (1984).

[15] Ishio, S. & Takahashi, M. Magnetostriction in dilute Fe-Co alloys. Journal of Magnetism and Magnetic Materials 46, 142-150, (1984).

[16] Quandt, E., Ludwig, A., Betz, J., Mackay, K. & Givord, D. Giant magnetostrictive spring magnet type multilayers. Journal of Applied Physics 81, 5420-5422, (1997).

[17] Quandt, E., Gerlach, B. & Seemann, K. Preparation and applications of magnetostrictive thin-films. Journal of Applied Physics 76, 7000-7002, (1994).

[18] T. Tanaka, S. S., M. Okada, M. Homma, and K. Arai. in International Symposium on Giant Magnetostrictive Materials and Their Applications.

[19] Honda, T., Arai, K. I. & Yamaguchi, M. Fabrication of magnetostrictive actuators using rare-earth (Tb,Sm)-Fe thin films (invited). Journal of Applied Physics 76, 6994-6999, (1994).

[20] Szymczak, H. From almost zero magnetostriction to giant magnetostrictive effects: recent results. Journal of Magnetism and Magnetic Materials 200, 425-438, (1999).

[21] Quandt, E., Ludwig, A., Betz, J., Mackay, K. & Givord, D. Giant magnetostrictive spring magnet type multilayers. Journal of Applied Physics 81, 5420-5422, (1997).

[22] Quandt, E. & Ludwig, A. Giant magnetostrictive multilayers (invited). Journal of Applied Physics 85, 6232-6237, (1999).

[23] Ludwig, A. & Quandt, E. Giant magnetostrictive thin films for applications in microelectromechanical systems (invited). Journal of Applied Physics 87, 4691-4695, (2000).

[24] Quandt, E. & Ludwig, A. Magnetostrictive actuation in microsystems. Sensors and Actuators a-Physical 81, 275-280, (2000).

[25] Quandt, E., Gerlach, B. & Seemann, K. Preparation and applications of magnetostrictive thin-films. Journal of Applied Physics 76, 7000-7002, (1994).

[26] Hristoforou, E. and Ktena, A., 2007. Magnetostriction and magnetostrictive materials for sensing applications. Journal of Magnetism and Magnetic Materials, 316(2), pp.372-378.

[27] Liu, T.; Dangi, A.; Kim, J.N.; Kothapalli, S.-R.; Choi, K.; Trolier-McKinstry, S.; Jackson, T. Flexible Thin-Film PZT Ultrasonic Transducers on Polyimide Substrates. Sensors 2021, 21, 1014.

[28] N.S. Tzannes, Joule and Wiedemann effects – the simultaneous generation of longitudinal and torsional stress pulses in magnetostrictive materials, IEEE Trans. Sonics Ultrason. 13 (1966) 33–41.

[29] R.B. Thompson, Mechanisms of electromagnetic generation and detection of ultrasonic Lamb waves in iron–nickel alloy polycrystals, J. Appl. Phys. 48 (1977) 4942–4950.

[30] R.B. Thompson, Generation of horizontally polarized shear waves in ferromagnetic materials using magnetostrictively coupled meander-coil electromagnetic transducers, Appl. Phys. Lett. 34 (1979) 175–177.

[31] H. Kwun, S.Y. Kim, J.F. Crane, Method and apparatus generating and detecting torsional wave inspection of pipes or tubes, U.S. Patent No. 6429650, 6 Aug. 2002.

[32] R. Ribichini, F. Cegla, P.B. Nagy, P. Cawley, Study and comparison of different EMAT configurations for SH wave inspection, IEEE Trans. Ultrason. Ferroelectr. Freq. Control 58 (2011) 2571–2581.

[33] Hunter, D.D., 2011. Fabrication and characterization of magnetostrictive thin films using the combinatorial method. University of Maryland, College Park.

[34] Liu, Z., Hu, Y., Fan, J., Yin, W., Liu, X., He, C. and Wu, B., 2016. Longitudinal mode magnetostrictive patch transducer array employing a multi-splitting meander coil for pipe inspection. NDT & E International, 79, pp.30-37.

[35] H. Kwun, S.Y. Kim, J.F. Crane, Method and apparatus generating and detecting torsional wave inspection of pipes or tubes, U.S. Patent No. 6429650, 6 Aug. 2002.

[36] S.H. Cho, H.W. Kim, Y. Young Kim, Megahertz-range guided pure torsional wave transduction and experiments using a magnetostrictive transducer, IEEE Trans. Ultrason. Ferroelectr. Freq. Control 57 (2010) 1225–1229.

[37] M.S. Choi, S.J. Kim, Contact SH-guided-wave magnetostrictive transducer, U.S. Patent No. 20120091829, 19 Apr. 2012.

[38] S.A. Vinogradov, Method and system for the generation of torsional guided waves using a ferromagnetic strip sensor, U.S. Patent No. 7573261, 11 Aug. 2009.

[39] Z. Liu, J. Fan, Y. Hu, C. He, B. Wu, Torsional mode magnetostrictive patch transducer array employing a modified planar solenoid array coil for pipe inspection, NDT and E Int. 69 (2015) 9–15.

[40] H. Kwun, E.C. Laiche, A.J. Parvin, Magnetostrictive sensor probe for guidedwave inspection and monitoring of wire ropes/cables and anchor rods, U.S. Patent No. 8098065, 17 Jan. 2012.

[41] H. Kwun, S.-Y. Kim, Measurement of torsional dynamics of rotating shafts using magnetostrictive sensors, U.S. Patent No. 7131339, 7 Nov. 2006.

[42] H. Kwun, S.Y. Kim, G.M. Light, Improving guided wave testing of pipelines with mechanical attachments, Mater. Eval. 68 (2010) 927–932.

[43] T. Hayashi, M. Murase, Defect imaging with guided waves in a pipe, J. Acoust. Soc. Am. 117 (2005) 2134–2140.

[44] H. Kwun, S.-Y. Kim, M.-S. Choi, Reflection of the fundamental torsional wave from a stepwise thickness change in a pipe, J. Korean Phys. Soc. 46 (2005) 1352–1357.

[45] S. Vinogradov, C. Barrera, Development of guided wave examinations of piping and tubing using magnetostrictive sensor technology, in: Proceedings of 8th International Conference on NDE in Relation to Structural Integrity for Nuclear and Pressurized Components, Berlin, Germany, Sep. 29-Oct. 1, 2010.

[46] H.W. Kim, Y.E. Kwon, S.H. Cho, Y.Y. Kim, Shear-horizontal wave-based pipe damage inspection by arrays of segmented magnetostrictive patches, IEEE Trans. Ultrason. Ferroelectr. Freq. Control 58 (2011) 2689–2698.

[46] H.W. Kim, J.K. Lee, Y.Y. Kim, Circumferential phased array of shear-horizontal wave magnetostrictive patch transducers for pipe inspection, Ultrasonics 53 (2013) 423–431.

[48] J.K. Van Velsor, R.L. Royer, S.E. Owens, J.L. Rose, A magnetostrictive phased array system for guided wave testing and structural health monitoring of pipe, Mater. Eval. 71 (2013) 1296–1301.

[49] Y.Y. Kim, C.I. Park, S.H. Cho, S.W. Han, Torsional wave experiments with a new magnetostrictive transducer configuration, J. Acoust. Soc. Am. 117 (2005) 3459–3468.

[50] C.I. Park, W. Kim, S.H. Cho, Y.Y. Kim, Surface-detached V-shaped yoke of obliquely bonded magnetostrictive strips for high transduction of ultrasonic torsional waves, Appl. Phys. Lett. 87 (2005) 224105.

[51] C.I. Park, S.H. Cho, Y.Y. Kim, Z-shaped magnetostrictive patch for efficient transduction of a torsional wave mode in a cylindrical waveguide, Appl. Phys. Lett. 89 (2006) 174103.

[52] E. Kannan, B. Maxfield, K. Balasubramaniam, SHM of pipes using torsional waves generated by in situ magnetostrictive tapes, Smart Mater. Struct. 16 (2007) 2505–2515.

[53] H. Kwun, S.-Y. Kim, G.M. Light, Long-range guided wave inspection of structures using the magnetostrictive sensor, J. Korean Soc. NDT 21 (2001) 383–390.

[54] S.H. Cho, J.S. Lee, Y.Y. Kim, Guided wave transduction experiment using a circular magnetostrictive patch and a figure-of-eight coil in nonferromagnetic plates, Appl. Phys. Lett. 88 (2006) 224101.

[55] J.S. Lee, S.H. Cho, Y.Y. Kim, Radiation pattern of Lamb waves generated by a circular magnetostrictive patch transducer, Appl. Phys. Lett. 90 (2007) 054102.

[56] J.S. Lee, Y.Y. Kim, S.H. Cho, Beam-focused shear-horizontal wave generation in a plate by a circular magnetostrictive patch transducer employing a planar solenoid array, Smart Mater. Struct. 18 (2009) 015009.

[57] L. Zhou, Y. Yang, F.-G. Yuan, Design of a magnetostrictive sensor for structural health monitoring of non-ferromagnetic plates, J. Vibroeng. 14 (2012) 280– 291.

[58] B. Yoo, S.-M. Na, A.B. Flatau, D.J. Pines, Directional magnetostrictive patch transducer based on Galfenol’s anisotropic magnetostriction feature, Smart Mater. Struct. 23 (2014) 095035.

[59] J.K. Lee, H.W. Kim, Y.Y. Kim, Omnidirectional Lamb waves by axisymmetrically configured magnetostrictive patch transducer, IEEE Trans. Ultrason. Ferroelectr. Freq. Control 60 (2013) 1928–1934.

[60] H.M. Seung, H.W. Kim, Y.Y. Kim, Development of an omni-directional shear horizontal wave magnetostrictive patch transducer for plates, Ultrasonics 53 (2013) 1304–1308.

[61] S.H. Cho, B.Y. Ahn, T.H. Heo, Magnetostrictive phased array transducer for transducing shear horizontal bulk waves, U.S. Patent No. 20130145851, 13 Jun. 2013.

[62] Y.E. Kwon, H.J. Jeon, H.W. Kim, Y.Y. Kim, Waveguide tapering for beam-width control in a waveguide transducer, Ultrasonics 54 (2014) 953–960.

[63] C. Liang, B. Prorok, Measuring the thin film elastic modulus with a magnetostrictive sensor, J. Micromech. Microeng. 17 (2007) 709–716.

[64] H.W. Kim, S.H. Cho, Y.Y. Kim, Analysis of internal wave reflection within a magnetostrictive patch transducer for high-frequency guided torsional waves, Ultrasonics 51 (2011) 647–652.

[65] K.S. Kumar, V. Murthy, K. Balasubramaniam, Improvement in the signal strength of magnetostrictive ultrasonic guided wave transducers for pipe inspection using a soft magnetic ribbon-based flux concentrator, Insight Non-Destructive Test. Condition Monit. 54 (2012) 217–220

[66] H.W. Kim, Y.E. Kwon, J.K. Lee, Y.Y. Kim, Higher torsional mode suppression in a pipe for enhancing the first torsional mode by using magnetostrictive patch transducers, IEEE Trans. Ultrason. Ferroelectr. Freq. Control 60 (2013) 562– 572.

[67] Liu, Z., Zhong, X., Xie, M., Liu, X., He, C. and Wu, B., 2017. Damage imaging in composite plate by using double-turn coil omnidirectional shear-horizontal wave

magnetostrictive patch transducer array. Advanced Composite Materials, 26(sup1), pp.67-78.

[68] Christopoulos, A., Hristoforou, E., Koulalis, I. and Tsamasphyros, G., 2014. Inductive strain sensing using magnetostrictive wires embedded in carbon fibre laminates. Smart materials and structures, 23(8), p.085035.

Chapter 4: Effect of Magnetic Field Direction on Guided Wave Mode Generation

This chapter examines the effect of different magnetic field combinations on the generation of ultrasonic signals in magnetostrictive patches. The experiments and results reported within this chapter extend the knowledge of the use of removable magnetostrictive patches, by studying their response when subject to different combinations of static and dynamic magnetic fields. The magnetic fields are generated using either coils with different geometries or permanent magnets. The interaction between the applied direct current (DC) magnetic field and the AC fields generated by the various coil configurations is investigated, and the result that this has on the generation of ultrasonic guided waves is measured. The ultrasonic generation source involves two mechanisms: magnetostriction and the Lorentz force. The results reported within this chapter provide a better understanding on how different designs for coils and permanent magnets used to drive a magnetostrictive patch can affect the generation of guided waves.

4.1. Experimental setup

Experiments were conducted to investigate the effect of applying different configurations of both the dynamic magnetic field from various coil designs and the applied static magnetic field. The experiments were designed to provide a better understanding on how the generation of guided waves modes can be modified by changing the direction and the shape of the external magnetic fields. The vibration of the magnetostrictive patch was also captured during these experiments using an optical vibrometer. Each patch was attached to the surface of the sample using 25µm thick double-sided tape. This allowed the patch to be removed after each inspection, without altering the surface quality of the sample.

Initial experiments were conducted using a glass plate as the sample in order to initially investigate vibrations generated solely within the magnetostrictive patch rather than a combination of vibrations generated by the patch and within a conductive sample. The glass plate, is a non-conductive, uniform thickness, isotropic structure, with low acoustic attenuation for the frequency range of interest. Thus, the elastic waves observed were generated by forces generated within the patch only. This approach provides a more controlled environment to observe the waves generated by magnetostriction and the Lorentz forces. The vibrations of the magnetostrictive patch for different magnetic fields in different direction and were measured on a glass plate in the first experiments, and in the following experiments, the patch was attached to a stainless-steel plate in order to study the resultant guided wave generation and propagation.

4.1.1. Experiments to study the effect of magnetic field direction on magnetostrictive thin film vibration

A schematic diagram of the experimental apparatus used to perform these investigations is presented in figure 4.1. The material used for the magnetostrictive patch was 55 µm thick VACOFLUX 48 iron cobalt alloy (®VACUUMSCHMELZE GmbH & Co, Germany). VACOFULX is characterized by a high permeability reaching up to 18000 NA^{-2}. The saturation magnetization is equal to 2.35T. The properties relevant to the experiments detailed below are summarized in Table 4.1.

Table 4.1. *Mechanical and magnetic characteristics of the magnetostrictive patch material (VACOFLUX iron-cobalt alloy)*

Young’s Modulus	200 GPa
Poisson Ratio	0.29
Density	8.12 g/cm^3
Electrical Resistivity	0.42 µΩm
Saturation Magnetostriction	70 ppm
Saturation Magnetisation	2.35 T

The square patch used had dimensions of 80mm x 80mm and was placed at the centre of a 200mm x 200mm x 3mm thick square glass plate, as shown in figure 4.1. A reflective tape was placed on the directly opposite surface to the patch, and served as a reflection medium for the laser beam from a PSV-400 3D scanning vibrometer (Polytec Inc, Germany). This was used to capture the vibrations in the glass plate directly under the patch. (Note that other experiments to be described below looked at the guided wave signals propagating away from the plate).

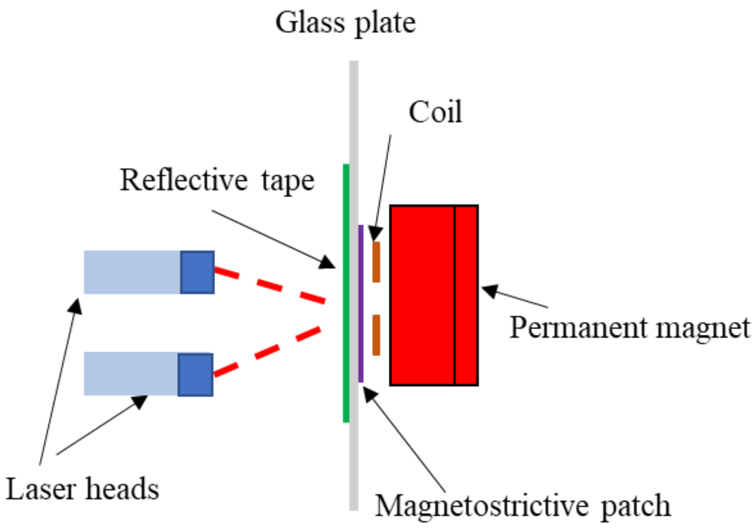

(a)

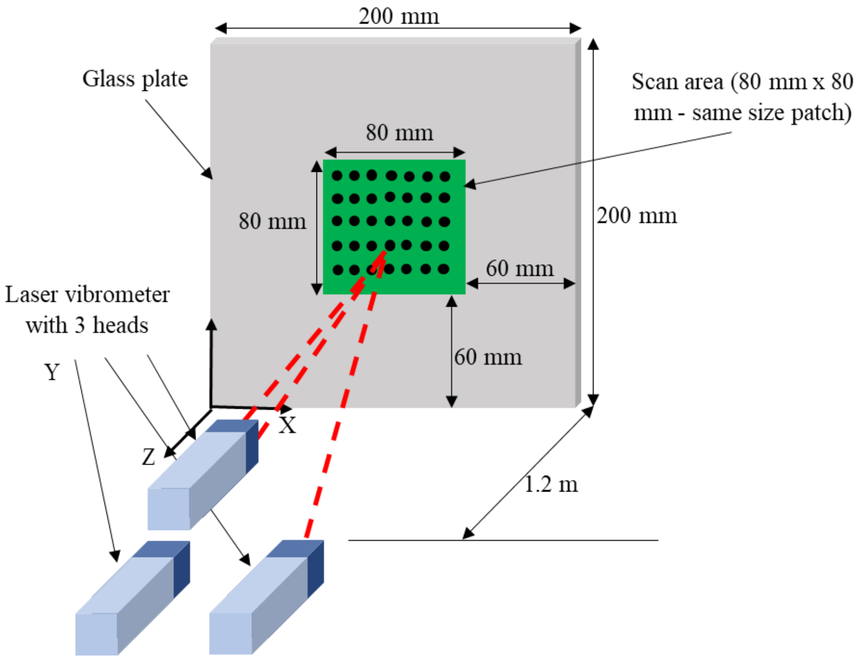

(b)

__Figure 4.1.__ (a) Side view of the measurement system showing the location of the coil, permanent magnet, magnetostrictive patch, and the reflective tape on the opposite surface of the glass plate; (b) Experimental apparatus showing the laser vibrometer heads (blue) placed in position relative to the reflective tape (green) which was attached to the opposite side of the glass plate (grey) relative to the MPT.

The main laser unit was placed at a distance of 1.2m from the surface of the glass plate. The laser system is constructed of 3 separate heads connected through a control and acquisition system. The different laser beams can detect the vibration in three directions: two orthogonal in-plane directions and one out-of-plane (directions X, Y and Z respectively). The distance separating the laser heads and the surface of the glass plate was selected based on the optimal distance to optimise the reflected energy of the laser and to ensure a good scanning resolution. The PSV-400 scanning system was programmed to directly capture the vibration occurring under the patch after excitation over the 80 mm x 80 mm scanning area.

As stated earlier, the aim of these experiments was to study the effect of different coils with different shapes on the vibrational characteristics detected directly under the patch (as in Figure 4.1) or for the guided wave studies to be described later. To achieve this, different coil shapes were connected to a high-power pulsing unit (Innerspec RF pulsing system). The electrical current generated from the pulsing unit consisted of a 1 cycle sine-like wave pulse with a 120 kHz central frequency as shown in figure 4.2. This frequency was selected to ensure that the laser system is able to capture the vibration with high precision with minimal sensitivity losses.

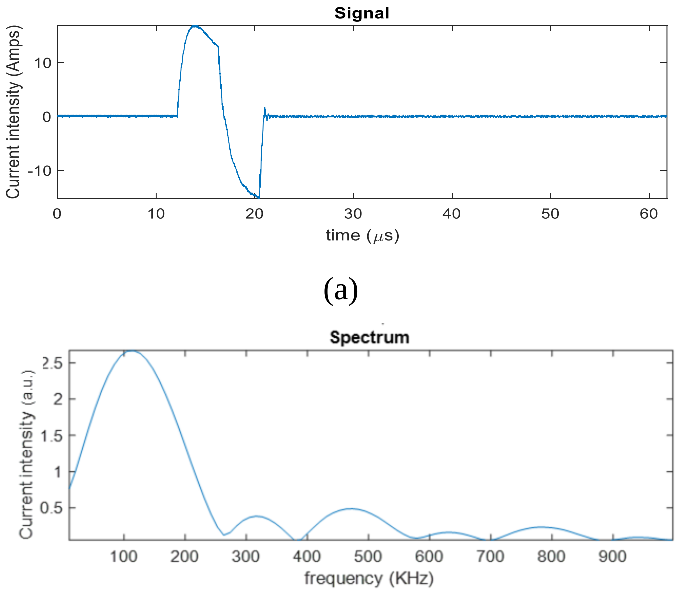

(a)

(b)

Figure 4.2. *(a) The electrical signal from the high-power pulsing unit delivered to the excitation coil and (b) the corresponding FFT of the signal.*

The key results were captured at two specific time delays of 14 µs and 22 µs. The first set of data captured was when the excitation signal delivered to the driving coil was reaching its peak. This was to observe the vibration of the patch when the input signal is at a maximum, reducing any electrical pick-up generated from the electronics of the pulsing unit. The second time step was just before the end of the pulsing window and this was to capture qualitatively the first elastic waves generated within the immediate area of the patch.

The dynamic magnetic field (B_d) applied to the magnetostrictive patch was generated through the use of a flat coil, and two main types were used: a racetrack coil and a circular pancake shaped coil. All coils were used in conjunction with a permanent magnet to generate the applied static magnetic field (B_s) needed for efficient operation. Figure 4.3 presents the different coil designs and the permanent magnet configurations that were investigated. The racetrack coil shown in figure 4.3(a) was used in conjunction with the U-shape permanent magnet (figure 4.3(b)) which generated a magnetic field parallel to the surface of the patch, while the circular permanent magnet (figure 4.3(d)) was used to generate a static magnetic field in the normal direction to the surface of the patch.

The permanent magnet was placed so that the region where the magnetic field was generated coincided with the linear area of the racetrack coil. The racetrack coil was formed of 10 turns of 1mm wide copper track, with a 0.5mm spacing between each turn. In fact, the racetrack coil was used in configurations 1 and 2. The coil was made of a printed circuit with a thickness of 35 µm. The full copper track was 14.5mm wide and the overall thickness of the PCB was 1.57mm. For the configurations 3 and 4, a circular coil was used. The circular coil had 5 turns with a 1mm wide copper track and a 0.5mm spacing. The coil was manufactured using the same PCB as the racetrack coil. The copper track thickness was 35µm while the overall thickness of the coil (copper and board backing) is equal to 1.57mm. The different configurations will be presented in greater detail in the following section.

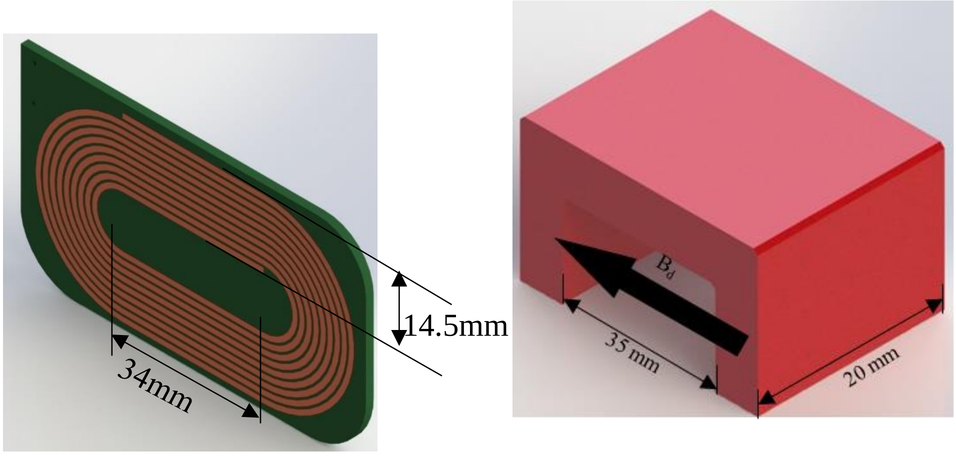

(a) Racetrack coil (b) U-shape permanent magnet

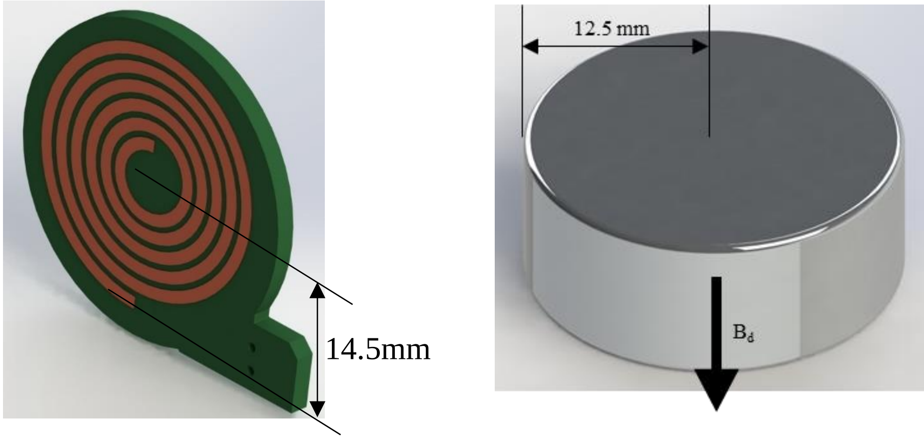

(c) Pancake coil design (d) Circular permanent magnet design

Figure 4.3. *Illustrations of (a) the racetrack coil, (b) the U-shaped Alnico permanent magnet, (c) the circular pancake coil and (d) circular permanent magnet.*

The U-shape permanent magnet was a grade 5 Alnico permanent magnet with a 1.1.T remanent magnetic field. The actual generated magnetic field was measured using a commercial gaussmeter Hirst GM08 and the amplitude of the permanent magnet measured at the centre point between the poles in air away from any other material was 210 mT. It is important to mention that the real applied in-plane magnetic field when the magnet is placed near the magnetostrictive patch will be higher, due the material’s high permeability. The cylindrical permanent magnet providing the out-of-plane static magnetic field had a remanent magnetic field of 1.3T and was measured to have an amplitude of 300 mT in air using the gaussmeter, at the surface of the magnet face that would be behind the coil.

The overall aim of these experiments was to define the vibrational response of the magnetostrictive patch when subject to different magnetic field configurations. Thus, four different configurations were studied and explored. A summary of the different configurations is presented in table 4.2 and these are illustrated in figure 4.4. The X-Y plane was parallel to the surface of the plate while the Z direction represents the out-of-plane direction i.e. perpendicular to the surface of the sample.

Table 4.2. *List of the different configurations used to analyse the response of the thin magnetostrictive patch.*

Configuration	Static magnetic field B_s	Dynamic magnetic field B_d	Coil shape
Configuration 1	X-axis	Y -axis	Racetrack
Configuration 2	X-axis	X-axis	Racetrack
Configuration 3	Z-axis	Radial (X, Y plane)	Circular - Pancake
Configuration 4	X-axis	Radial (X, Y plane)	Circular - Pancake

It should be noted that the different configurations analysed within these experiments were fundamentally different from the expected analysis of a conventional EMAT, where the design is based on the Lorentz force generation mechanism. Here, magnetostriction is expected to be the dominant generation mechanism for the generation of the elastic waves. All configurations could be rotated by 90° with respect to the patch, in order to investigate any directional dependencies due to the anisotropy of the material. The Lorentz forces in Configuration 1, where a racetrack coil and the U-shaped permanent magnet are used, would be expected to be minimal (Figure 4.4(a)), because the in-plane static magnetic field and eddy current in the sample would be in the same direction. For Configurations 2 and 3, Lorentz forces are expected to be generated in the out-of-plane direction and in the in-plane direction respectively. Configuration 2 consists of the racetrack coil and the Alnico magnet placed at 90° angle (Figure 4.4(b)). Configuration 3 had the circular coil delivering an in-plane, radially polarised, dynamic magnetic field and a circular permanent magnet generating an out-of-plane static magnetic field (Figure 4.4(c)). Configuration 4 consisted of the circular coil generating an in-plane, radially polarised, dynamic magnetic field combined with the U-shape alnico magnet inducing a permanent biasing magnetic field in one in-plane direction. The Lorentz forces generated within Configuration 4 would be expected to be of a complex pattern due to the mixture of directions of both the applied dynamic field and the applied static field (see figure 4.4(d)).

Coil and permanent magnet design and orientation

Field directions

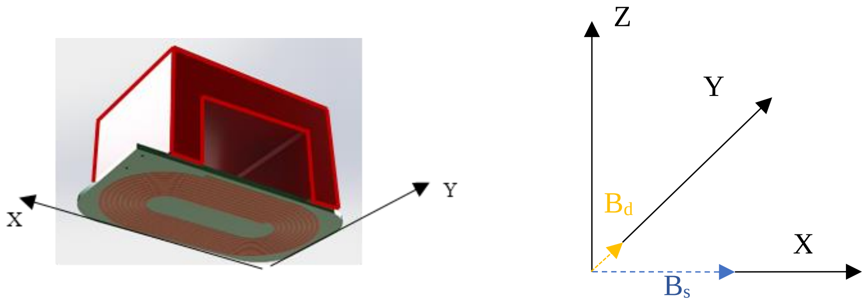

Configuration 1

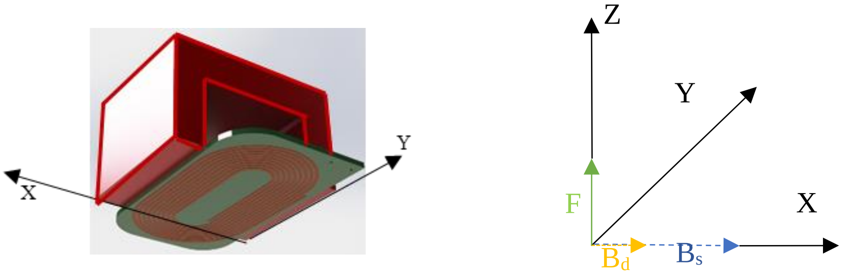

Configuration 2

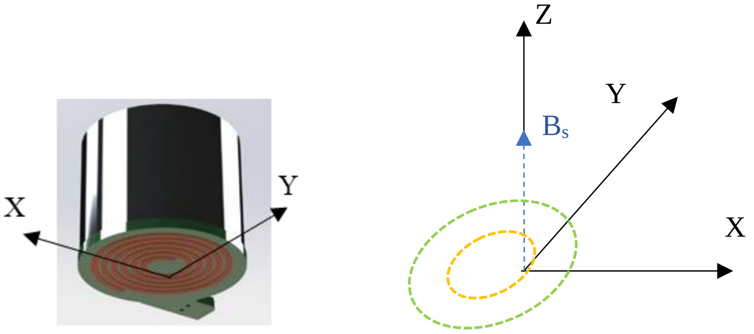

Configuration 3

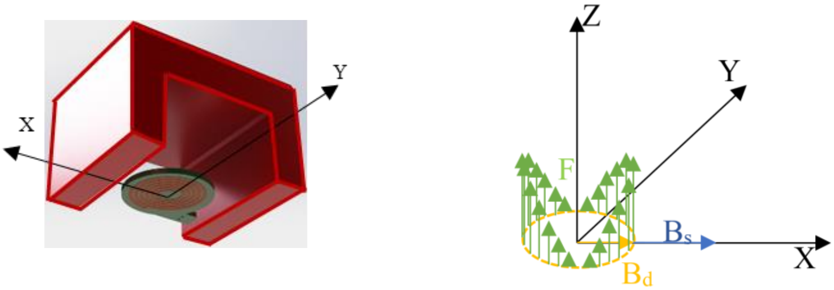

Configuration 4

Figure 4.4. *Illustration of the different configurations showing the relative positions of the coil and the permanent magnets along with the relative direction of the bias magnetic field (Yellow), the dynamic magnetic field (blue) and Lorentz forces when generated (green).*

4.1.2. Set-up for experiments on guided wave generation

These experiments were designed to explore the radial propagation of the guided waves generated by the MPT, attached to a non-magnetic stainless-steel plate (530mm x 530mm x 3mm). The experimental apparatus is presented in figure 4.5. The input signal used during these experiments consisted of 3-cycles of a 200 kHz sine wave-like, gaussian amplitude modulated signal (see figure 4.6a). This was generated using a commercial high-power system RITEC RAM-5000 unit. The selection of the frequency and the number of cycles used was to enhance the signal-to-noise ratio (SNR) of the received signal. This combination of central frequency and number of cycles allowed the capture of an accurate reflected signal. The three different guided waves modes expected in this thickness of plate (S0, SH0 and A0) were captured, permitting the calculation of their corresponding phase velocities and time of arrivals. The laser system recording window was set up to 400µs. A delay equal to 10µs was initially programmed within the RITEC system to minimise the electrical pick-up and interference with the receiving system.

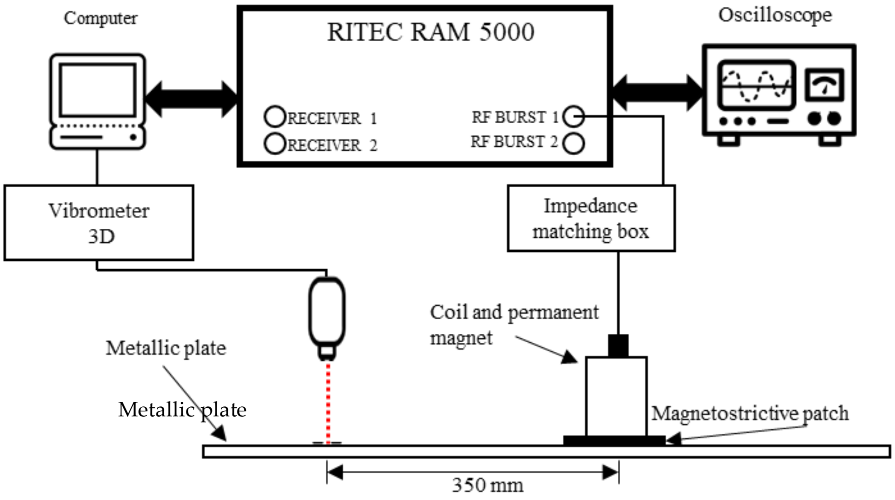

Figure 4.5. *Experimental apparatus for the guided waves generation using the MPTs*

The impedances of the different coils used were measured using the PRECISION Impedance Analyzer Agilent 4294A. The impedance analysis was conducted to measure the current driving the coil which its root mean squared was equal to 15A. The signal form, current magnitude and magnitude FFT frequency spectrum are presented in figures 4.6a and 4.6b respectively.

During these experiments, the racetrack coil and the circular coil from the previous set of experiments were used to generated the dynamic magnetic fields to investigate the generation of guided waves. The printed coil was placed on top of the magnetostrictive patch with a 0.1mm thick insulation adhesive film covering the conductive tracks on the PCB. Similar to the previous experiments, the U-shape permanent magnet was placed within the linear region of the racetrack coil. For the configurations 3 and 4, the circular coil was used. In order to detect the propagation of the guided waves, a 3D laser vibrometer system was used. The laser system was a Polytec CLV-3000 single spot laser system mounted on a robotic arm. The laser head contained 3 separate Doppler laser beams ensuring the measurement of velocity in different 3 axis (X, Y and Z). Reflective tape was attached to the metallic plate to enhance the amount of back-scattered light to the sensing heads for measuring the velocity of the vibrations coupled onto the tape from interaction with ultrasonic disturbances or waves in both the in-plane direction and the out-of-plane direction.

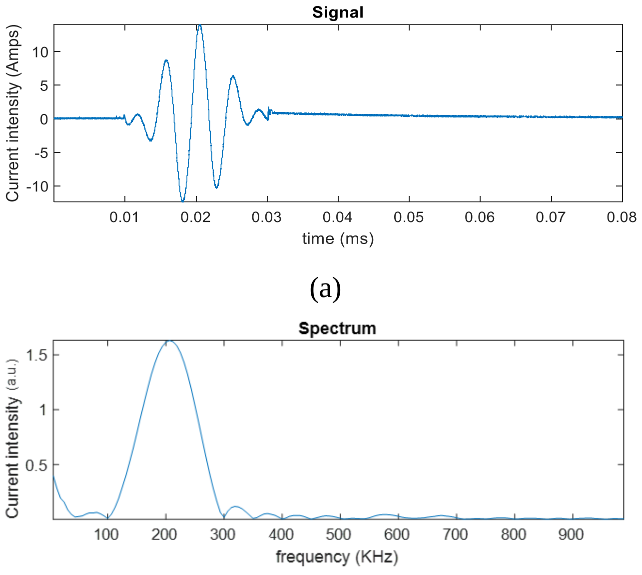

(a)

(b)

Figure 4.6. *(a) Current waveform from the RITEC RAM 5000 for GW experiments, (b) The corresponding FFT of the current signal shown in (a)*

The laser head performed a 360° circular sweep to measure the received waves at different locations. The robotic arm performed a 10° step to capture the elastic waves at different angles. The laser head as well as the relative position of the patch and the detection points are presented in figure 4.7. The detection points were placed at 350mm distance from the location of the centre of the patch. The back-scattered laser was measuring the components of the received waves at the X, Y and Z directions.

Different combinations of the applied static and dynamic magnetic fields were applied to the patch. Similar to the previous set of experiments, the dynamic fields were generated using a racetrack coil for the configuration 1 and 2. For the configurations 3 and 4, the circular coil was used to generate the dynamic field. The static magnetic field was generated using the U-shape Alnico magnetic for configurations 1, 2 and 4. A circular permanent magnet was used to generate the bias static magnetic field in configuration 3.

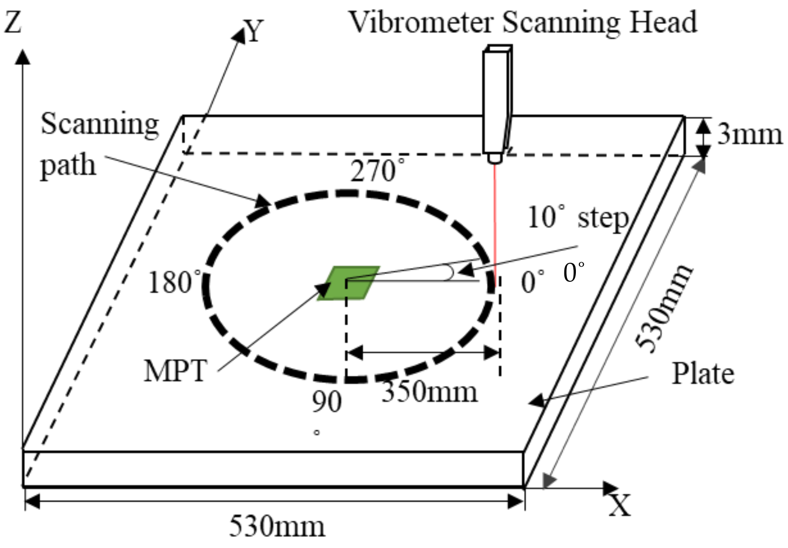

Figure 4.7. *Geometry of scan to measure GW directivity patterns*

The measurements were conducted twice with a 90° angle by rotating the coil and the permanent magnet, to investigate any anisotropy or directional effect affecting the performances of the patch.

4.2. Results

The results of both sets of experiments are described below.

4.2.1. Vibration patterns analysis of the magnetostrictive patch

The variations in magnitude of the vibrations are presented in the following figures as changes in particle velocity amplitude, as this is the quantity detected by the vibrometer. If the vibration amplitudes in the directions X, Y and Z are A_x, A_y and A_z respectively, then the overall amplitude at any one location can be calculated using equation 4.1.

$$|A| = \sqrt{A_X^2 + A_Y^2 + A_Z^2} \qquad (4.1)$$

The vibrometer was scanning over the area below the patch, as shown earlier in Figure 4.1(b), and the spatial change in |A| plotted as a function of position at a fixed time delay after the excitation pulse. The aim was to show the vibrational patterns created by the patch, then would then lead to guided wave generation.

Configuration 1

The first configuration (Figure 4.4 – configuration 1) was designed to investigate the case where the static magnetic field B_s and the dynamic magnetic field B_d were applied in the XY plane along the X direction and the Y direction respectively. The permanent magnet was placed above the linear section of the racetrack coil that generates the majority of the alternating magnetic field in the patch. As the static and dynamic magnetic fields were perpendicular to each other (static magnetic field was parallel to the induced current within the coil), Lorentz forces were not expected to be present. Thus, only magnetostriction forces would be expected to be the dominant cause of any vibrations. The patterns of vibrations for both time steps (at the time corresponding to the maximum input signal amplitude and toward the end of the pulse) are presented in Figures 4.8 (a) and (b). This shows that the maximum magnitude of the vibration is occurring just under the racetrack coil, at a time delay of 14μs after the current pulsing window started. The signal captured toward the end of the pulsing window shows the direction of the propagation of the generated elastic wave. As can be seen, the wavefront had an elliptical shape. The results show that the generated waves are travelling along the plate in a direction parallel to the applied alternating magnetic field. The collected data after the rotation of the coil and permanent magnet system by 90° with respect to the patch showed no significant effect on the amplitude or the directivity of the elastic waves generated in the thin film as shown in the table below. As it can be seen from the recorded amplitudes for different guided waves at 0º and 90º there are no major differences for S0, SH0 and A0. Some differences are due to experimental errors such as placing the sensor when rotating as the process was performed manually.

Table 4.3. *Amplitudes of the guided waves received through configurations 1-4 used to analyse the response of the thin magnetostrictive patch.*

	Configuration at an angle 0º			Configuration at an angle 90º		
	S0	SH0	A0	S0	SH0	A0
Config 1	9.62×10^{-4}	2.83×10^{-3}	2.83×10^{-4}	9.53×10^{-4}	2.32×10^{-3}	2.10×10^{-4}
Config 2	4.51×10^{-4}	2.42×10^{-3}	2.74×10^{-4}	4.08×10^{-4}	2.23×10^{-3}	2.16×10^{-4}
Config 3	$2.3\ 10^{-4}$	$1.74\ 10^{-4}$	$2.58\ 10^{-4}$	2.51×10^{-4}	1.31×10^{-4}	2.65×10^{-4}
Config 4	4.25×10^{-4}	5.23×10^{-3}	2.51×10^{-4}	4.19×10^{-4}	4.05×10^{-4}	2.2×10^{-4}

These results confirmed that there is no detectable magnetic anisotropy present within the magnetostriction patch. Similar rotation experiments were also conducted for configurations 2, 3 and 4, and the collected data confirmed that the rotation of the coil and the permanent magnet would not affect the amplitude or the patterns of the vibration.

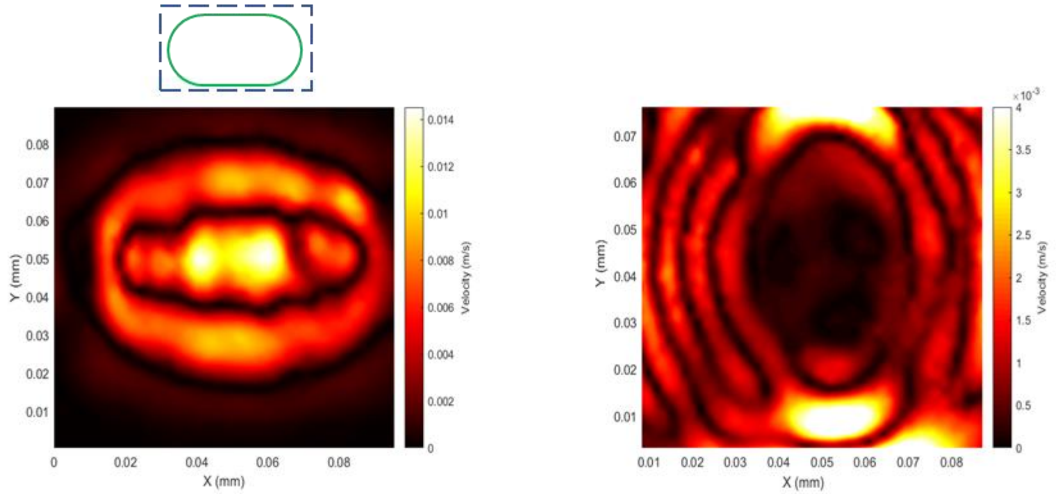

(a) (b)

Figure 4.8. *Configuration 1: Scan measuring |A| at two different time delays directly under the patch at (a) t = 14 µs and (b) t = 22 µs showing the relative positions of the coil (green) and permanent magnet (blue)*

Configuration 2

Configuration 2 (Figure 4.4 – configuration 2) has both the dynamic magnetic field, generated through the racetrack coil, and the static biasing magnetic field, generated through the U-shaped magnet, both acting in the X direction. As the figure 4.9 shows, the vibrations are occurring below the area where the forces would be generated in the patch, with a shape similar to that the of racetrack coil, with an elliptically-shaped wavefront propagating outward from the patch. The direction of travel for the generated elastic waves, for this configuration, was in the Y direction (perpendicular to the direction of both the dynamic and static applied magnetic fields). At these frequencies, such a force distribution generated with a main direction along the X axis, might be expected to favour S0 and SH0 generation. As all the forces are directed toward the X direction, S0 generation is enhanced in the same direction while the forces that are travelling in the Y direction is enhancing SH0 waves generation

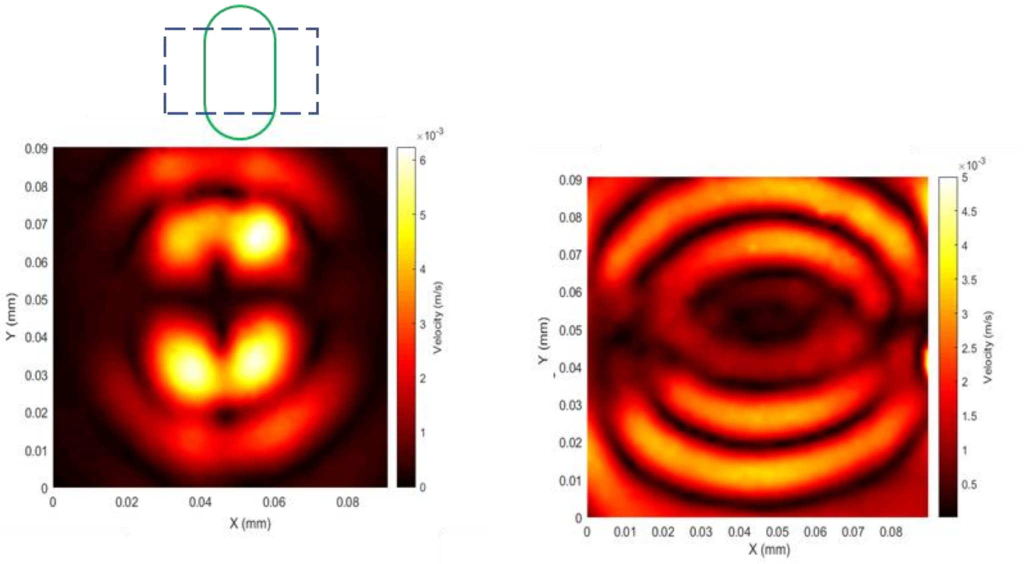

(a) (b)

Figure 4.9. *Configuration 2: Scan measuring |A| at two different time delays directly under the patch at (a) t = 14 µs and (b) t = 22 µs showing the relative positions of the coil (green) and permanent magnet (blue)*

Configuration 3

Configuration 3 contains a circular permanent magnet providing an out-of-plane static magnetic field coupled with a circular coil, generating an in-plane, radially polarised dynamic magnetic field (Figure 4.4 – configuration 3). In-plane radial Lorentz forces are expected to be generated in this configuration, alongside the magnetostriction forces. Both forces would be in phase. As can be observed in Figure 4.10, the result was a wave radiating fairly uniform in all the directions.

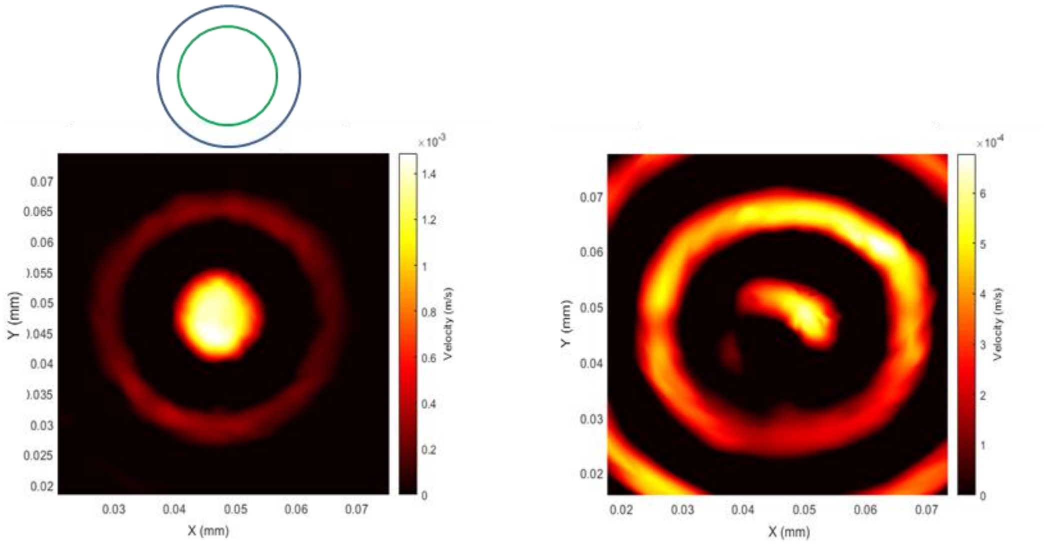

Figure 4.10. *Configuration 3: Scan measuring |A| at two different time delays directly under the patch at (a) t = 14 µs and (b) t = 22 µs showing the relative positions of the coil (green) and permanent magnet (blue)*

Configuration 4

Configuration 4 (Figure 4.4 – configuration 4) consisted of a circular pancake coil, generating a radially polarised, dynamic field, with the U-shape alnico permanent magnet generating an in-plane bias magnetic field in the X-direction. In this configuration, it was expected that the force distribution due to magnetostrictive and Lorentz forces over the area covered by the coil, would be very complex and spatially varying with a maximum amplitude at the centre line of the permanent magnet. The spatial scan of the area beneath the patch and the first elastic waves generated are presented in the Figure 4.11. A unique feature noticed in this configuration was that the initial vibrations did not have a similar shape to that of the coil used to generate the dynamic magnetic field. The initial vibrations are of an elliptical shape with the dominant axis aligned with the direction of the applied static magnetic field. The scan at the second time step shows that the elastic waves were travelling in the direction perpendicular to the applied static field.

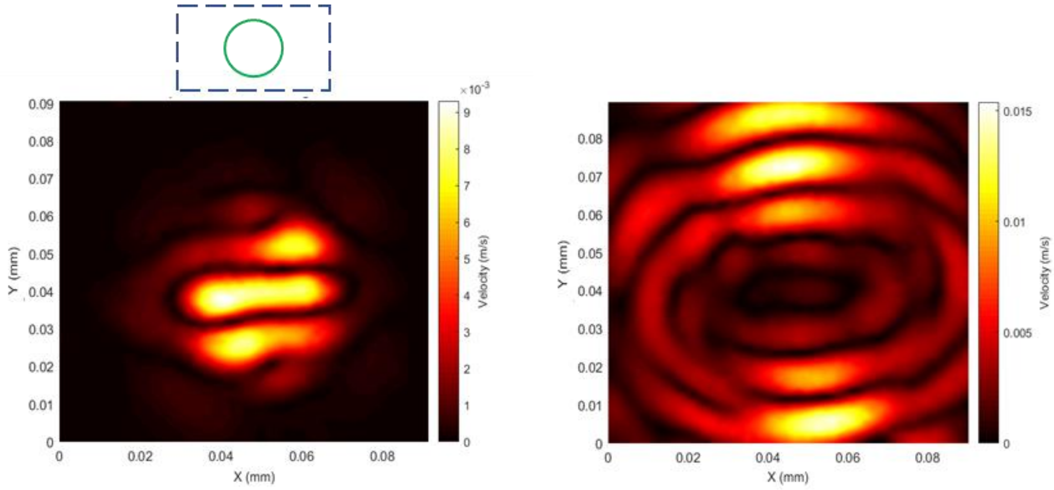

Figure 4.11. *Configuration 4: Scan measuring |A| at two different time delays directly under the patch at (a) t = 14 µs and (b) t = 22 µs showing the relative positions of the coil (green) and permanent magnet (blue)*

Configuration 4 seems to have led to a complex generation mechanism for the Lorentz forces combining shearing and twisting forces due to the complex distribution of Lorentz forces. In fact, the circular coil is generating a radial distribution of the dynamic magnetic field. This distribution will be partially parallel to the applied static field leading to the generation of the Lorentz forces. In adjacent areas, the dynamic field is perpendicular to the static field, and thus no Lorentz forces are expected. This is only valid on the centre line of the permanent magnet while in other areas, Lorentz forces are generated with different amplitudes. The variation of the interaction between the dynamic field and the static field led to the generation of the Lorentz forces in the Z-direction with varying magnitude.

4.2.2. Spatial scans of guided waves propagating in the plate

This Section shows results of guided wave propagation in a 3mm thick, non-magnetic stainless-steel plate at some distance (350 mm) from the source, where different guided wave modes could be distinguished by their group velocities. The overall aim of these experiments was to investigate the propagation of the S0, SH0 and A0 wave modes. These were the only modes expected within the frequency range used, as this is below the cut-off frequency for higher-order modes. Note that rotation of the square patch had no significant effect on the measured directivities of guided waves, suggesting that there was no significant anisotropy in the effects generated within the patch.

Dispersion curves for these three modes were calculated and are presented in figure 4.12. In addition, the phase and group velocities at the 200 kHz central frequency for S0, A0 and SH0 modes were also calculated, and are shown in Table 4.4.

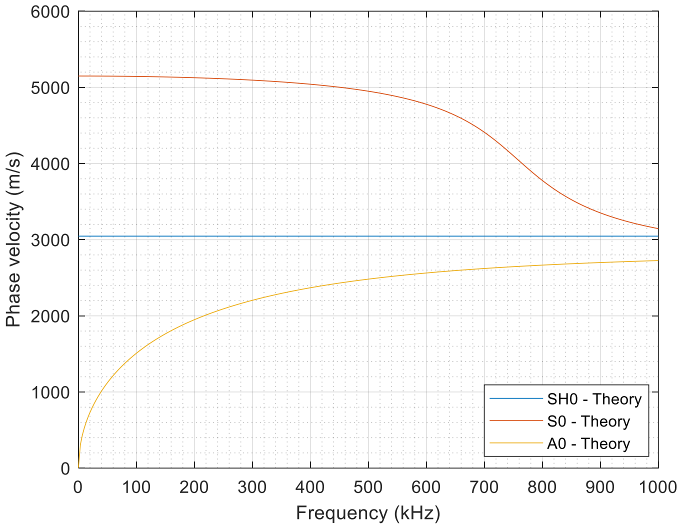

(a)

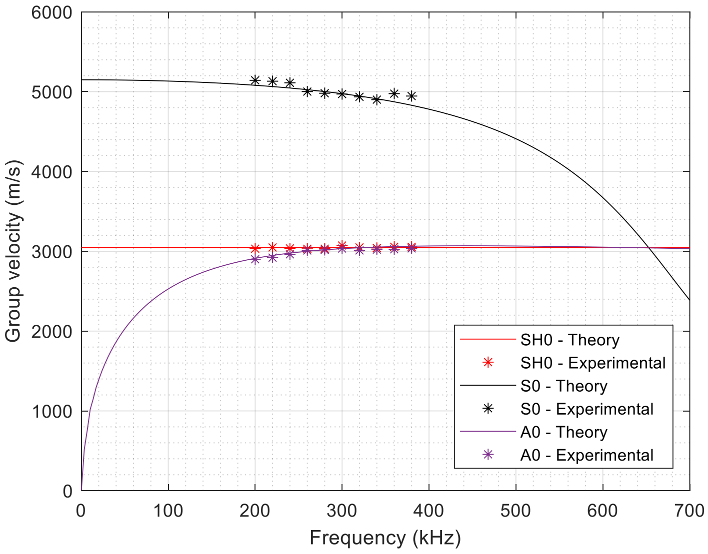

(b)

Figure 4.12. *Dispersion curves for a 3 mm thick stainless-steel plate showing the phase velocities for S0, SH0 and A0 and the group velocities for S0, SH0 and A0 obtained through mathematically and experimentally*

The curves presented in figure 4.12 were obtained using open source software (Dispersion calculator, Centre for Lightweight Production Technology Institute of Structures and Design, German Aerospace Centre) to calculate the dispersion curves for different materials. Young's Modulus, plate thickness, Poisson's ratio and the frequency range were used as input. The predictions were then compared to experimental data, with the aim of validating the software output. Both datasets are presented in figure 4.12.

Table 4.4. *Phase velocity of S0, SH0 and A0 modes at 200 kHz.*

Guided wave mode	Phase velocity (m/s)	Group velocity (m/s)
S0	5146	5141
SH0	3046	3046
A0	1950	2241

Examples of the recorded waveforms are shown in Figure 4.13. For each configuration, the angle of detection was selected for each mode to highlight a particular aspect of the directivity. It can be seen that for the Configurations 1, 2 and 3, all three waves modes (A0, S0 and SH)) were presented within a single detected waveforms at the indicated angles. For configuration 4 at 0°, only the SH0 mode can be detected, as expected from the directivity patterns, as the SH0 mode is dominant compared to the S0 and SH0 modes.

The signal wave magnitude |A| was measured at the fixed distance of 350 mm using the setup shown earlier in Figure 4.7 as a function of angle to obtain directivity plots. The radiation patterns for both the symmetrical S0 mode and the shear horizontal waves modes SH0 are illustrated in figure 4.14 for all four configurations. It can be seen from the figures that the radiation patterns are significantly different for each configuration.

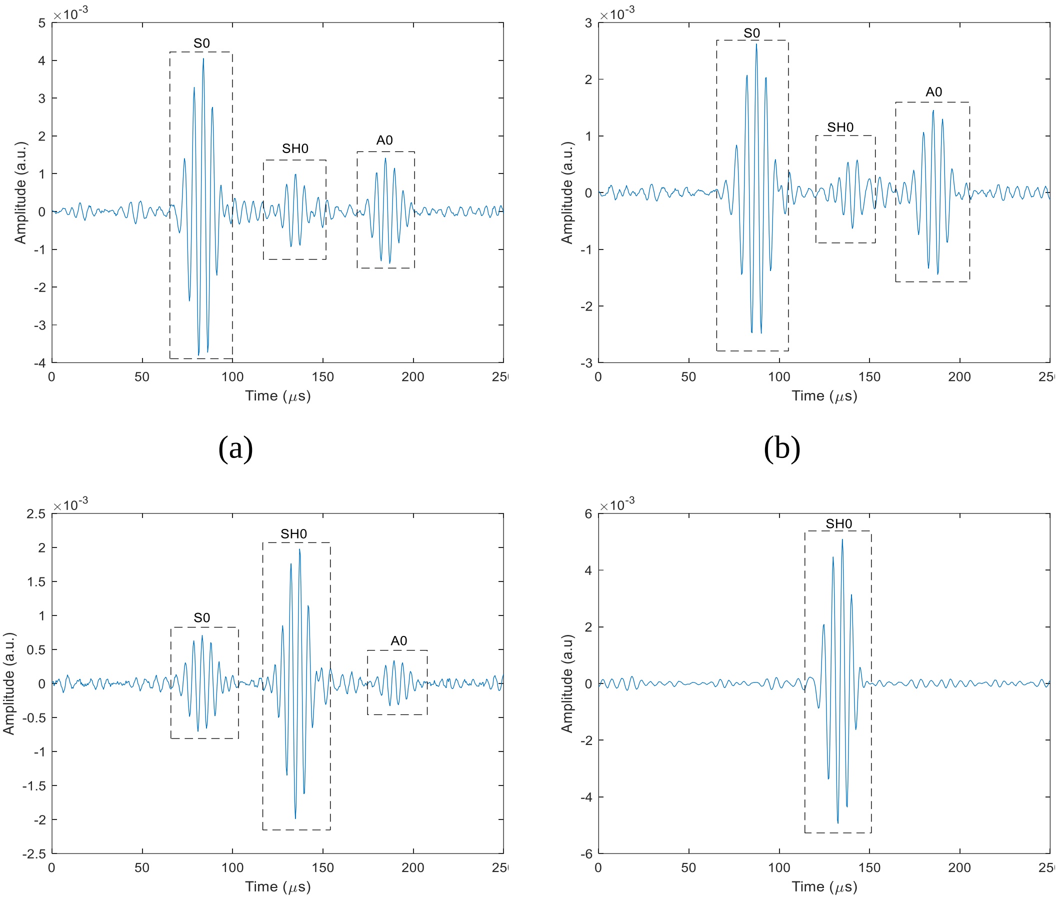

(a)

(b)

(c)

(d)

Figure 4.13. *Detected waveforms at 350mm distance for (a) Configuration 1 at 160°, (b) Configuration 2 at 90°, (c) Configuration 3 at 90° and (d) Configuration 4 at 0°.*

The signal wave magnitude |A| was measured at the fixed distance of 350 mm using the setup shown earlier in Figure 4.7 as a function of angle to obtain directivity plots. The radiation patterns for both the symmetrical S0 mode and the shear horizontal waves modes SH0 are illustrated in figure 4.14 for all four configurations. It can be seen from the figures that the radiation patterns are significantly different for each configuration.

The results for Configuration 1 show a complex directivity behaviour for both the S0 and the SH0 modes, with no clear unique directivity for a specific wave mode. However, multiple local directivities can be observed affecting defect detection in specific areas where there is minimal ultrasonic energy being generated.

Configuration 1 Configuration 2

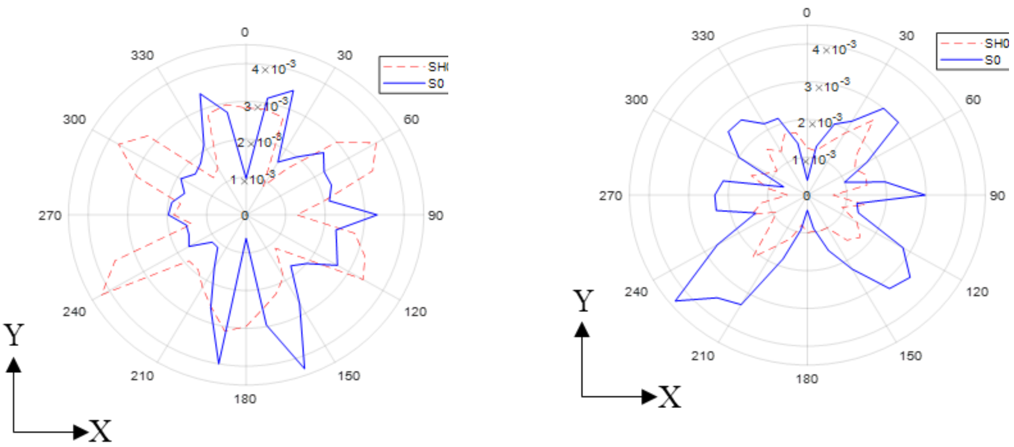

Configuration 3 Configuration 4

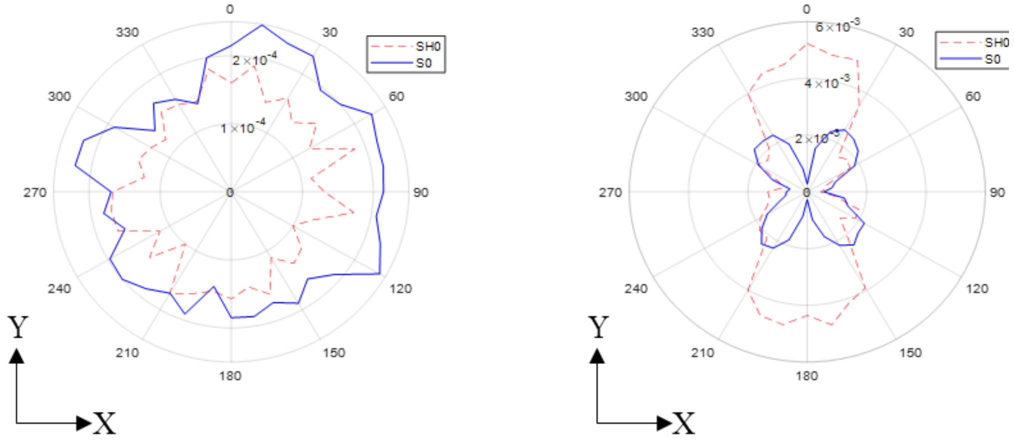

Figure 4.14. *Radiation patterns for the guided waves modes S0 and SH0*

The magnitude of both wave modes is similar. This is due to the complex vibration behaviour of the patch seen earlier when the patch response was captured. The complex behaviour was caused by magnetostrictive forces only - Lorentz forces were not expected to be generated. As only magnetostriction forces are generated, the dynamic magnetic field is oscillating and thus the magnetostrictive patch is subject to twisting forces. This behaviour led to a vibration mechanism similar to the Wiedemann effect generated in a plate favouring the generation of SH0 in the 0°-180° direction and S0 in the perpendicular direction.

In the case of Configuration 2, the directivity pattern of both S0 and SH0 modes remained complex with no clear unidirectionality for any specific wave mode. However, local directivities can be identified thus a proper selection of the excitation angle is required to maximise the ultrasonic energy. The magnitude of the S0 mode was higher than that of the SH0 mode, with multiple lobes at different angles. Lorentz forces within this configuration are expected to be cancelled due to opposing magnetisation forces.

For Configuration 3, it can be observed that both waves are radiating in a more uniform pattern, while the SH0 mode amplitude is significantly greater than that of the S0 mode. Such a directivity pattern is expected, as both the dynamic magnetic and static magnetic fields are in-plane, resulting in forces that are radial in the X-Y plane.

Finally, in Configuration 4, it can be seen that the SH0 mode was predominantly directed in the 0° and 180° directions, parallel to the Y-direction. This pattern was expected, as the static field B_s was applied in the X-direction, enhancing the generation of the SH0 in the Y-direction (and this agrees with the images in Figure 4.11). The S0 mode directivity pattern presented four main lobes, with maxima at 30°, 135°, 225° and 315°. The overall magnitude of the S0 mode is lower than the magnitude of the SH0 mode across the full radial scan.

Figure 4.15 gives the results for the A0 mode for the four configurations. For configuration 1, it can be seen that four main lobes were present at the angles 35°, 140°, 215° and 320°. Configuration 2 led to the strong lobes of the A0 mode at 90° and 270°. This is due to the forces generated by this configuration being along the X axis, with minimal forces at 0° and 180°.The A0 mode had significantly lower magnitudes compared to the S0 and SH0 modes observed in Configuration 3. In this case, both the Lorentz forces and the magnetostriction forces were generated in the in-plane direction.

A complex directivity pattern was observed for configuration 4. In fact, it can be seen that there were lobes at multiple angles. The overall magnitude of the A0 mode was significantly lower than that of the S0 and SH0 modes. The Lorentz forces potentially generated along the Z-axis in Configuration 4 did not have a major effect on the generation of the A0 mode as most of these forces are cancelled due to opposing magnetisation forces. Similar to configuration 1, the Wiedemann effect was strongly affecting the wave generation leading to a quasi-omnidirectional generation of SH0 waves. These findings suggest that in the case of magnetostrictive patches, the generated magnetostrictive forces along the surface of the film will be dominant in elastic wave generation compared to the Lorentz forces generated in the out-of-plane direction.

For the different configurations generating S0, SH0 and A0, some inconsistencies can be observed for the full radial pattern amplitude which led to some differences with regards to the symmetry following 0º-180º axis. This is mainly due to the fact that, although the scanner used was performing the scan automatically using a robotic arm, the handling of the EMAT and the magnetostrcitve patch was performed manually which led to minor experimental errors. These errors led to some non-symmetry in some configurations such as for A0 for S0 Lamb waves.

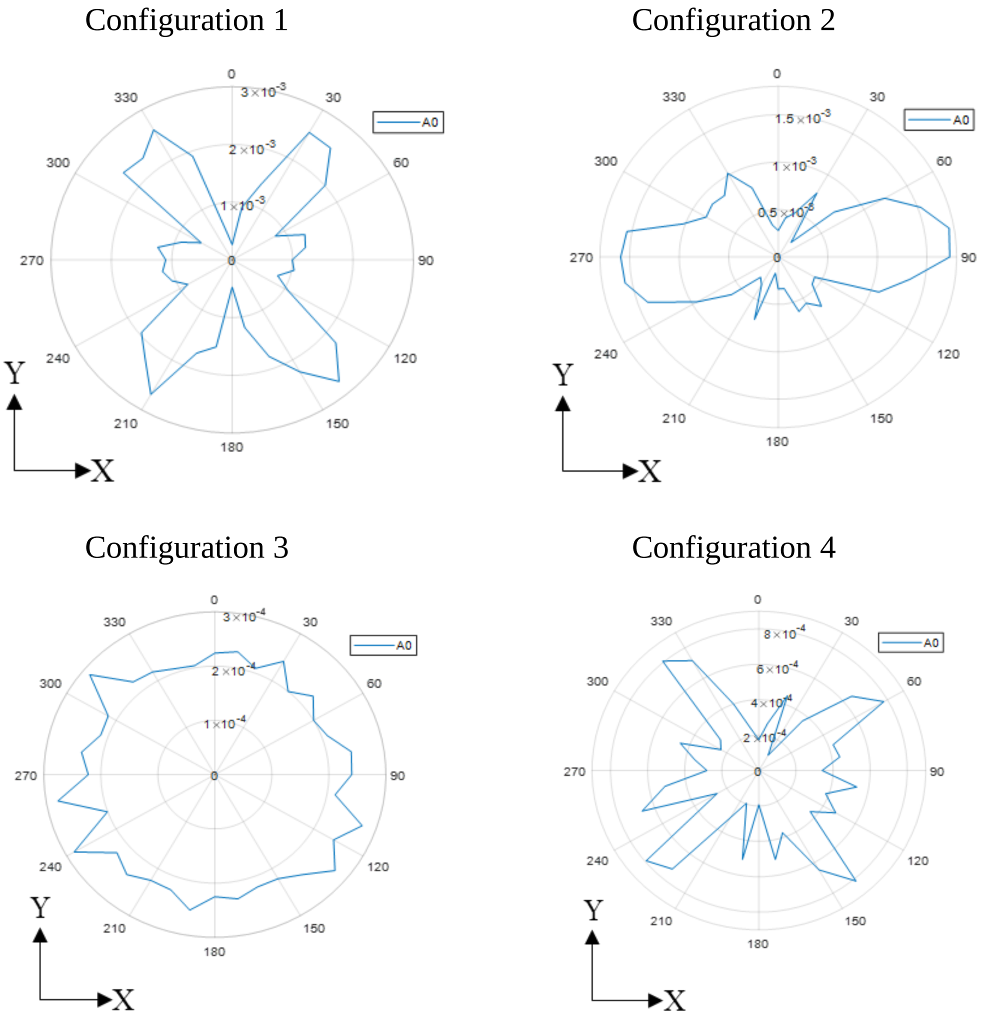
Configuration 1

Configuration 2

Configuration 3

Configuration 4

Figure 4.15. *Radiation patterns for the A0 guided wave mode*

4.3. Discussion

From the results reported, it can be concluded that complex interactions are taking place in the situation where a magnetostrictive patch is attached to a plate and subject to dynamic and static magnetic fields applied in different directions and configurations. In the case of Configuration 1, both the dynamic magnetic field B_d and the static magnetic field B_s are perpendicular; thus, only magnetostrictive forces will be observed as the Lorentz forces would not be generated. The wave pattern detected under the patch showed an asymmetrical distribution leading to a complex directivity for the generation of S0, SH0 and A0 modes. Configuration 1 showed that relying on the magnetostrictive forces only to generate the elastic waves will lead to a complex directivity pattern but with local maxima for different wave modes such as SH0 reaching up to 3×10^{-3} at 0º compared to a lower S0 wave amplitude equal to 1×10^{-3} at the same angle. S0 has a maximum of 3.3×10^{-3} while SH0 is equal to 1×10^{-3} at the same angle Configuration 2 indicated that the A0 mode amplitude was significantly lower compared to that of S0 and SH0 modes reaching around 2.2×10^{-4} for A0, but that prominent bipolar directivity lobes were present for the A0 mode in the same direction as the static magnetic and dynamic magnetic fields. This configuration can be used to optimise the generation of the A0 mode if needed.

In Configuration 3, the generated forces (magnetostrictive forces and Lorentz forces) were both located in the X-Y plane, parallel to the surface of the magnetostrictive patch. The directivity plots indicated that the radiation is fairly uniform for all three wave modes. This behaviour was expected, as the generation forces were radial and parallel to the surface of the patch.

The last configuration tested showed that the SH0 waves were favoured at specific angles of 0° and 180° reaching to levels of up to 5×10^{-3}. This is due to the fact that the static field B_s was directed towards the 90° direction, which enhanced the generation of shear waves. The SH0 mode directivity had minima at 90° and 270° as most forces are concentrated in those directions limiting shear vibration. In the case of A0 mode generation, the pattern is complex, but with clear maxima at the angles 55°, 140°, 230° and 320°.

4.4. Conclusions

The Polytec 3D Laser Doppler system was used to characterise different guided wave modes generated by attaching a magnetostrictive patch used to generate those elastic waves. The results showed a complex behaviour for the vibrations immediately under the patch, leading to complex directivity patterns for all three guided wave modes.

It has been proven that a specific guided wave mode can be preferentially selected and generated by manipulating the direction of the static and dynamic magnetic fields through the rotation of the field or by changing the direction of the applied magnetic field. In fact, the amplitude and the directivity of each of the elastic waves S0, A0 or SH0 can be controlled and modified in this way. These modifications were achieved by using different driving coils and external permanent magnets.

The data indicated an interaction between the magnetostrictive forces and the Lorentz forces generated in certain configurations, and that this interaction is complex. In practice, the different wave modes can be generated and their magnitudes controlled by using the same magnetostrictive patch, and simply modifying the direction of both the dynamic magnetic and static bias magnetic fields. This is important, as it allows the selection of different modes for guided wave NDE.

Prior knowledge of the anisotropy present in the directivity patterns is critical for all the guided waves modes as it can affect the inspection process and also the chosen wave generation mechanism if a specific mode is required. The origins of such anisotropy can be due to multiple factors such as the application of both the dynamic and static magnetic fields and their associated directions. As the patch was attached initially to a non-magnetic plate, it can be established that the waves were generated through either magnetostriction (generated within the patch) or Lorentz forces (generated within the patch and the plate) or a combination of both. In addition to that, the anisotropy could be affected by the vibrational performance of the patch. In the subsequent sections of the thesis, the patch will be attached to the composite plate which by its own introduces a level of structural anisotropy in addition to the magnetic anisotropy. This combination of anisotropies would affect the radiation patterns as structural anisotropy can affect the generation of the elastic waves in addition to the anisotropy induced magnetically.

Chapter 5: Theoretical investigation of the driving parameters controlling the magnetostriction effect

In the previous chapter, some of the main elements controlling the generation of vibrations within magnetostrictive patches were discussed. The magnitude and direction of the dynamic and static magnetic fields were varied, and the vibration patterns of the patch and radiation pattern analysis of the generated guided waves were investigated in an isotropic plate.

This chapter presents modelling predictions of the dynamic and static magnetic fields, together with a theoretical analysis of the generation of guided waves in isotropic plates and composite structures. First, the coil models were investigated to identify the generation patterns of the dynamic magnetic fields created by the coil. The coil lift-off effect is also investigated to identify the reduction in amplitude with distance from the patch. The combination of static and dynamic magnetic fields experimentally presented in the previous chapter is then discussed, together with the factors affecting guided wave generation. This approach helps in understanding the results of chapter 4, and the design of the experiments presented later in chapters 6 and 7.

5.1. Modelling using COMSOL software

COMSOL Multiphysics software [1] is a full package finite element modelling software that is widely used to understand the magnetostriction effect, the properties of dynamic coils and static magnetic field systems, and their associated transduction mechanisms [2-4]. The software is used to predict the dynamic magnetic field and the static magnetic field patterns in space. The findings are then used to design the experiments presented later in the thesis; and provided information on the interaction between the dynamic and static magnetic fields and a thin magnetostrictive patch.

The COMSOL software was used for modelling because it included multiple interconnecting modules, such as the AC/DC module, RF module and solid mechanics modules. These features allowed the modelling of the electromagnetic problem related to driving the magnetostriction effect through modelling the static magnetic field B_s and the dynamic magnetic field B_d.

Conventionally the coil generating the dynamic magnetic field and the permanent magnet generating the static magnetic field constitute the basics of an EMAT, as seen in chapter 2. In this research, a special focus is applied to the interaction of the magnetic fields toward the control of the magnetostriction effect. The study revolves around understanding the key parameters that can control the magnetostriction for the generation of ultrasonic guided waves. Both Lorentz forces and the magnetostrictive forces are considered in the theoretical study and experimental work. Through COMSOL, the AC/DC module was initially used to compute the direction and amplitude of the static magnetic field B_s, which was generated by C-shaped and cylindrical permanent magnets and an electromagnet. The electromagnet had an E-shaped ferrite core surrounded by 4 coils connected in parallel with 200 turns each. The coils of the electromagnet were connected to a DC pulsing unit. The modelling of the electromagnet is presented within this chapter while its associated experiments will be presented in the next chapter.

In addition, the dynamic magnetic field B_d generated by different coils shapes was studied. This allowed the interaction of the two with the magnetostrictive patch material to be predicted, and hence the features affecting guided wave generation.

The theoretical model was solved through the incorporation of both the potential scalar of the electric field (*V)* and the vector potential of the magnetic field (*A)*. These are defined as:

$$B = \nabla \text{ x A} \tag{5.1}$$

$$E = -\nabla V - \frac{\partial A}{\partial t} \tag{5.2}$$

where E and B are the electrical field and magnetic field respectively. In addition to solving the electromagnetic mathematical framework, COMSOL was used to theoretically identify the magnetostrictive curves for the materials used in the thesis.

Although magnetostriction is a non-linear phenomenon, the variation of magnetostriction levels in a ferromagnetic material with the applied magnetic field around a defined operating point of interest can be considered linear [5, 6]. Under this assumption, the coupling equations describing magnetostriction can be calculated using equations (5.3) – (5.6):

$$S = c_H \varepsilon - e_{HS}^T H \tag{5.3}$$

$$B = e_{HS} \varepsilon + \mu_0 \mu_{rS} H \tag{5.4}$$

$$\varepsilon = s_H S + d_{HT}^T H \tag{5.5}$$

$$B = d_{HT} S + \mu_0 \mu_{rT} H \tag{5.6}$$

where μ_0 is the permeability in a vacuum, S is the strain tensor, ε is the strain, and H and B are the magnetic field and the magnetic flux density respectively. In addition, d_{HT} and e_{HS} are the piezomagnetic matrices while the subscript T refers to the transpose matrix , and μ_{rS} and μ_{rT} are the relative permeability corresponding to a specific strain and stress respectively. Finally, c_H and S_H are the stiffness and compliance matrices respectively for a specific magnetic field value. Eqns. (5.3) and (5.4) describe the relations between the key variables constituting the magnetostriction modelling environment in the framework of stress magnetisation, while equations (5.5) and (5.6) describe the environment in the strain magnetisation framework.

As mentioned earlier, the linear magnetostriction framework can only be used when the problem is describing small changes of the variable around an operating point. In a more general context, the software solving engine is based on the equation (5.7):

$$\varepsilon = \frac{3}{2}\frac{1}{M_s^2}\left[\lambda_{100}(M \otimes M) + (\lambda_{111} - \lambda_{100})\sum_{i \neq j} M_i M_j (e_i \otimes e_j)\right] \tag{5.7}$$

where M is the magnetisation tensor, ε is the strain generated through the magnetostriction, $(M \otimes M)_{ij} = M_i M_j$ and e is the point strain calculated at the node level.

Following the solving of the electromagnetic equations system and coupling the electromagnetic forces to the strain generated through magnetostriction, the elastic waves propagation model included in COMSOL was used to simulate the resulting guided wave propagation in a plate. The software solver used the displacement equations system presented in chapter 1 to solve the propagation framework of the ultrasonic guided waves.

5.2. Static and dynamic magnetic fields modelling

5.2.1. Dynamic magnetic field modelling

In order to generate dynamic magnetic fields with different properties, both a racetrack coil and a circular coil were used, as described in Chapter 4. The coils were designed to provide different direction and amplitudes of the generated dynamic magnetic field (B_d). The initial design of both coils is presented in the figure 5.1.

Initially, a model of the racetrack coil and the circular coil was built into COMSOL to provide insights of the radiation patterns and the amplitude of the dynamic magnetic field generated by the coils. The coils used in the experiments were manufactured onto a PCB , with a FP4 substrate. The racetrack coil was made of 10 turns of 1 mm wide copper tracks with 0.5 mm spacing between adjacent tracks. The linear part of the racetrack coil is 34 mm long, as shown in Fig 5.1a. These dimensions were used in COMSOL, to ensure that the generated dynamic magnetic field is unidirectional under the linear section of the coil. The circular coil was made of 5 turns of 1 mm wide copper tracks, with 0.5 mm spacing between adjacent tracks. This coil was designed to provide a dynamic magnetic field which is radiating with the same amplitude in all directions. The coils presented in the figure 5.1. are used in building the theoretical model in COMSOL while the coils built and used during the experiments are formed from a continuous track spiralling outwards and included a feedthrough to connect the coil to the RF system.

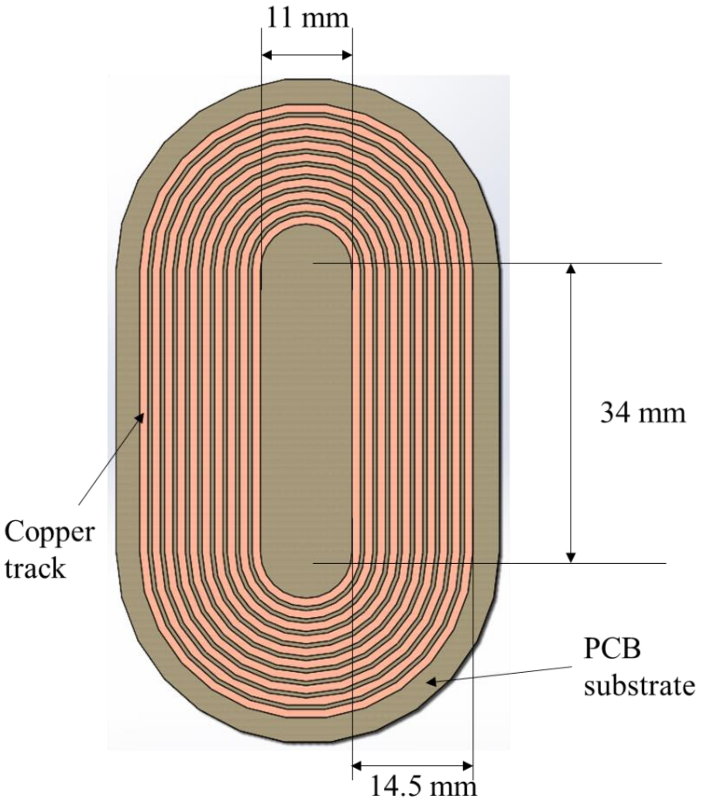

(a)

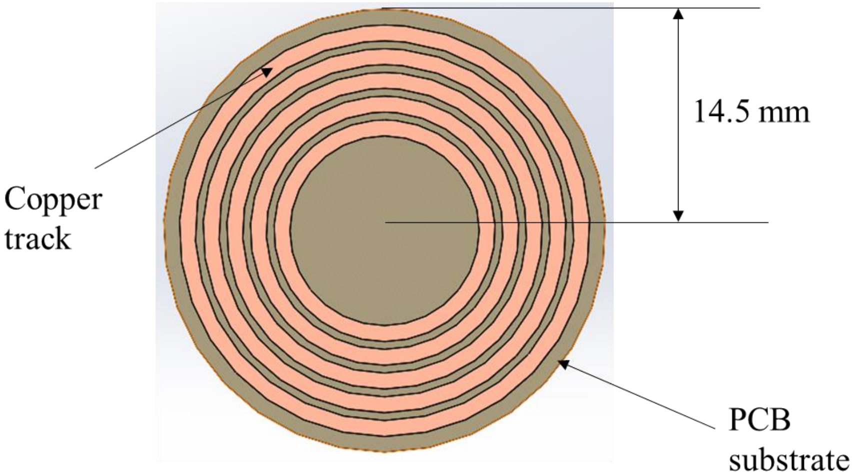

(b)

Figure 5.1. *COMSOL coil design and dimensions used to generate the dynamic magnetic fields showing (a) the racetrack coil and (b) the circular coil.*

The modelling results generated through COMSOL are presented in the figure 5.2. The figure presents the results of the modelling of the racetrack coil in the case where the magnetostrictive patch is placed under the coil. It helps in investigating the behaviour of the magnetic field generated initially by the coil before introducing the permanent magnet to result in a more complex behaviour. A similar approach was used for the circular coil. The patch was placed under the coil without the presence of the permanent magnet to identify the magnetic field patterns generated by the coils only in the first instance. Later, similar work was conducted by placing the magnetostrictive patch under the C-shape permanent magnet, the circular magnet and the electromagnet. Finally, the combination of the configurations is created by placing different coil shapes with different magnets, as was shown earlier in figure 4.4. The step-by-step modelling of the different elements helped to provide an understanding of how both the static and dynamic magnetic fields would interact in the presence of the magnetostrictive patch transducer.

As can be seen from figure 5.2(a), the magnetic flux density is generated with minimum variation in the region under the linear section of the racetrack coil. The RF pulsing system used in the experiments, to be described later in Chapters 6 and 7, can potentially deliver a power of 1.2 kW to the coil, under the correct electrical matching conditions. The modelling showed that the dynamic magnetic flux density that can be generated by the racetrack coil in the design used here can reach up to 0.16 T in the presence of the magnetostrictive patch as shown in figure 5.2. These readings were conducted to investigate the generation capabilities of the coil in the absence of the permanent magnet. The introduction of the static magnetic field will be described in detail in a later section. The magnetic flux density in the curved section of the racetrack coil exhibits a change of sign in the pattern, which is simply due to a rotation of the direction of the generated magnetic field. In fact, as seen from the figure 5.2(a), in order to analyse the region situated under the coil between the coil and the magnetostrictive patch, for the region where the magnetic flux density is positive, the dynamic magnetic field will be generated in the direction of +Y and when the magnetic flux density is negative, then the magnetic field is generated in the -Y direction. The input current induced in the coil is in the form of a windowed sine wave. Thus, under the same track, the dynamic magnetic field will be subject to change of sign when the current in the coil changes direction.

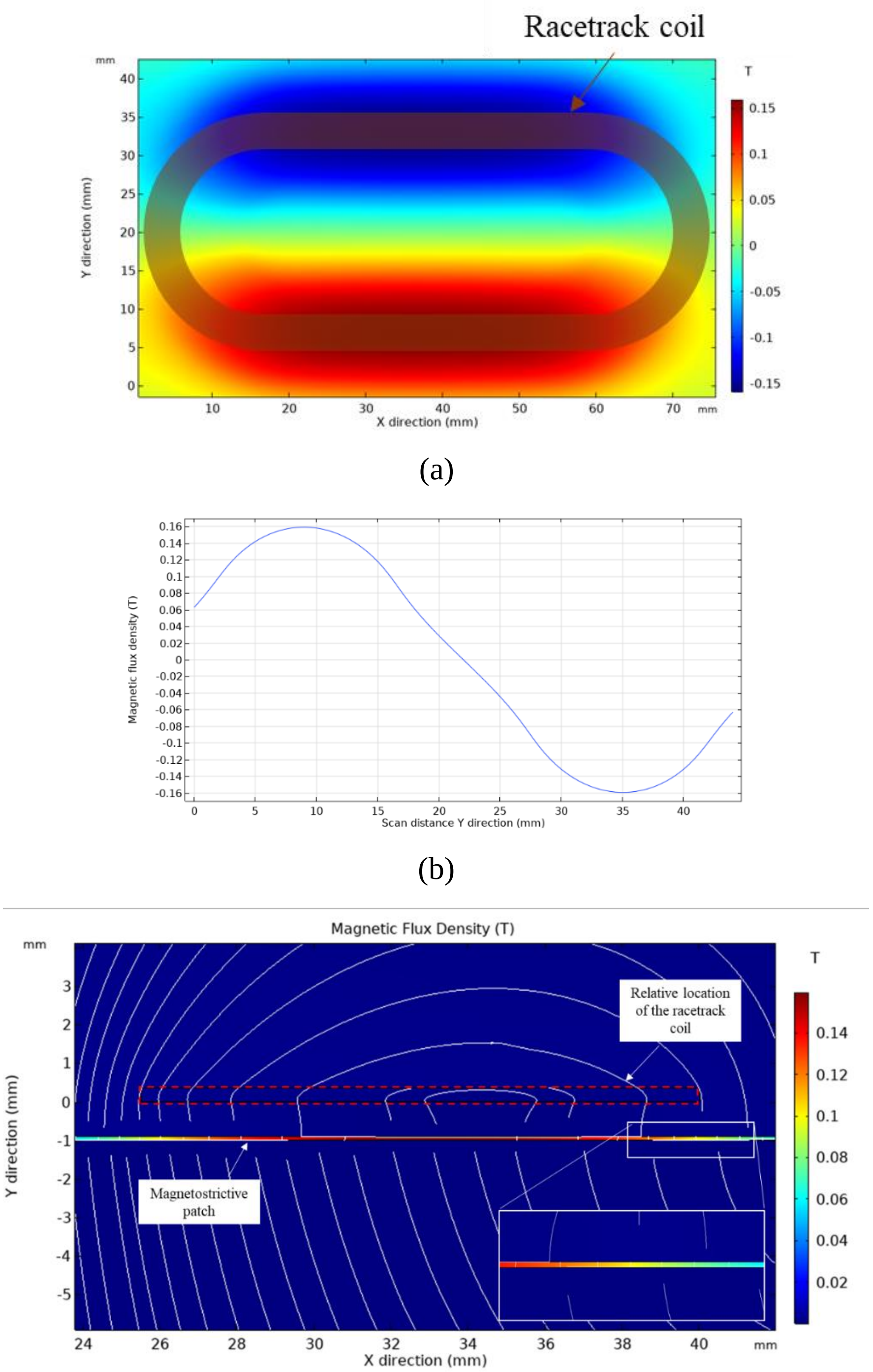

(a)

(b)

(c)

Figure 5.2. *COMSOL modelling results for the racetrack coil with the magnetostrictive patch showing the (a) magnetic flux density for the racetrack coil in Y direction (in-plane, perpendicular to the racetrack coil linear section), (b) the linear sweep of the magnetic flux density amplitude at the middle plane of the patch and (c) the magnetic flux density pattern around the linear sections of the racetrack coil with a zoom in for the area below the coil showing the concentration of the magnetic flux density within the patch.*

Figure 5.2(b) represents the magnetic flux density through a linear theoretical scan at the middle plan of the magnetostriction patch to understand the behaviour of the magnetic flux applied to the patch when using a racetrack coil, while figure 5.2(c) provides an insight into the flux density patterns in the region of interest under the linear section of the coil in the presence of the magnetostrictive patch. The sweep was performed along the full cross length of the coil. These measures were important as to understand the amplitude drop of the magnetic field generated by the coil due to any offset in placing the magnetostrictive patch. The lift-off distances were selected as the coil is expected to be at a close distance from the magnetostrictive patch. In the experiments, an isolating tape was used to protect the apparatus from short-circuits. The tape thickness is around 30 µm thick. as it can be seen from the figures, the magnetic flux density amplitude remains fairly constant in the linear region under the racetrack coil. In addition to that, the magnetic field is concentrated within the magnetostrictive patch due to the high permeability of the material which limits the magnetic losses in the area between the coil and the patch.

The second coil used to generate the dynamic magnetic field applied to the magnetostrictive patch is the circular coil to generate a radial dynamic magnetic field. The modelling results are summarized in figure 5.3. As can be seen from figure 5.3(a), the dynamic magnetic field is uniformly generated in the direction away from the coil centre when the input current is positive leading to a diverging pattern, while in the case when the current is negative, the pattern of the flux is converging toward the centre of the coil. Similar to the racetrack coil, the input power generated from the RF pulsing system led to the generation of a dynamic magnetic field with an amplitude equal to 0.1 T in the case where the coil is placed near the surface of the magnetostrictive patch while the magnetic field is concentrated within the patch section increasing the overall magnetic flux density.

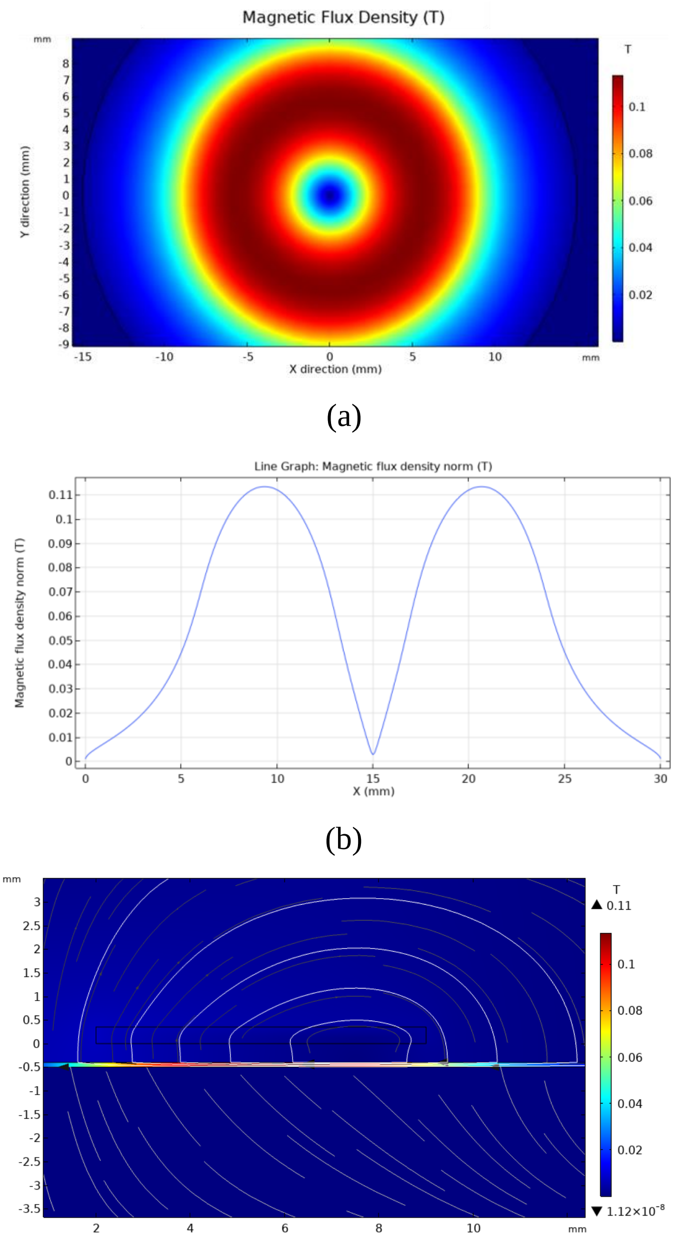

(a)

(b)

(c)

Figure 5.3. *COMSOL modelling results for the spiral coil showing the (a) magnetic flux density for the circular coil in the presence of the magnetostrictive patch, (b) the linear sweep of the magnetic flux density amplitude at the middle plane of the patch placed under the coil and (c) the magnetic flux density pattern under the circular coil showing the region of interest (coil – patch)*

5.2.2. Static magnetic field modelling

In addition to the coils used to generate the dynamic magnetic field, static magnetic fields were applied to the magnetostrictive patch in different directions and amplitudes, in order to control the magnetostriction levels within the ferromagnetic material. To generate the static magnetic field, three static (or pseudo static) magnets were used: a N42 NdFeB permanent magnet, an alnico permanent magnet and a pulsed electromagnet, throughout the work reported in this thesis.

Note that the modelling for both the circular magnet and the C-shape magnet was performed when the magnetostrictive patch was present to initially understand the effect of the patch on the generated magnetic fields.

To compute the magnetic flux density values and the patterns of the magnetic field, a model was built and analysed in COMSOL. Initially, the N42 permanent magnet as modelled and the results are presented in the figure 5.4. The permanent magnet is a cylindrical N42 rare-earth material magnet of 25 mm diameter and 10 mm height, and is able to provide magnetic fields of 0.35 T magnitude in the out-of-plane direction (i.e. normal to the surface of the patch (figure 5.4(b))). The magnetic behaviour under the magnet was also predicted when the magnetostrictive patch is present (figure 5.4(a)). It can be seen that the magnetic fields are concentrated within the patch and the overall direction of the field is altered from out-of-plane to in-plane within the patch

.

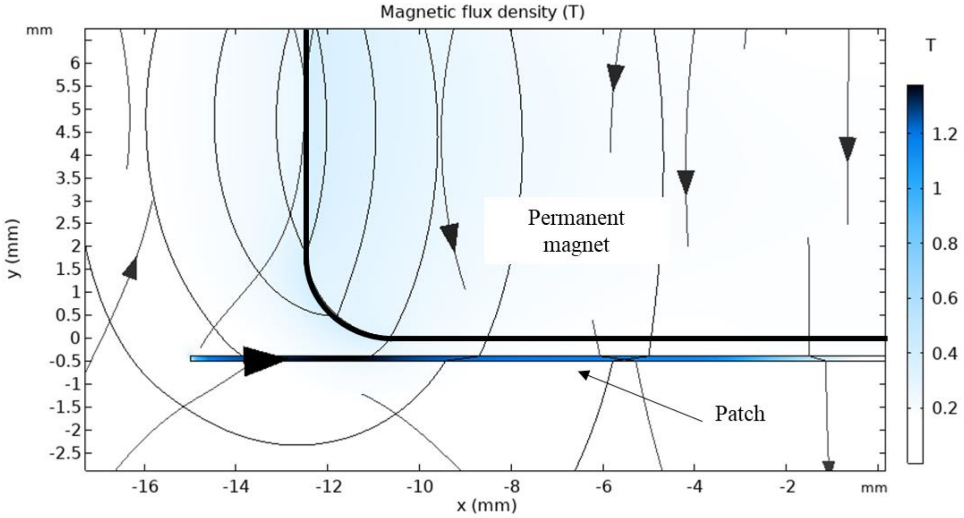

(a)

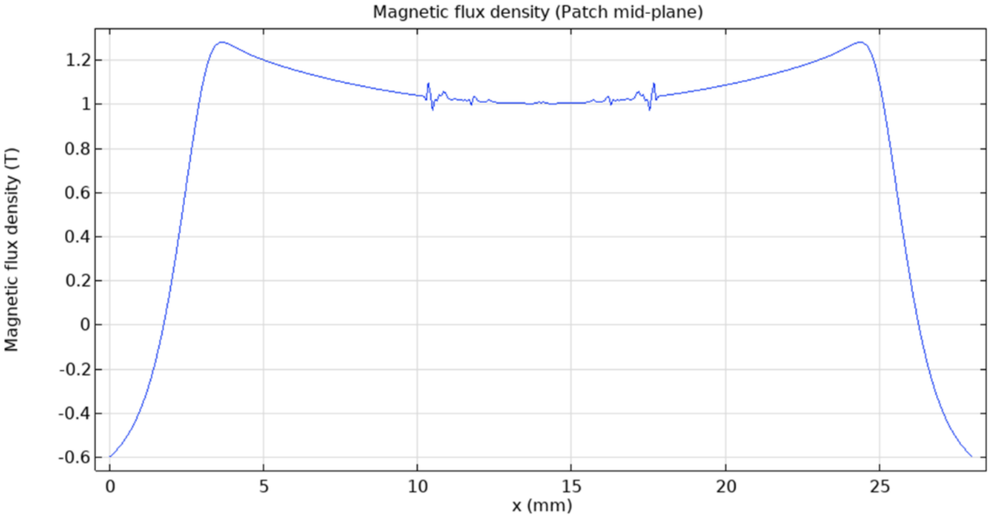

(b)

Figure 5.4. *COMSOL modelling results showing the (a) magnetic flux density map for the circular N42 permanent magnet (cylindrical coordinates r-Z), (b) a linear sweep in the radial direction of the magnetic flux density amplitude for different distances away from the magnet.*

The alnico grade 5 magnet was used to generate a static magnetic field in the in-plane direction, rather than in the out-of-plane direction. The modelling showed that the field generated between the magnet poles is relatively linear in the in-plane direction. The theoretical model also showed that the amplitude of the static magnetic field generated by the alnico magnet was in good agreement with the values measured experimentally using a commercial GM08 gaussmeter, which returned an amplitude of around 800 mT. The alnico magnet provided enough space to accommodate both the racetrack coil in one instance and the circular coil in another instance to combine and in-plane generated static magnetic field and dynamic magnetic field while offering the capability to set different direction for both fields.

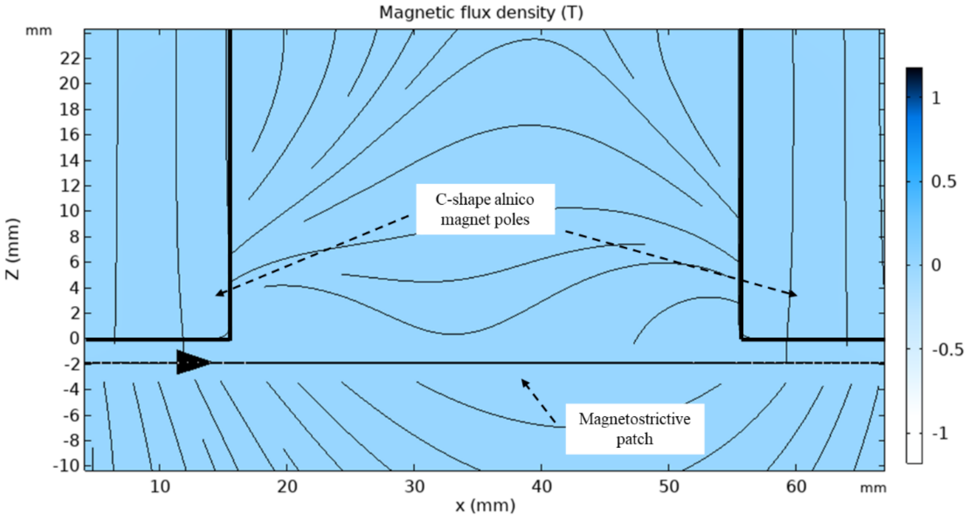

(a)

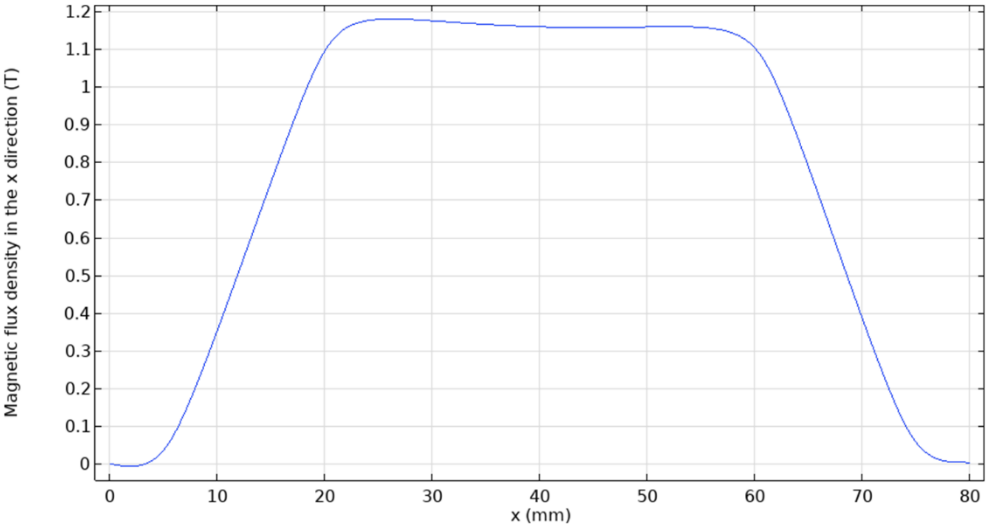

(b)

Figure 5.5. *COMSOL modelling results showing (a) the magnetic flux density for the C-shaped alnico 5 permanent magnet in X-Z plane, (b) the linear sweep of the magnetic flux density amplitude in the z direction in the mid-plane of the magnetostrictive patch showing the flux amplitude in the X direction (parallel to the surface of the patch)*

It is shown that the magnetic flux density has increased significantly due to the high permeability of the ferromagnetic material which led to the concentration of the magnetic field lines within the material increasing the flux density amplitude and direction.

Permanent magnets are able to generate relatively high amplitude static magnetic fields, but varying the field strength from them without changing the shape of the field is challenging. This type of capability was needed in the study of the interaction of dynamic and static fields, and so an electromagnet was used instead of permanent magnets to vary the amplitude and the direction of the generated magnetic field to better understand the mechanisms at work. These results are presented in Chapter 6. The electromagnet was designed as an E-shaped ferrite core with a coil surrounding the central pole of the core. The coil of the electromagnet was made of 4 segments of total of 200 turns of copper each connected in parallel to a DC pulsing unit. As can be seen in figure 5.6, the electromagnet provided the option of generating the static magnetic field in the out-of-plane direction when the patch is placed under the central pole while the static magnetic field could be generated in the in-plane direction when the patch was placed between the pole gaps of the electromagnet.

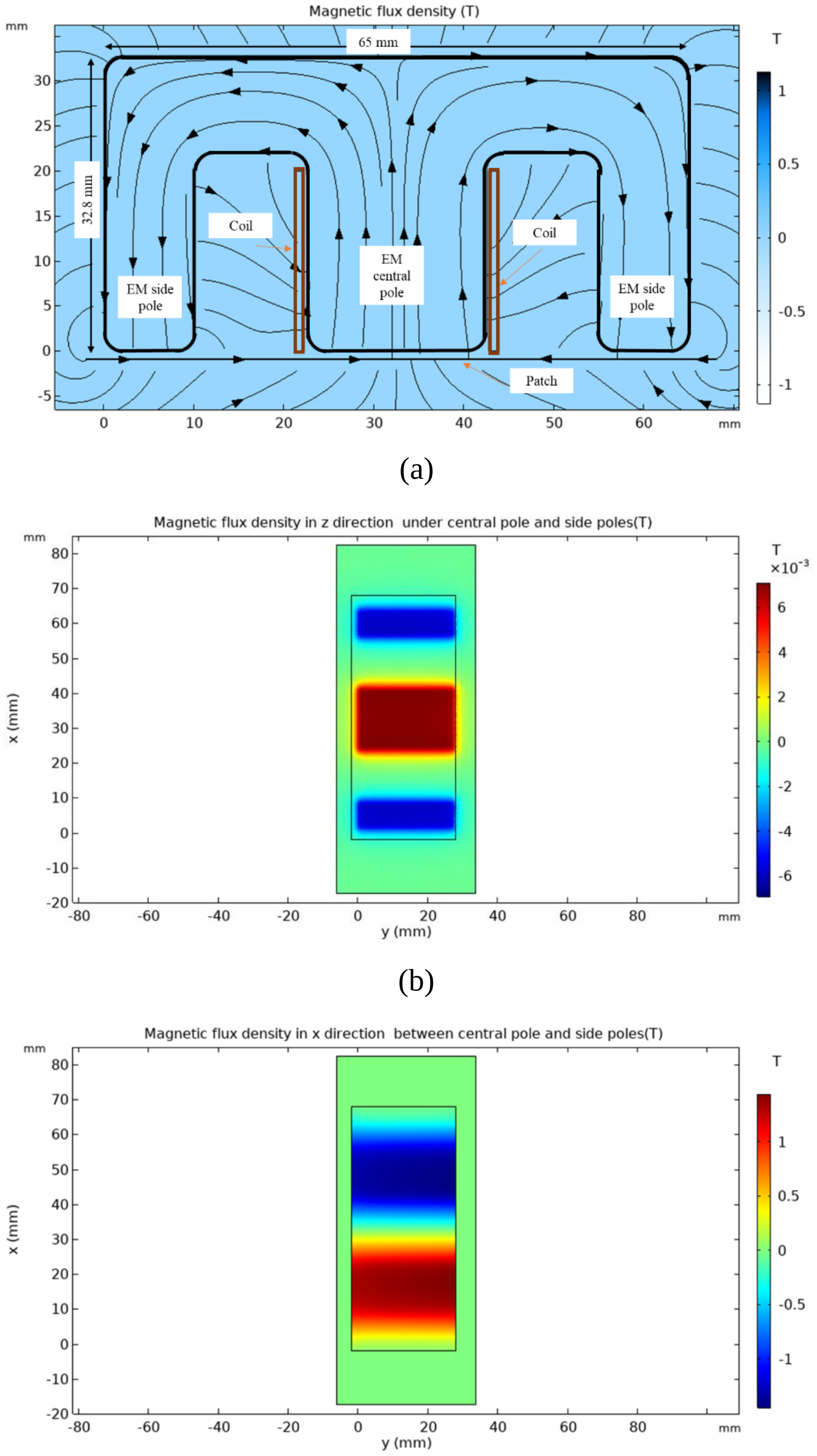

(a)

(b)

(c)

Figure 5.6. *COMSOL modelling results for the electromagnet to be used in Chapter 6, showing the (a) magnetic field behaviour generated through the electromagnet, (b) the magnetic flux density distribution under the central pole and (c) the magnetic flux density in the region between the poles.*

5.2.3. Theoretical investigation of Configurations 1-4 presented in Chapter 4

The four configurations detailed in Chapter 4 and presented in in figure 4.4. were designed to give certain properties in terms of expected response of the magnetostrictive patch. COMSOL was again used to study the situation where the coil is used to generate the dynamic field in the presence of the static field from a permanent magnet. This is now considered for all four configurations. In configuration 3, the circular coil with the cylindrical N42 permanent magnet was used. The circular coil ensured the generation of omnidirectional dynamic magnetic field in the direction parallel to the surface of the magnetostrictive patch. The static magnetic field led to the generation of an out-of-plane magnetic field. Configuration 4 was designed by using the circular coil and the alnico permanent magnet. This combination allowed the interaction between an omnidirectional dynamic magnetic field generated and unidirectional in-plane static magnetic field. The modelling results computed by COMSOL including the magnetostrictive patch are presented in the figures (5.7) – (5.10). The mechanical and magnetic properties of the magnetostrictive patch are summarised in the table below

Table. 5.1. *Magnetostrictive patch characteristics*

Patch material	Iron Cobalt Alloy
Shape	square
Dimensions	20mm x 20mm x 0.1 mm
Young’s Modulus	200 GPa
Poisson Ratio	0.29
Density	8.12 g/cm^3
Electrical Resistivity	0.42 μΩm
Permeability	18,000 N A^{-2}
Saturation Magnetostriction	70 ppm
Saturation Magnetisation	2.35 T

Configuration 1

Configuration 1 (Section 4.2.1, Figure 4.4(a))) had both static and dynamic magnetic fields orthogonal to each other with both in the same plane. This was achieved by using the racetrack coil and the alnico grade 5 permanent magnet. The dynamic magnetic field direction was perpendicular to the direction of the static magnetic field generated between the poles of the magnet. It can be seen from figure 5.5 that the alnico 5 permanent magnet is generating an in-plane magnetic field in the region between the poles. The magnetic field lines in the modelling are fairly straight in the region of the patch, and are directed from one pole to the other. When the coil is introduced, the magnetic flux lines and thus the field is disturbed leading to a modification of the magnetic field behaviour (figure 5.7(a)). It can be seen that the magnetic field in the area between the poles of the permanent magnet is no longer linear. The field is slightly rotated and a perpendicular component of the field vector is introduced which is parallel to the Y direction, and thus perpendicular to the direction of the generation of the in-plane static magnetic field. In addition, the new component is parallel to the dynamic magnetic field generated by the coil. It is expected that this introduction of the dynamic magnetic field would alter the behaviour of the magnetostriction through twisting motion enforcing the generation via the Wiedemann effect, as the resulting magnetic field generated by the combined system coil and permanent magnet has 2 perpendicular components. The interaction of the magnetic fields led to an oscillating dynamic magnetic field, introducing a partially rotating total field direction at any one point in time, in conjunction with an applied static magnetic field. The induced torsional behaviour of the dynamic field is expected to lead a shear vibration of the magnetostrictive patch. Similarly, the behaviour of both magnetic fields is expected to generate in-plane motion within the magnetostrictive patch enhancing the generation of the Lamb waves S0 mode and the shear horizontal mode.

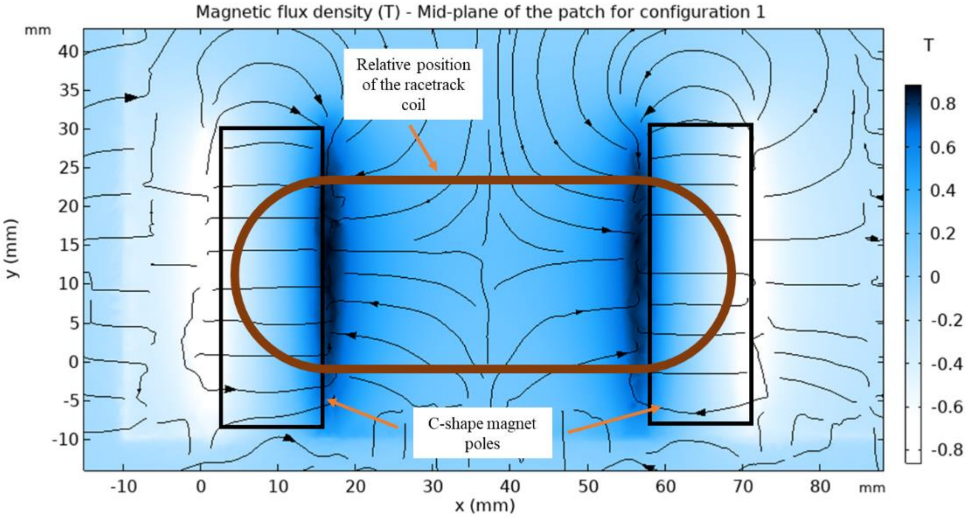

Figure 5.7. *COMSOL computed magnetic field density magnitude and patterns shown through the arrows at the level of mid-plane of the patch placed under the racetrack coil and the permanent magnet following configuration 1 design.*

Configuration 2

In configuration 2 (Section 4.2.1, Figure 4.4(b)), the racetrack coil was rotated so that both the static and dynamic magnetic fields are parallel and in-plane (i.e. parallel to the surface of the magnetostrictive patch). Similarly, the alnico magnet produces an in-plane static magnetic field. However, when the racetrack coil is introduced so that both, the field patterns are altered. As can be seen from figure 5.8, the magnetic field resulting from the interaction is elliptical in shape, with the major axis aligned with the magnetic fields generated by the coil and the permanent magnet. Such behaviour is expected to affect the generation of magnetostrictive forces, and this would cause a directional driving mechanism to the magnetostrictive patch. This effect was actually observed in Chapter 4, (see Figure 4.10(a)), where the effect of this directionality on vibrations generated within the patch was described.

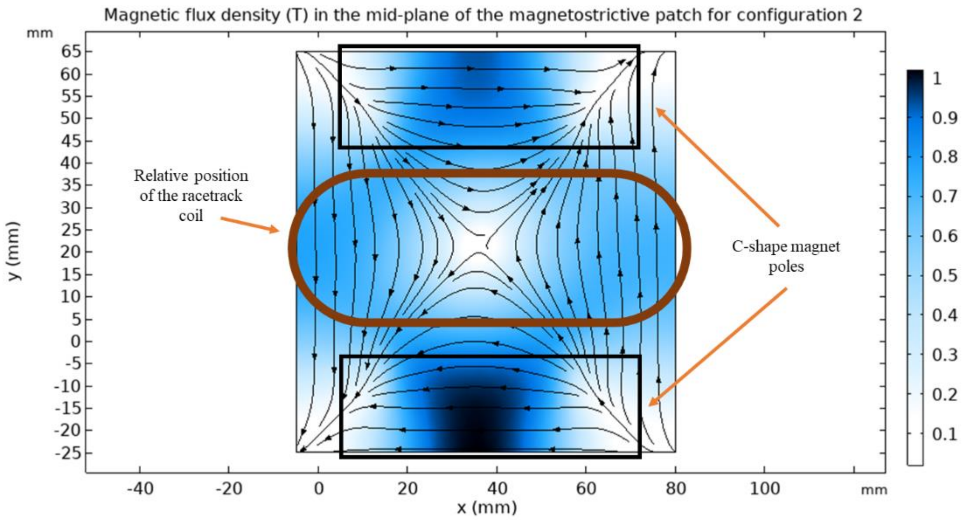

Figure 5.8. *COMSOL computed magnetic field density magnitude and patterns shown via the arrows at the level of mid-plane of the patch. This was placed under the racetrack coil and the permanent magnet following configuration 2 design.*

Configuration 3

Configuration 3 (Section 4.2.1, Figure 4.4(c)) contained an omnidirectional dynamic magnetic field generated by a circular coil, and an out-of-plane static magnetic field. A prediction of the resulting magnetic field is presented in figure 5.9. It can be seen that the magnetic field lines are propagating in a circular pattern and uniform across the 360º space. This distribution would allow the magnetic field to propagate in a diverging behaviour, moving symmetrically away from the centre of the circular coil. As the magnetostrictive patch was introduced and placed under the coil and the permanent magnet, the magnetic field lines are concentrated within the material due to its high permeability. These theoretical findings are in good agreement with the results presented in Chapter 4 (Figure 4.11(a)) where it was demonstrated that this configuration led to an omnidirectional wave generation. The interaction of the dynamic and static magnetic fields computed in COMSOL is omnidirectional which led to a generation of uniform vibration forces on the magnetostrictive patch in the radial direction.

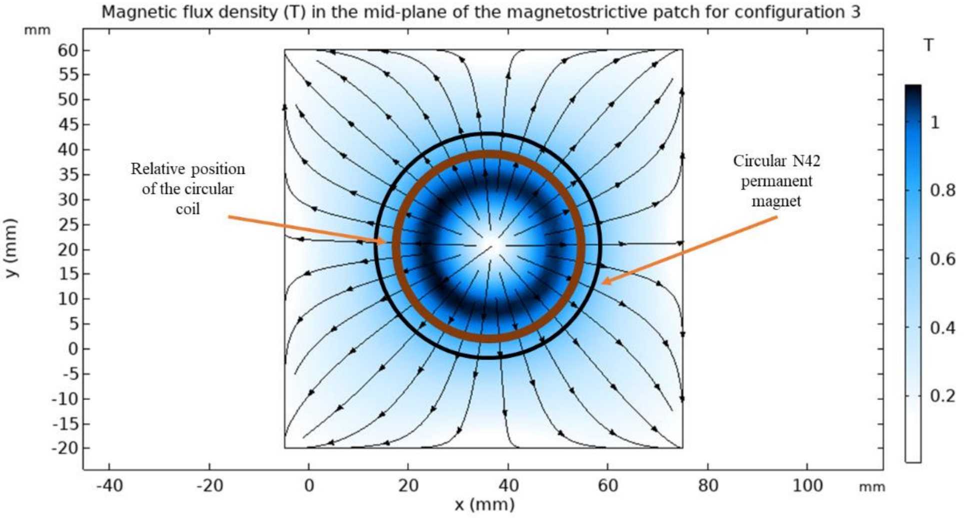

Figure 5.9 *COMSOL computed magnetic field density magnitude and patterns shown via the arrows at the level of mid-plane of the patch. This was placed under the racetrack coil and the permanent magnet following configuration 3 design.*

Configuration 4

Configuration 4 consisted of utilising the circular coil and the alnico permanent magnet. As seen from the figures 5.3 and 5.5, the coil will generate a radial dynamic magnetic field, while the permanent magnet will generate a linear in-plane static magnetic field. The predicted output is shown in figure 5.10. In agreement with the discussion in Chapter 4 (see Section 4.2.2 and Figure 4.13), this interaction is of complex behaviour. The magnetic field lines computed under the coil and the magnet surface presented two main features. The lines are diverging away at the centre of the magnet, leading to the assumption that the coil is altering the magnetic lines, while the flux regains a more linear pattern at the edges of the permanent magnet. The effect of such interaction on magnetostriction was investigated in Chapter 4. It is expected to predominantly generate in-plane magnetostrictive forces as Lorentz forces can be cancelled due to opposing magnetization forces thus the sum of forces would be focused in the radial direction (from the circular coil) and the linear pattern generated from the C-shaped permanent magnet.

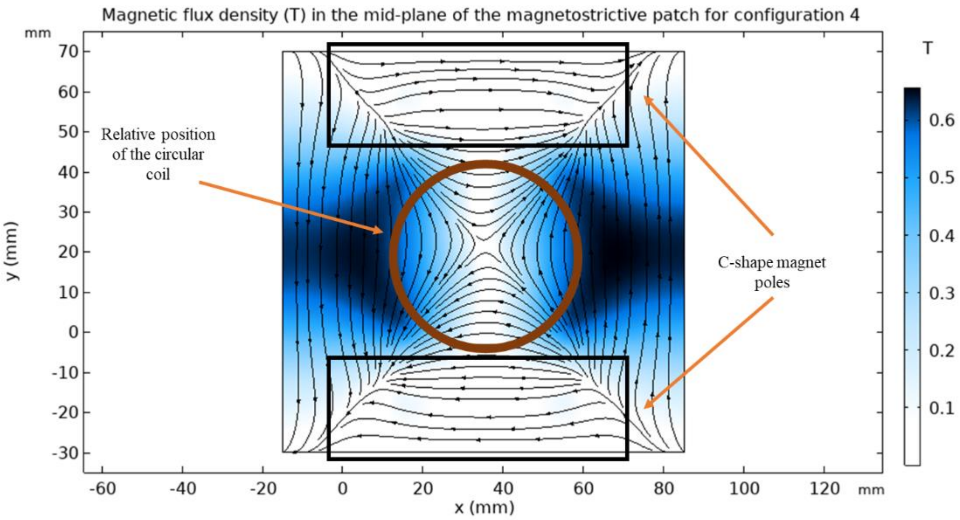

Figure 5.10. *COMSOL computed magnetic field density magnitude and patterns shown via the arrows at the level of mid-plane of the patch. This was placed under the racetrack coil and the permanent magnet following configuration 4 design.*

5.3. Theoretical analysis of the magnetostrictive patch transducers:

The magnetostrictive curve shown in figure 5.11 is that for VACOFLUX 48, which is a soft magnetic cobalt-iron alloy with relatively high magnetostriction levels at around 70 ppm. The magnetostrictive curve was computed using COMSOL. The curve is used to identify the operational region of the material, as the magnetostrictive force that generates the elastic waves is dependent of magnetic field amplitude and direction. In practice, the operating point at which such a material is designed to vibrate is selected to be within the linear region with the steepest slope. This is where larger levels of magnetostriction are generated, when the applied magnetic field is varied by a given amount. The VACOFLUX 48 material selected saturates at around 2.4 T, generating the highest level of magnetostriction equal to 70 ppm.

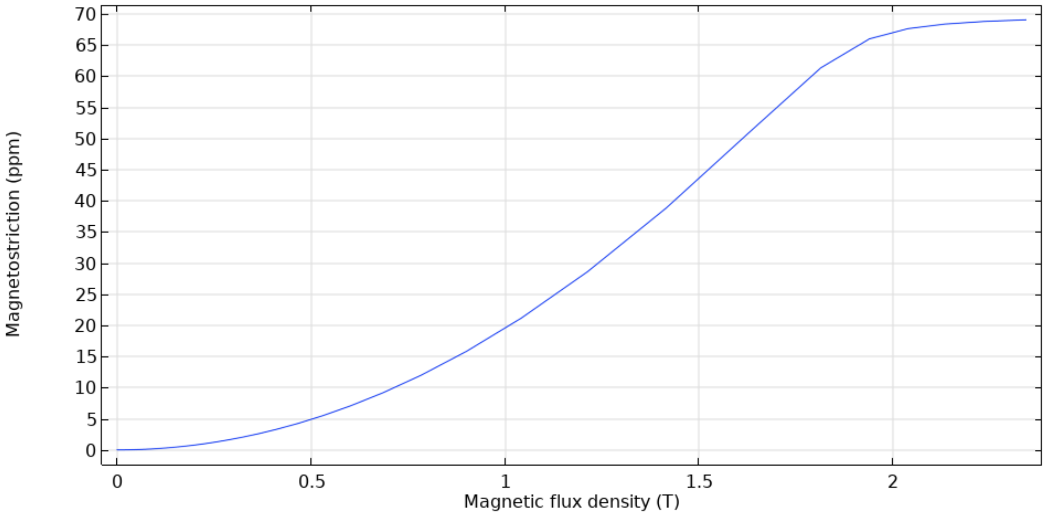

Figure 5.11. *Computed magnetostrictive curve for VACOFLUX 48 when the static magnetic field was applied in the in-plane direction*

The equipment used to generate the magnetic fields used in the current work are capable of generating magnetic fields with flux densities reaching 1.1 T. The operating range of the magnetic fields is below the saturation level and thus the gradient of the magnetostriction changes in function of the magnetic flux density is high resulting in higher strain levels generation when the magnetic field is varied by small increments. In addition to that, the material is expected to operate linearly when the magnetic field is varied.

5.4. Conclusions

In this chapter, COMSOL simulations of the different elements affecting the design of the experiments has been investigated. This modelling of the magnetic fields and their interaction was useful as it provides an insight into the patterns of the fields which are used to drive magnetostriction within the patches. Later, the magnetostrictive curve for the Vacoflux 48 was computed to identify the operational magnetic flux density range that should be selected. Good agreement of COMSOL modelling predictions with the findings of Chapter 4 has allowed the modelling to better understand the generation mechanisms at work, and to design practical arrangements for excitation of the magnetostrictive patches. The following Chapters will investigate the effect of the excitation frequency and the simultaneous variation of the magnitude and direction of the applied static magnetic fields and later the experimental behaviour in terms of guided wave generation and the creation of images of defects using these waves.

References for Chapter 5

[1] COMSOL. 2022. COMSOL: Multiphysics Software for Multiphysics Simulations. [online] Available at: <https://www.comsol.com/> [Accessed 10 February 2022].

[2] Zhang, Y., Sun, P., Gou, J., Liu, X., Yang, T., You, C. and Ma, T., 2021. Depth-dependent decomposition and property of large magnetostriction Fe-Ga alloys. Applied Surface Science, 569, p.151059.

[3] Ren, W., Xu, K., Dixon, S. and Zhang, C., 2019. A study of magnetostriction mechanism of EMAT on low-carbon steel at high temperature. NDT & E International, 101, pp.34-43.

[4] Ren, W., He, J., Dixon, S. and Xu, K., 2018. Enhancement of EMAT’s efficiency by using silicon steel laminations back-plate. Sensors and Actuators A: Physical, 274, pp.189-198.

[5] Kim, Y.Y.; Kwon, Y.E. Review of magnetostrictive patch transducers and applications in ultrasonic nondestructive testing of waveguides. Ultrasonics 2015, 62, 3–19.

[6] Gao, X.; Pei, Y.; Fang, D. Magnetomechanical behaviors of giant magnetostrictive materials. Acta Mech. Solida Sin. 2008, 21, 15–18.

Chapter 6: The Effect of Changes in Magnetic Field and Frequency on the Generation of Magnetostrictive Forces Within Thin Patches

In the previous chapters, experimental work focused on the study of the ultrasonic guided wave generation for different magnetic fields directions, while theoretical work focused on understanding the interaction of the magnetic fields for the different configurations reported within the thesis. In this chapter, a series of experiments were conducted to investigate the effect of varying different key parameters such as the frequency, direction and amplitude of the externally-applied magnetic fields. This is so that the vibrational characteristics of the magnetostrictive patches can be enhanced.

6.1. Preliminary analysis for the VACOFLUX 48 material

In order to fully understand the behaviour of the thin magnetostrictive patch when subject to different frequencies, multiple magnetostrictive materials were studied so that the most suitable material to the desired application could be selected. Initially, Terfenol-D ($Tb_{0.3}Dy_{0.7}Fe_{1.92}$) was chosen, as it is the material with the highest magnetostrictive level (up to 1200 ppm). However, it could not be produced as a thin film as the material is brittle, making it not suitable to NDT applications based on magnetostrictive thin patches. Another option considered was Metglass foils (iron-based alloy) which is produced as patches with high permeability. However, the saturation magnetostriction is around 30 ppm which significantly reduces the performance of the patch in terms of generating elastic waves. The third material that was investigated is the VACOFLUX 48 which can be produced as patches and providing a saturation magnetostriction around 70 ppm. Thus, VACOFLUX was selected.Although the saturation magnetostriction is lower than other commercially available materials, the combination of the material being produced as a thin patch providing fairly good level of magnetostriction offered flexibility and performance.

To analyse the effect of variation of amplitudes and directions of both the static and dynamic magnetic fields on the performance of the magnetostrictive patch, a preliminary analysis of the composition of the material was conducted. This analysis was performed to eliminate any inconsistencies in the design or manufacturing of the VACOFLUX 48 material, obtained from ®VACUUMSCHMELZE GmbH & Co., Hanau, Germany. It is an iron-cobalt (FE-Co) alloy containing small amounts of vanadium (V). The chemical composition of the magnetostrictive patch transducers was measured using a Scanning Electron Microscopy (SEM) with Energy Dispersive X-Ray (EDX) analysis. Manufacturing inconsistencies were investigated using this technique, with a spot size of 1.5 µm, which could be scanned over the surface. Figure 6.1 shows a typical SEM-EDX result at one position. The response from the analysis points is presented in figure 6.1, which includes the chemical elements reported in the commercial datasheet from the manufacturer.

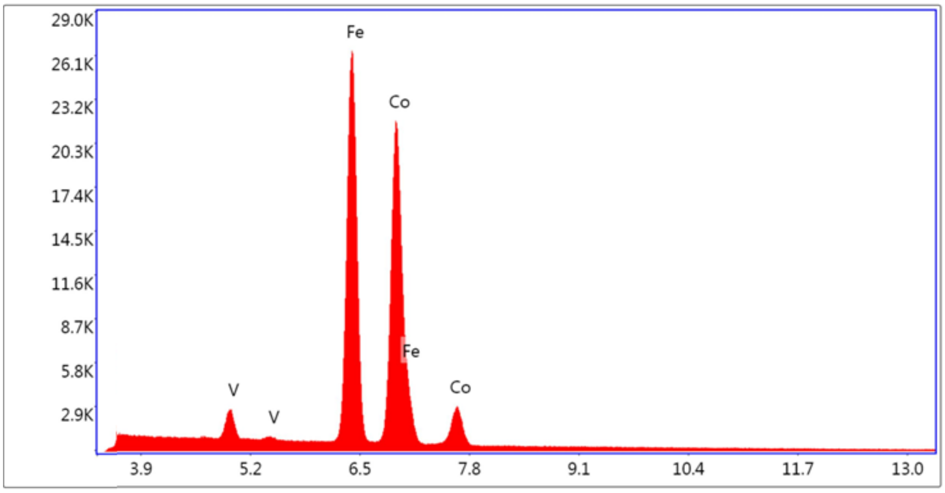

Figure 6.1. *Count numbers and energy levels of the structure analysis for the VACOFLUX 48 showing high levels of iron and cobalt obtained through the SEM EDX Analysis*

The response from different analysis points is summarised in Table 6.1, which includes the values reported in the commercial datasheet from the manufacturer. It can be seen that, although there was some analysis numerical readings variations, the results indicated a fairly uniform distribution of iron and cobalt across the patch.

Table.6.1. *Weight results for the VACOFLUX 48 magnetostrictive material showing percentages of the iron, cobalt and vanadium forming the alloy*

Element	Average weight (measured with SEM) % with measurement error values	Weight (Commercial datasheet) %
Iron (Fe)	48.05 ± 1.74	49
Cobalt (Co)	46.79 ± 1.73	49
Vanadium (V)	2.25 ± 3.79	2

In addition, the magnetic B-H curve of the material was obtained from the manufacturer datasheet and is presented in the figure 6.2. The ferromagnetic VACOFLUX material exhibits high permeability and high saturation flux density levels, with a high level of magnetostriction value (70 ppm). The dimensions and some other properties of the material were previously reported in table 5.1.

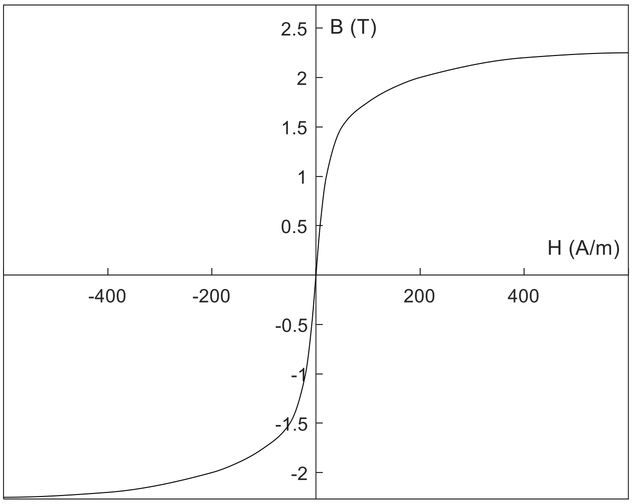

Figure 6. 2. *The BH curve for the ferromagnetic material used in the experiments: VACOFLUX 48*

6.2. Pulsed Electromagnet and RF coil Designs

The experiments were designed to investigate the effect of the variation of input parameters such as the frequency of oscillation of the dynamic magnetic field, and the amplitude and the direction of both the static magnetic field and the dynamic magnetic field. A pulsed electromagnet was employed to generate a high amplitude magnetic field that was at a constant level for a period of time during which the dynamic magnetic field was produced, with the dynamic magnetic field generated using a coil.

In order to expand the capabilities of the pulsed electromagnet, it was decided to use an E-shape ferrite core. These cores are widely-used in many applications such as continuous electromagnets and transformers, as they exhibit high permeability. This enhances the generation of high magnetic flux densities, while minimising magnetic losses. The hysteresis loop of the ferrite core is shown in Figure 6.3. This was needed as input to the FE model generated within COMSOL to predict the magnetic field properties generated by the electromagnet.

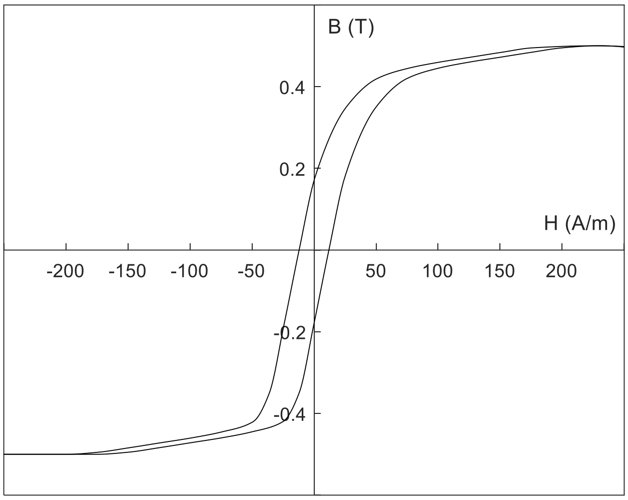

Figure. 6.3. *Hysteresis loop of the ferrite core used within the pulsed electromagnet*

The pulsed electromagnet was formed from an E-shaped ferrite core which is 65 mm long, 27.4 mm wide and 32.8 mm high, as shown in Figures 6.4. (a) and (b). The E-shaped pulsed electromagnet allowed the use of two different locations under the core itself. Under the central pole, the static magnetic field generated from the electromagnet will be in the perpendicular direction to the patch surface as proved through modelling reported in chapter 5, while in the case under the pole gap, the static magnetic field generated by the pulsed electromagnet will be parallel to the patch surface. The area of the central pole was 548 mm^2 and the area of the pole gap was 331.54 mm^2. COMSOL was used to predict the direction and amplitude of the static magnetic field in both locations, and the results are presented in figure 5.6.

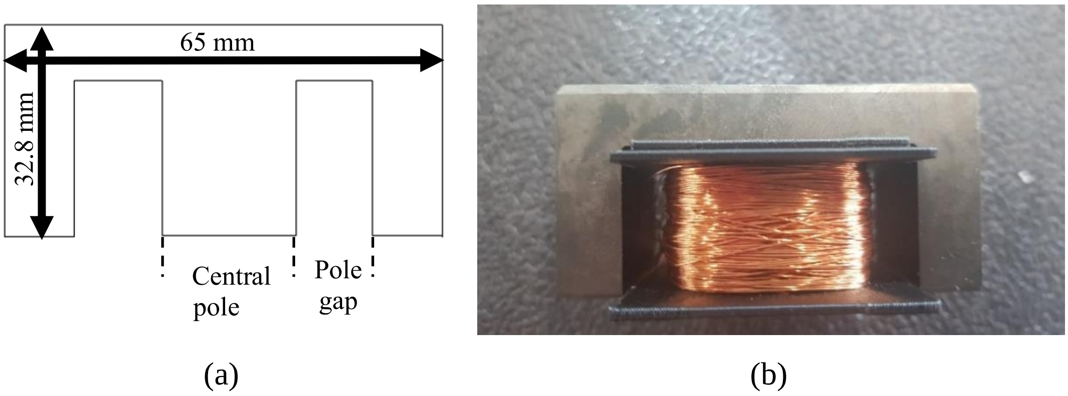

Figure 6.4. *(a) Ferrite core design and dimensions used for the electromagnet; (b) Image of the electromagnet and the coil winding.*

In order to generate the pulsed static magnetic field, a coil formed of 4 segments each with 200 turns connected in parallel was used surrounding the central pole to generate a magnetic field, with the capability to reach a magnetic flux density equal or exceeding 1 T. The COMSOL model, presented in chapter 5, indicated that a current of 25 A would be needed to achieve the 1 T threshold. The modelling also investigated the effect of the presence of the patch on the magnetic flux density variation. The magnetostrictive patch has a high magnetic permeability thus the magnetic field will be concentrated within the patch, increasing the overall magnetic flux density.

While the static magnetic field was generated using a pulsed electromagnet, the externally applied dynamic magnetic field (B_d) was generated using a printed circuit board (PCB) copper coil with a racetrack design used in the experiment in chapter 4. The width of each track was 1 mm with a spacing of 0.5 mm (see figures 4.3(a) and 5.1(a)). The COMSOL model reported in chapter 5 was built to investigate and analyse the resultant dynamic magnetic field, helping to optimise the direction of the dynamic magnetic field and providing insights into the best size and location of the magnetostrictive patch. The model predictions for the racetrack coil are shown in figure 5.2(a). This indicated that the patch should be placed under the straight section of the racetrack coil to ensure that the applied dynamic magnetic field is always applied in the direction parallel to the surface of the patch.

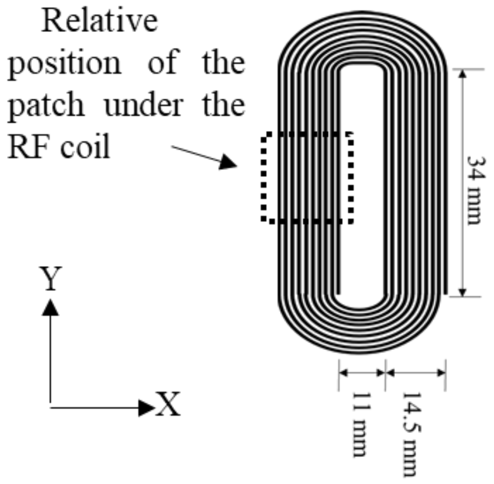

Figure 6.5. *The dimensions of the coil used to generate the dynamic magnetic field and the relative position of the magnetostrictive patch under the linear section of the coil*

6.3. Experimental Apparatus

To investigate the effect of input parameters on the magnetostriction within the VACOFLUX patch, an INNERSPEC custom-designed pulsing unit was used to excite both the pulsed electromagnet and coil. A schematic diagram for the overall apparatus is shown in Figure 6.6(a). The apparatus contained two interconnecting subsystems. The first was an RF pulsing unit that input current into the PCB coil in the form of a 5-cycle windowed pulse with a varying input frequency ranging from 100 kHz to 250 kHz. The coil was connected to the high-power pulsing unit within the INNERSPEC system, which was able to provide two levels of power, namely 450 W and 1.8 kW. The second subsystem was used to generate a pulsed quasi-static magnetic field of sufficient duration for the experiments. An initial experimental measurement using a gaussmeter confirmed the predictions of the COMSOL model, with the measured amplitudes of quasi-static externally applied magnetic field ranging from 0 - 0.5 T under the central pole, and 0 - 1.1 T between the poles. The gaussmeter experimental measurement indicated a magnetic flux density value of around 1 T when the DC excitation current reached its maximum. These findings are in good agreement with the results obtained through theoretical modelling in COMSOL which indicated that the electromagnet reaches its maximum value of around 1.1 T in-between poles when the magnetic field is generated in the in-plane direction. Similarly, the sensor measured around 0.35 T experimentally, which is within a good accordance to the theoretical results obtained by COMSOL.

The output of both subsystems is shown in Figure 6.5(b). The time delay of the tone burst used for the dynamic field generation could be adjusted so that it coincided with the time range during which the pulsed electromagnet was generating a constant value.

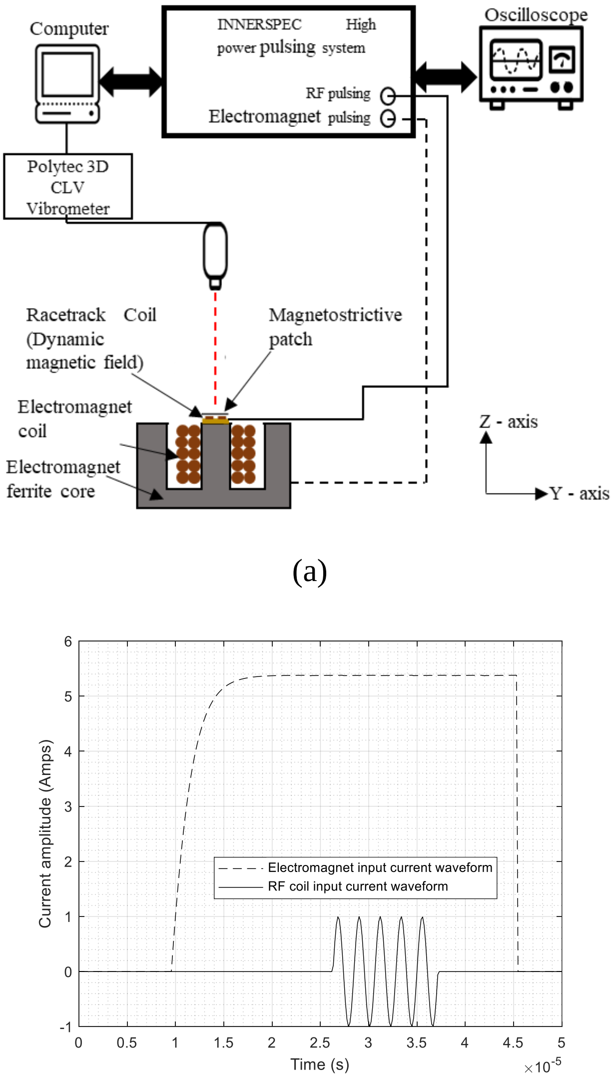

(a)

(b)

Figure 6.6. *(a) Schematic diagram of the apparatus. (b) The nominal output from the dual electromagnet/racetrack coil driving system, showing both the electromagnet drive current and the 5-cycle tone-burst used to excite the racetrack coil. Note that the RF coil was excited once the current to the electromagnet had stabilised.*

As in Chapter 4, the dynamic vibration and displacement of the magnetostrictive thin patch was detected using a Polytec CLV 3000 3D. The laser vibrometer was formed of three laser heads combined in a singular chamber. This provided the ability to scan the patch vibrations in both the in-plane direction (parallel to the surface) and in the out-of-plane direction (perpendicular to the surface of the square patch) in the three axes (X, Y and Z). Figure 6.7. shows the relative positions of the RF racetrack coil, the ferrite core and the ferromagnetic square patch for changing the direction of the static field $B_{s.}$ As before, the vibrometer provided the particle velocity waveform at each scanned point.

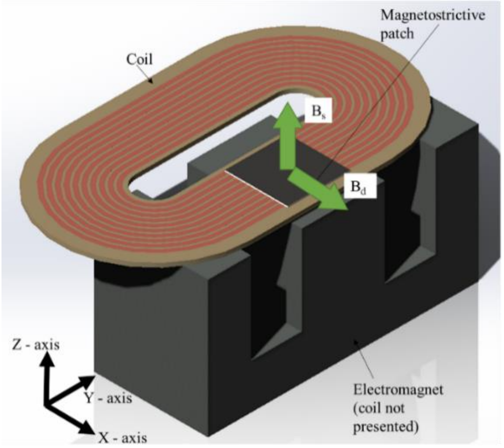

(a)

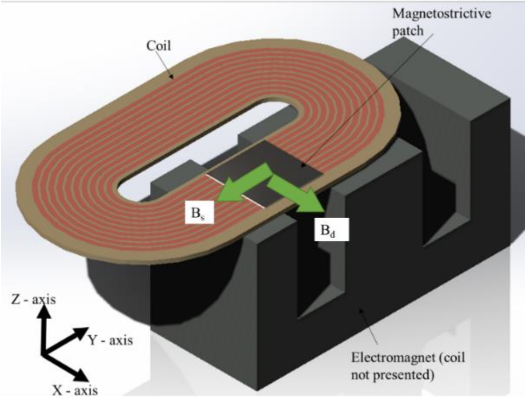

(b)

Figure 6.7. *Schematic diagram of the relative positions of the ferrite core, the coil and the magnetostrictive patch, (a) in the case the patch is placed under the central pole of the electromagnet and (b) in the case the patch is placed in the pole gap of the electromagnet.*

6.4. Results

6.4.1. Static magnetic field (B_s) in the out-of-plane direction

The first set of experiments was conducted so that the static magnetic field B_s was in the Z direction i.e. the out-of-plane direction perpendicular to the surface of the patch. The dynamic magnetic field B_d was generated parallel to the surface of the magnetostrictive patch. It was applied in the in-plane direction (the X-direction as shown in the figure 6.7).

The amplitude of the static magnetic field B_s and the excitation frequency f of the dynamic field were modified and the particle velocity signal on the surface of the patch was then captured in the three orthogonal directions (X, Y and Z) using the laser vibrometer system. This was placed in a way such that the laser beam was at the centre of the square patch. This configuration was selected in order to avoid any boundary effect while ensuring that the magnetic field was maintained with minimal variation around the laser region. The amplitude of the dynamic magnetic field remained constant for this first set of experiments as provided by the pulsing system. The excitation frequency was varied from 100 kHz to 240 kHz in 10 kHz steps. The amplitude of the static magnetic field B_s was varied from 0.1 T up to 0.5 T with a 0.05 T step.

Figures 6.9(a)-(c) show the results recorded from the laser system for the configuration shown in Figure 6.6 (a), with the patch located under the central pole region. Figures 6.9(a)-(c) show the particle velocity detected on the surface of the ferromagnetic patch in the three directions X, Y and Z, while Figure 6.9(d) represents the amplitude of the magnitude of the velocity which was calculated using the same equation as in chapter 4, Eq.4.1.:

$$|A| = \sqrt{A_X^2 + A_Y^2 + A_Z^2} \qquad (6.1)$$

where A_x, A_y, and A_z are the amplitudes of particles velocities measured on the surface of the thin patch in the directions X, Y, and Z respectively.

Figure 6.9(a) shows that, when the excitation frequency is being changed from 100 kHz to 240 kHz, there is a sudden decrease in the vibration amplitude in the X direction around 180 kHz. The vibrations in the Z direction, shown in the figure 6.9(c), decreased abruptly at ~ 200 kHz. In this case, the maximum value of vibrations was observed when the amplitude of the static magnetic field is above 0.4 T and when the excitation frequency ranged from 140 kHz to 180 kHz. In terms of excitation frequency, the vibrations in the Y direction are exhibiting similar behaviour to the vibrations in the Z direction with a maximum amplitude recorded in the frequency range of 140 kHz to 200 kHz. Note that this trend is limited to high amplitude values of B_s.

Figure 6.9(d) represents the overall magnitude of the vibrations in all directions. It was demonstrated that the most effective frequencies at which the patch is exhibiting high particle velocities are when the frequency ranges from 120 kHz to 180 kHz. High vibrational amplitudes could also be obtained by selecting a low frequency with a low static magnetic field. It should be noted that both Lorentz and magnetostrictive forces were generated due to this configuration. The Lorentz forces were generated in the X direction. It can be concluded that for this configuration, the magnetostrictive and Lorentz forces are constructively interfering because the amplitude recorded in the X direction was higher than that in the Y and Z directions.

The particle velocities in the X direction are higher than those generated in the Y direction and the frequency range is wider for the X direction. This is due to the fact that the dynamic magnetic field is applied in the X direction. The static magnetic field is applied in the out-of-plane direction and thus the field effect is expected to be uniform across the magnetostrictive patch.

Another observation is that the vibrations recorded are higher in the direction of the applied dynamic magnetic field B_d.

Initial modelling of the patch vibration natural frequencies for this particular geometry showed that a vibrational mode of the thin magnetostrictive patch shape would exist at 100 kHz as shown in the figure 6.8.:

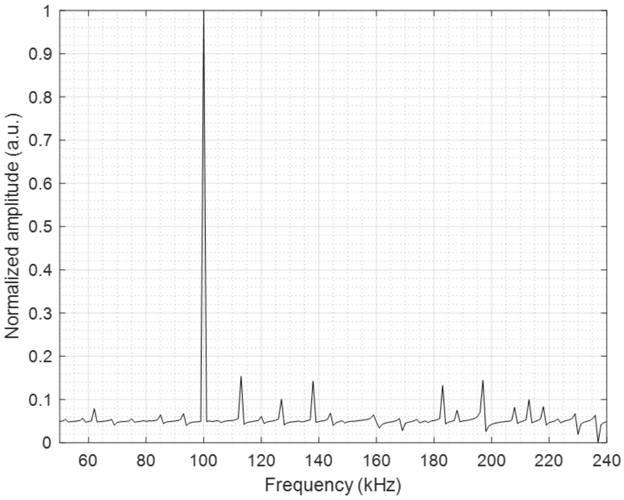

Figure 6.8. *Frequency analysis of the vibrational response of the magnetostrictive patch when attached to the plate showing high response at 100 kHz*

This modelling is in agreement with the experimental results, in that the particle velocity in all directions was high at 100 kHz, and changing B_s at that frequency had little effect, suggesting that the natural frequency of resonance was dominant. The frequency response showing the natural frequencies is valid for the patch within this configuration (attached to the structure). In fact, the vibrational patterns can be altered when attached to a different structure or the dimensions of the patch are changed as the natural frequencies will then be shifted to new frequencies [1].

At higher frequencies, a more complex interaction occurred, with amplitudes increasing with B_s as might be expected. There was a noticeable drop-off in amplitude at frequencies above 200 kHz, indicating that the material was not responding efficiently at these higher frequencies.

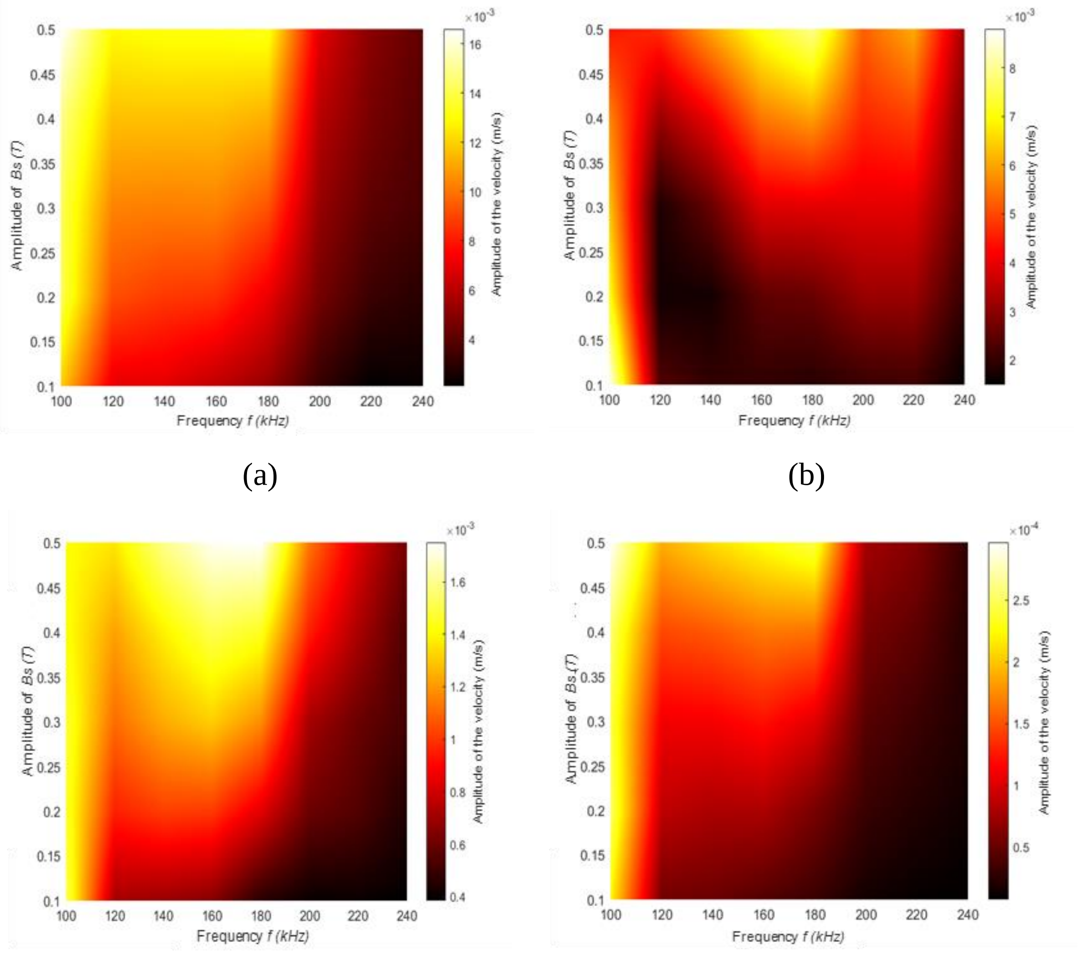

(a) (b)

(c) (d)

Figure 6.9. *Particle velocity amplitude mapping while varying the static magnetic field amplitude (B_s) and the frequency of the coil excitation in (a) the X direction, (b) the Y direction, and (c) the Z direction. (d) The resultant magnitude was calculated using Eqn. (6). B_s is in the out-of-plane direction.*

6.4.2. B_s and B_d in-plane and orthogonal to each other

In these experiments, the thin magnetostrictive patch was placed under the pole gap as shown in fig. 6.7(b). In this configuration, both the dynamic magnetic field B_d and the static magnetic field B_s are parallel to the surface of the patch while being orthogonal to each other. As before, the amplitude of particle velocity and the vibrational patterns were recorded in the X, Y and Z directions as a function of the excitation frequency and the amplitude of B_s.

By adopting this configuration, the Lorentz force amplitude is expected to be null (as any eddy current induced in the patch will be parallel to B_s), unlike the configuration where the bias field is in the out of plane. The results presented in Figure 6.10 represent the particle velocity in the case where the input power to the RF coil was equal to 450 W. Compared to the previous experiments presented in Figure 6.9, where the static magnetic field was in the out-of-plane direction, the vibration patterns are noticeably different. By adopting this configuration, even for a relatively low input power, the velocity magnitude in the X, Y and Z directions are significantly higher in the range of low frequencies up to 140 kHz. It can also be noticed that the signal dropped considerably in the range of high frequencies.

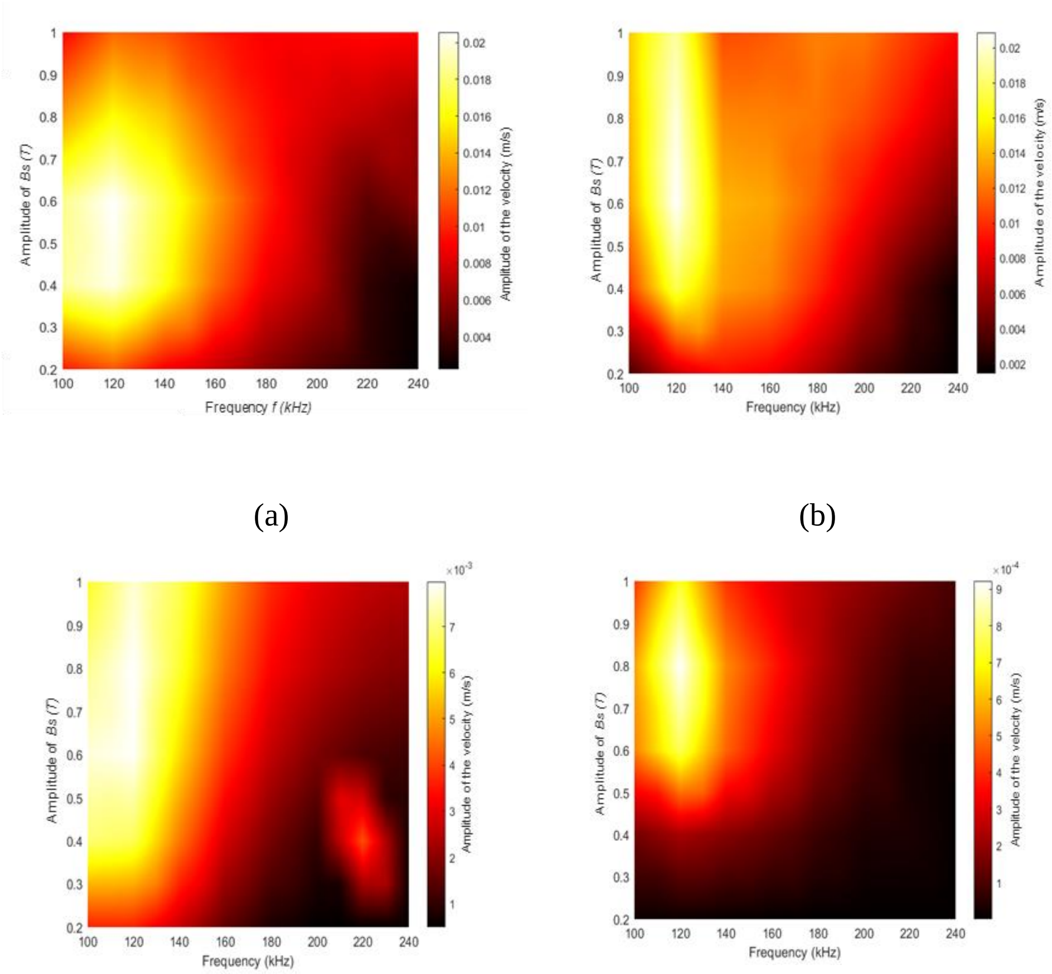

(a) (b)

(c) (d)

Figure 6.10. *Velocity mapping while varying both the static magnetic field* B_s *and the frequency in the (a) X, (b) Y, and (c) Z directions respectively. (d) The resultant magnitude of the particle velocity. The input power used to generate the dynamic field was 450 W throughout.* B_s *and* B_d *are in-plane and orthogonal to each other.*

The calculated magnitude presented in Figure 6.10(d) further reflects these significant changes in vibrational behaviour in the X, Y and Z directions. The magnitude is a maximum when the frequencies are in the 105-140 kHz range.

The second part of this set of experiments consisted of increasing the input power to the RF pulsing system to reach 1.8 kW. The results are shown in figure 6.11. By increasing the power of the pulsing unit generating the dynamic magnetic field, it can be seen that the distribution of the high amplitude range is expanded over a wider range of frequencies compared to the situation where the input power was equal to 450 W. In fact, the maximum values of amplitudes are reached in the range of frequencies between 120 kHz up to 160 kHz for the recorded vibrations in the Y direction and relatively high vibrational patterns can still be obtained even for higher frequency range reaching 200 kHz. Similarly, the maximum velocity is expanded to cover frequencies ranging from 105 kHz to 160 kHz in the X direction. It is also important to mention that the velocity amplitude in the X direction doubled from 0.02m/s to 0.04m/s and the amplitude in the Y direction increased by half from 0.02 m/s to 0.03 m/s. Nevertheless, the maximum recorded amplitudes in the Z direction are similar to the previous set of experiments, having relatively high velocity magnitude readings for frequencies below 120 kHz.

From the figure below, it can be noticed that even with this configuration, the vibrational response at 100 kHz remained relatively high. By comparing these results to the previous set of experiments where the static magnetic field was in the out-of-plane direction shown in fig. 6.9, the effect of the natural frequency mode vibration is less dominant compared to the magnetostrictive forces. The magnetostrictive forces were thus the dominant forces generating vibrations within the thin patch in this configuration.

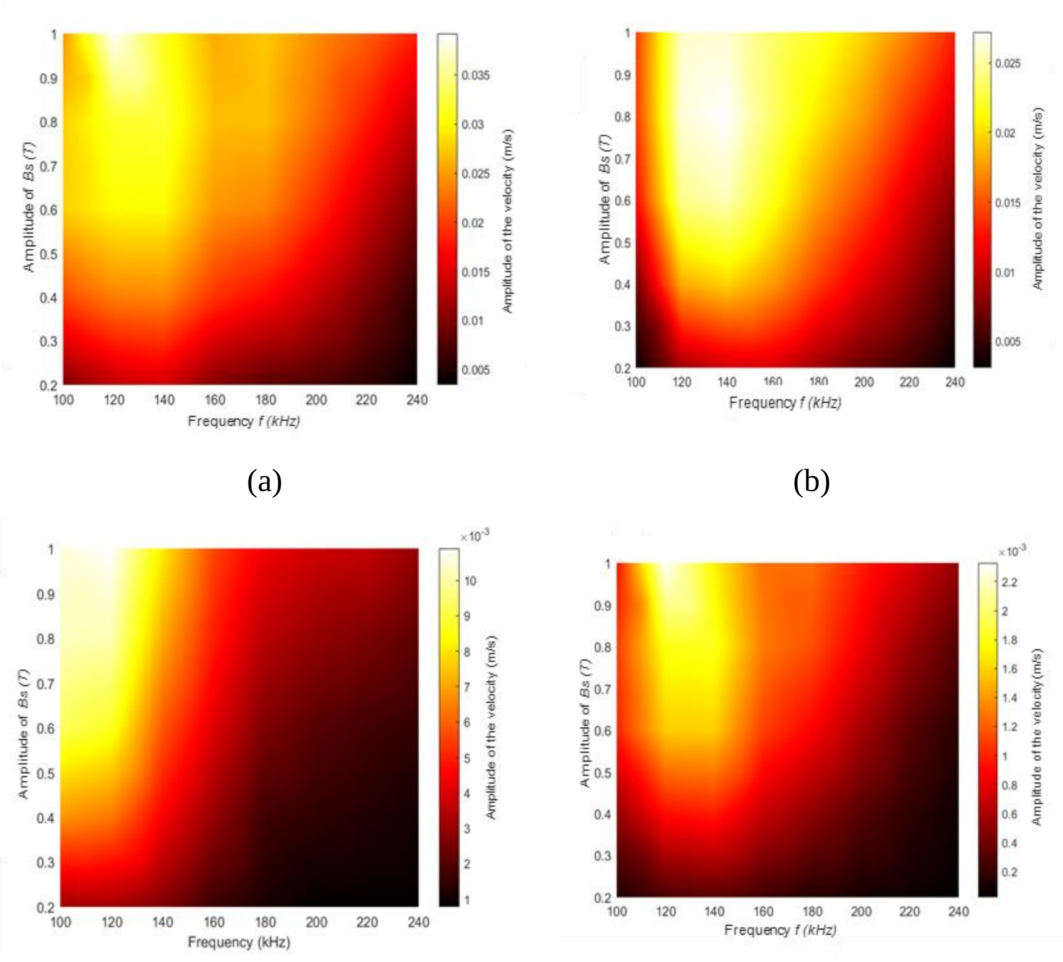

(a) (b)

(c) (d)

Figure 6.11. *Velocity mapping while varying both the static magnetic field B_s and the frequency in the (a) X, (b) Y, and (c) Z directions respectively. (d) A map of the resultant magnitude of the particle velocity. The input power used to generate the dynamic field was 1.8 kW throughout.*

It can be seen that when B_s and B_d were both in-plane, the vibrational amplitude was greater than when B_s was out of plane. In fact, the maximum magnitude of vibration increased from 2.5 x 10^{-4} m/s to 2.2. x 10^{-3} m/s, reflecting an increase by almost an order of magnitude. In addition to that, the operational frequency range, where the vibrational patterns are high to generate ultrasonic waves, had expanded leading to more combinations of static magnetic field applied/frequencies that can be selected to provide reasonable particle velocities levels via the patch.

By observing the results of these experiments, it was noted that by using a high-power input current to the PCB coil and by placing both B_s and B_d in-plane and orthogonal to each other, the vibration range of the patch is expanded to cover wider range of operational frequencies. The particle velocity magnitude increased with increases in B_s, but decreased when the excitation frequency was increased.

Further analysis of the experimental results collected when both the static magnetic field and the dynamic magnetic field were generated in the same plane but orthogonal to each other are presented in the figure 6.12. The input signal passing through the coil to generate the dynamic magnetic field was 1.8 kW, while various frequencies (100 kHz, 120 kHz, 200 kHz and 220 kHz) were selected. As B_s and B_d were orthogonal and in-plane, Lorentz forces should be negligible. The results are summarised in Figures 6.12 (a)-(d).

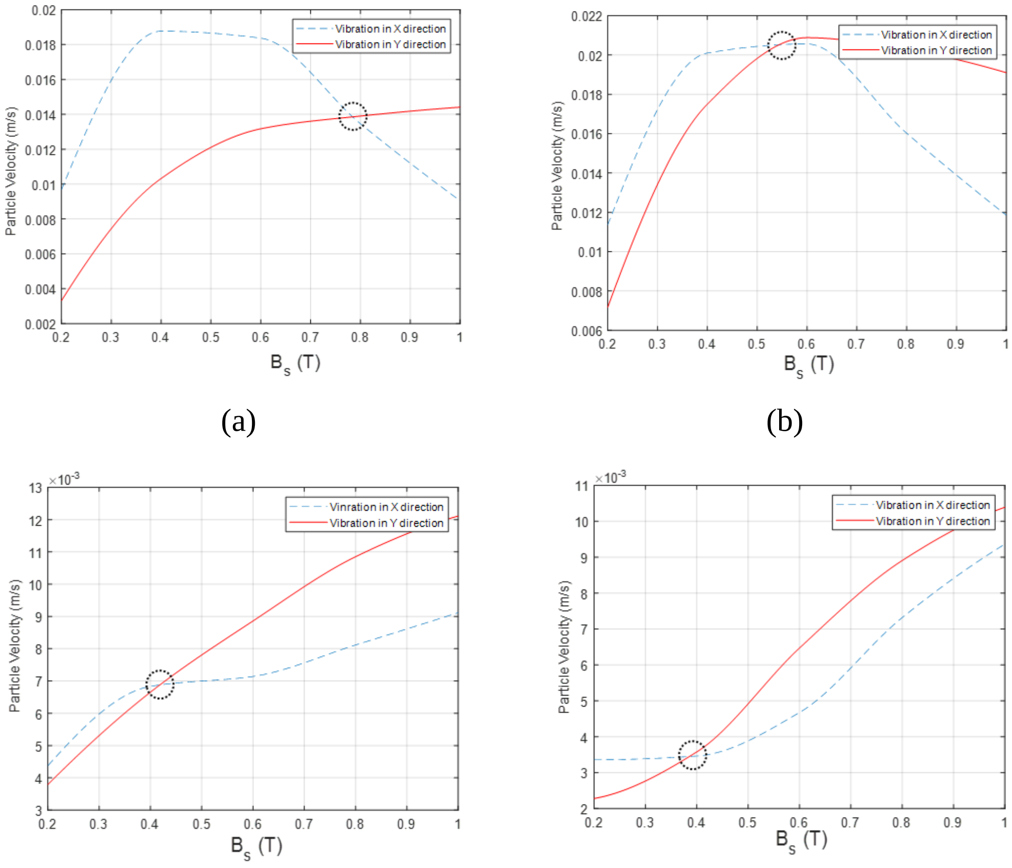

(a) (b)

(c) (d)

Figure 6.12. *Magnetostrictive patch vibration in the X and Y directions as a function of static magnetic field amplitude for (a) 100 kHz, (b) 120 kHz, (c) 200 kHz, and (d) 220 kHz.*

It can be seen in Figure 6.12 that the amplitudes in the X and Y directions exhibited a non-linear behaviour when B_s increased. These observations are in good agreement with the previous sets of experiments. At low frequencies, the gradient of the vibration in the Y direction is slightly decreasing for B_s in the 0.4 - 0.6 T range, but that then the vibrational amplitude decreased more rapidly once B_s was >0.6 T. Conversely, when relatively high frequencies were used for B_d, the vibrations in the X and Y directions exhibited similar patterns, with the vibration amplitude increasing when B_s was increased.

An interesting point is that when B_s is increasing, the velocity magnitude in the Y direction surpasses that in the X direction at some point. This “switch point” is circled in each case in Figure 6.12. It tends to be at lower B_s values at higher frequencies. As a matter of fact, the switch point can be used in order to generate a specific wave with a main directivity pattern which will enhance specific wave modes and optimise the inspection process

6.5. Discussion

The series of experiments conducted in this chapter have shown that amplitude and direction of the applied dynamic magnetic field (B_d) and the static magnetic field (B_s) have an important effect on the generation of the magnetostriction within a thin ferromagnetic patch. The results show that by varying the frequency of the dynamic magnetic field and the amplitude of the static magnetic field, the vibrations generated via the magnetostriction effect and the Lorentz force effect can be enhanced and controlled. The analysis showed a complex interaction between the vibration as a result of both magnetostriction and Lorentz forces and those generated due to natural vibrational modes of the patch at around 100 kHz. Note that these natural frequencies are likely to be modified once a patch was attached to a sample, and may well be damped.

When both B_s and B_d were in-plane, Lorentz forces were expected to be minimal, allowing observation of only the effect of magnetostrictive forces. This configuration was tested at two levels of coil energizing power (450 W and 1.8 kW). At 450 W, the patch performance was limited to a narrow frequency/static magnetic field amplitude range. This is primarily due to the fact that the input power used to generate the magnetostrictive forces within the patch was relatively low. B_s tends to align the magnetic domains in its direction while B_d provides modulation and hence the creation of vibrations. In the case where the input power is low, this modulation is limited. Conversely, when the input power was increased to 1.8 kW, the magnitude of the vibrations in the X, Y and Z directions was significantly enhanced, with reasonable vibrational levels observed at higher frequencies of up to 240 kHz. This led to a wider operational range.

Another interesting observation was the switching point shown in Figure 6.11. At low frequencies, a higher amplitude of the static magnetic field is required in order to maintain a dominant vibration in the Y direction, but the B_s switching point decreases at higher excitation frequencies. The energy induced in the magnetostrictive patch for higher frequencies is decreasing. Rotation of magnetic domains is then controlled by the direction of B_s, while B_d is only providing modulation.

6.6. Conclusions

A laser vibrometer system was used in order to capture the vibrations generated as a result of the magnetostriction within a ferromagnetic patch, when parameters such as the frequency, the amplitude and the direction of the dynamic magnetic field and the static magnetic field were varied. It was shown that the signal generated from magnetostrictive forces can be enhanced by either increasing the oscillating frequency or modifying the amplitude and direction of the applied magnetic fields (both static and dynamic magnetic fields). It was shown that by simply placing the static magnetic field in the same plan as the dynamic magnetic field while both being parallel to the surface of the patch can significantly increase the vibration amplitude due to the magnetostrictive forces.

It was also shown that for the low frequency range, the effect of the static magnetic field when acting in the out-of-plane direction has minimal effect on the vibration amplitudes. Conversely, patch performances can be enhanced using in-plane static and dynamic fields. It was shown also that by increasing the amplitude of the dynamic magnetic field B_d, the operational range of the patch can be significantly expanded.

The work reported in this chapter and the previous one provided a better understating on the effect of the variation of key parameters affecting the generation of magnetostrictive forces. The selection of specific combinations of excitation frequency, direction and amplitude of static magnetic field and dynamic magnetic field is critical for generating a relatively high amplitude signal that can be used in the NDT operations. The next Chapter demonstrates this for the inspection of composite plates.

References for Chapter 6

[1] Wang, P.W. and Cheng, C.C., 2005. Natural frequency tuning using structural patches. J. Vib. Acoust., 127(1), pp.28-35.

Chapter 7: Defect detection in composite structures using magnetostrictive patch transducers

Ultrasonic inspection is a widely-used technique for the non-destructive inspection of composite material parts. Chapters 4 and 6 reported experimental work that was conducted to investigate the different excitation parameters on the generation of magnetostriction within a thin iron-cobalt alloy patch. It was found that the vibrations generated within a patch could be controlled by varying the frequency, direction and amplitude of both the dynamic and static magnetic fields. In this chapter, the aim is to investigate the use of magnetostrictive thin patches to generate guided waves in a composite structure for NDE purposes. Here, a thin patch is attached to the surface of the composite plate, and the generated SH0 and A0 modes are used to detect defects in the form of an artificial defect in a carbon fibre reinforced polymer (CFRP) plate and delamination damage within a glass fibre reinforced polymer (GFRP) plate. The synthetic aperture focusing technique (SAFT) is then used to provide imaging of the defects in both samples.

7.1. Experimental apparatus

The first set of experiments was designed to capture and understand the elastic wave propagation in a CFRP composite material, using the vibrometer to test the different configurations reported in chapter 4 (which described results from an isotropic, non-magnetic sample). This allowed specific combinations of frequency, wave propagation direction and amplitude of the dynamic and static magnetic fields to be controlled, to optimize performance. The second set of experiments investigated the detection of defects within composite samples using magnetostrictive patches, as both a transmitter and as a detector. Subsequently, the SAFT algorithm was used to provide imaging results for detecting defects within both CFRP and GFRP plates. It is important to mention that the electromagnet was not used for these sets of experiments.

7.1.1. Experimental apparatus for initial experiments in composites

The pulsing system used to drive the transducers was the Innerspec RF Unit. This contains a high-power pulsing unit connected to a flat coil, to generate the dynamic magnetic field that is applied to the thin patch, together with a data-acquisition system to which a second detection coil can be connected. This module is used to collect the data and apply filters to enhance the signal and extract the required features.

This first set of experiments was designed to investigate the propagation of the guided waves in a defect-free composite sample, using the vibrometer to detect guided wave signals from a single transmitter. As in previous chapters, the magnetostrictive patch used to generate the guided waves within the composites was the iron-cobalt alloy VACOFLUX 48. This material was selected, as it retains high levels of magnetostriction around 70 ppm, and offers a level of flexibility in terms of design as it is easily cut into the required shape. The patch used for these experiments was cut into a strips of 400 mm length and 40 mm width.

The representation of the experimental setup is presented in figure 7.1. Figure 7.1(a) shows a representation of the vibrometer grid detection points on the plate, with the coil and permanent magnet combination placed above the horizontal strip-shaped patch. Figure 7.1(b) is a schematic diagram of the apparatus.

The input signal to the coil from the Innerspec current pulsing unit, consisted of a windowed sinusoidal current pulse of 3 cycles at 120 kHz. The nominal power issued from the pulsing unit was quoted by the manufacturer as 1.8 kW.. The selection of these initial parameters was based on the analysis conducted in the previous chapters. This combination of the number of cycles and frequency allowed the capture of guided waves in all of the four configurations reported previously in the Chapter 4.

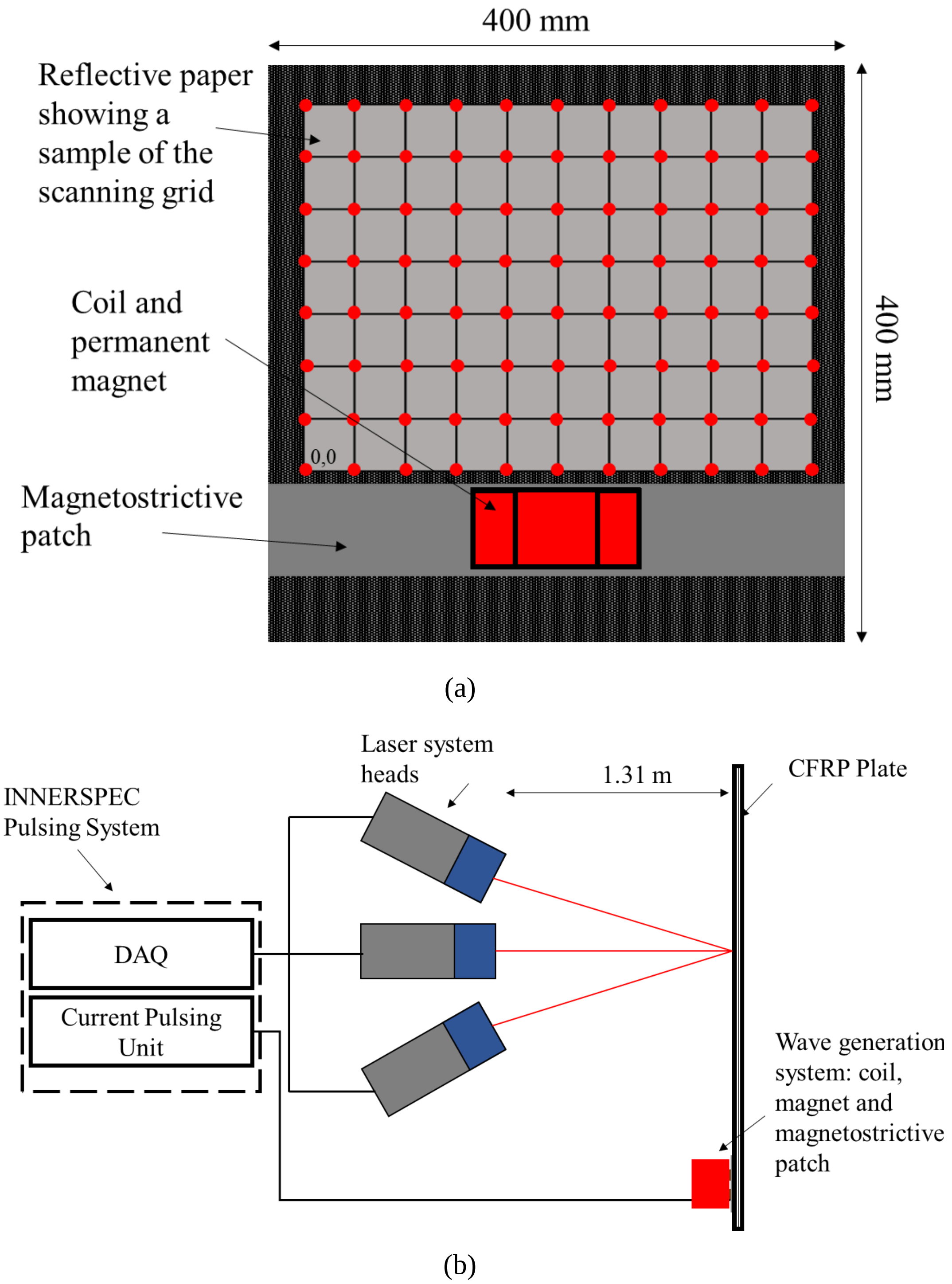

Figure 7.1. *Diagram for the experimental apparatus used to investigate the generation of guided waves using MPT: (a) Front view showing the relative position of the coil and magnet system, the magnetostrictive patch and a graphical representation of the reflective grid used to collect data using the PSV 3D laser system. (b) Schematic diagram of the apparatus.*

For these experiments, the racetrack coil and a pancake-shaped coil were used to generate dynamic magnetic fields in different directions. The racetrack coil, used in configurations 1 and 2, consisted of a coil (35 µm thick) printed onto a PCB, with a thin electrical insulation film applied to the top of the coil, to avoid any short-circuiting when the coil was in contact with the electrically conductive magnetostrictive patch. The coil (figure 4.3(a)) consisted of 10 turns, with a track width of 1 mm and a track spacing of 0.5 mm, using 35 µm thick copper. The overall width of the racetrack coil was 14.5 mm. For configurations 3 and 4, a circular coil (figure 4.3.(c)) was used, consisting of 5 turns with a 1 mm track width and a 0.5 mm spacing. In all cases, the thickness of the PCB fibreglass substrate was 1.5mm. As described in earlier chapters (chapter 4, figure 4.3.(b)), a U-shaped alnico grade 5 permanent magnet was used to generated the static magnetic field for configurations 1, 2 and 4 (chapter 4, figure 4.4). The shape of the magnet allowed the generation of an in-plane static magnetic field. In the case of configuration 3 (chapter 4, figure 4.4), a circular N42 permanent magnet was used for the required out-of-plane static magnetic field.

A thin, optically reflective tape was attached to the structure, to improve the reflectivity for vibrometer measurements, for investigating the propagation of the elastic waves in a composite material plate. This tape increased the reflectivity of the sample, without any significant change to the elastic properties of the sample. The vibrometer used was a POLYTEC PSV-400 3D laser system, as described in chapter 4. The detected signal was post-processed using the DAQ cards mounted within the Polytec system. The laser head was placed a distance of 1.31 m from the sample surface, so as to allow the scan of the full area, while maintaining an optimal level of back-scattered light to the laser head. As shown in figure 7.1(b), the scan was conducted based on a series of adjacent points, with the spacing of the points chosen to give approximately 32 points for the nominal wavelength of the SH0 mode at 120 kHz. The grid resolution was increased to capture the S0 mode. As it is the fastest mode for the selected frequency, the capture of A0 mode was permitted through the same spatial resolution. It is important to note that the data points shown in the figure 7.1(a) are schematic representation of the scanned grid, and are not the actual spacing between experimentally measured points

7.1.2. Experimental apparatus for defect detection in CFRP and GFRP composites

The second set of experiments that was conducted as part of this research was investigating the capabilities of magnetostrictive patches combined with a coil and a permanent magnet, to detect defects within a composite structure. These experiments helped in analysing the effect of applying different configurations of excitation frequency, direction and amplitude of both the dynamic magnetic field and the static magnetic field on the detection of the defect. This used separate transmitter and receiver units.

The first sample studied was a 400 mm x 400 mm CFRP flat panel of 3 mm thickness with 15 plies in a [0º 90º 0º 90º] layup configuration. It contained a circular through-thickness defect of 20 mm diameter and 1.5 mm depth that was machined into the surface of the CFRP plate. For these experiments, a linear scan using mirrored coil/patch systems was performed along the patch, with a spatial step of 1 mm, at a distance of 100 mm from the defect. Figure 7.2 (b) shows the apparatus used for signal capture. It consisted of two transducers, placed close to each other, with one acting as transmitter and the other as a receiver. A strip-shaped patch of 90 mm width and 400 mm length was used to allow each transducer to move in tandem across the sample.

Both were contained within the patch dimensions. The size of each transducer arrangement was 42 mm x 70 mm, with a gap of 2 mm between the source and receiver. The coil used for generation was connected to the Innerspec RF current pulser, while the sensing coil was connected to the DAQ panel of the same system. An internal trigger pulse was used at the trigger for acquiring the reflected signal. The sampling rate of the data acquisition was 25.6 MHz, and the power of the pulsing system was set to a nominal 1.8 kW. A digital filter was applied to the collected signal, using an FPGA built into the signal acquisition electronics. It consisted of a gated-signal with a smoothing function of 32 points. To identify specific ultrasonic wave arrivals and the different reflections presented in the received waveform, digital gates were designed within the data acquisition system to capture the reflected signal, the amplitude and the time of arrival. This configuration led to the analysis of the different wave modes reflected from the defect. These gates are presented in figure 7.2 (c). The gates allowed the discrimination of the signals corresponding to reflections generated from the defects, and assisted in partially identifying the reflections generated from the back wall of the CFRP plate, and the reflected signal from the side edges of the plate.

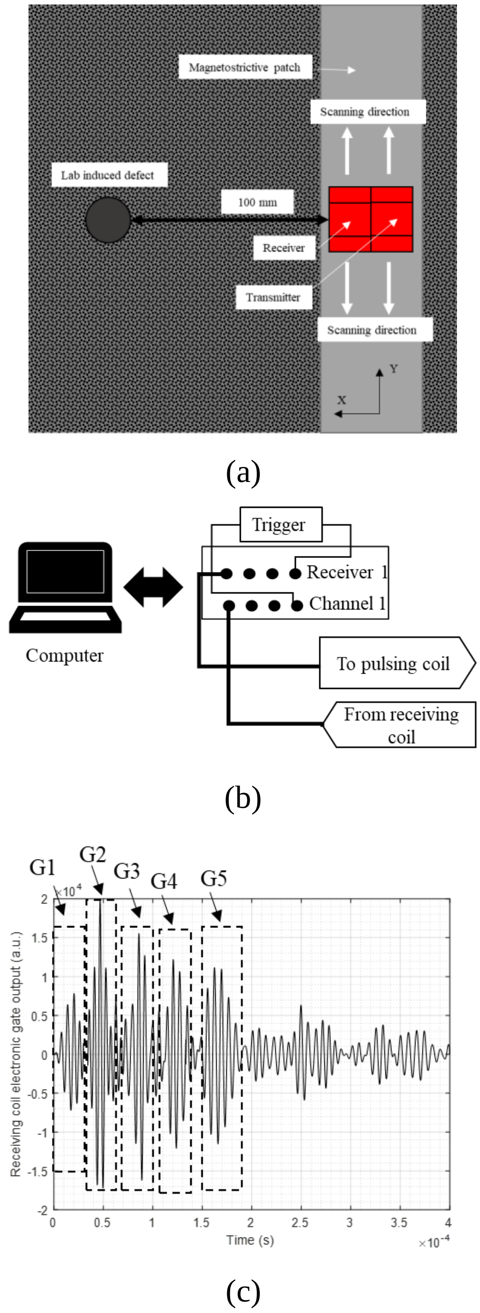

Figure 7.2. *(a) The experimental geometry and (b) the apparatus for demonstrating the defect detection capabilities and (c) waveform of the received signal showing the tracking gates numbers used to identify the received signal and the corresponding interactions of the wave with structural features (edge and defect reflections)*

Figure 7.3 shows the 3-cycles current waveform which was input to the coil to generate the dynamic magnetic field. The current was induced to the coil through the pulsing unit embedded within the Innerspec system. The figure 7.3(b) shows the frequency spectrum associated with the 120 kHz current signal.

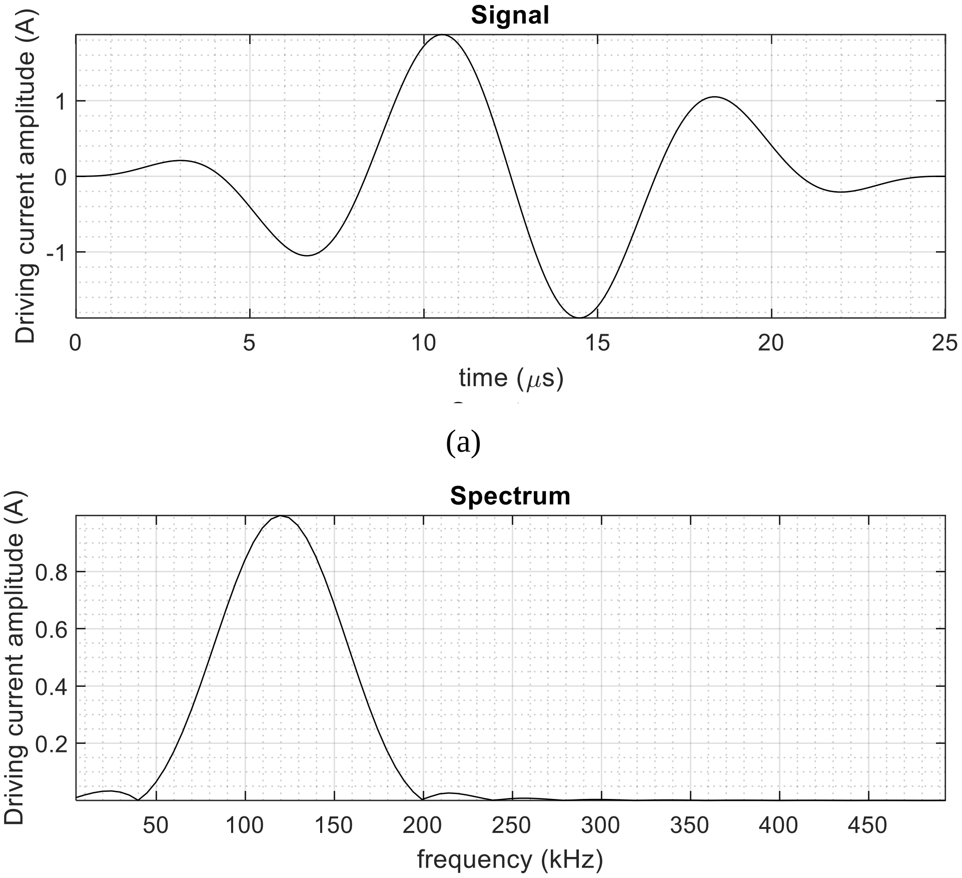

(a)

(b)

Figure 7.3. *(a) Current waveform induced in the excitation coil connected to the RF pulsing unit within the Innerspec system and (b) its respective magnitude FFT*

Experiments were also performed on a 1 m x 1 m square, 4 mm thick GFRP plate, containing a delamination. The delamination shape is a rectangle which is 15mm wide and 25 mm long. The delamination was introduced using a PTFE layer within the middle plane (2 mm) of the GFRP plate.

7.1.3. Synthetic aperture focusing technique (SAFT):

In order to characterize defects embedded within the thickness of a sample, different imaging techniques were used to produce an image of the defects which helps with flaw characterization. Initially, ultrasonic testing generated a B-scan which is a representation of the amplitudes of the reflected signal as a function of time. By capturing multiple B-scans, a lateral image of the scanned area could be reconstructed. These images can include reflectors or scatterers based on the reflected signal time of arrival and amplitude drop. There are multiple technologies used for NDT application that have the defect imaging capabilities such as in radiography using X-rays [1] and thermography [2]. Although these technologies provide excellent results, ultrasonic imaging was selected due to the limitations of radiography such as health and safety issues and limitations of thermography due to the experimental setup requiring advanced equipment.

The use of multiple B-scans to reconstruct the image of the defect using UT inspection methods is critical to build the synthetic aperture focusing technique (SAFT). In fact, the UT signal tends to diverge or scatter when interacting with a defect which reduces significantly the lateral resolution of the detection [3, 4]. The SAFT technique is an excellent method to increase the lateral resolution in order to precisely characterize the defect in terms of location and dimensions.

Many different algorithms have been used for SAFT. These algorithms can be executed either in the time-domain or the frequency-domain [5]. One of the established algorithms in the frequency domain is the phase shift migration (PSM). The PSM [6, 7] method is usually used in seismology based on the assumption that the reflected signal from all reflectors and scatterers would “explode” when time $t = 0$ and the resultant field velocity would be half the propagation velocity of the induced signal. The PSM approach has been used in this work.

To reconstruct the image using SAFT PSM method, a sensor should be placed at a fixed distance and perform a linear sweep with equal distance steps as shown in fig. 7.2.(a). Both the emitter and receiver are scanning linearly, in the Y direction, the composite plates in a pitch-catch configuration and the ultrasonic wave is travelling I the X-Y plane.

Initially, a wave field received by the receiver (coil and permanent magnet system) $p(t, y, X)$ is considered where t is the time, y is the sensor linear sweep position and X is the location of the sensor at the start of the scan. Then, the collected signal is transformed using the Fourier transformation into the frequency domain as $P(\omega, k_x, Y)$ which will be extrapolated to other distances Δy. The next step is that every Δy is multiplied by the phase shift factor equal to $e^{ik_y(y-Y)}$ where y is the sensor linear sweep position and Y is the direction of the wave travelling in the X-Y plane. The third step consists of evaluating the wave field when $t = 0$. This process is called "imaging condition".

Finally, the extrapolated field is inversed to the time domain through the application of inverse Fourier transformation leading to the generation of focused image revealing all the reflectors and scatterers [7].

7.2. Results

7.2.1. *Effect of different configurations on guided wave generation*

The first set of experiments consisted of analysing the propagation of elastic waves in the CFRP composite plate. Collected data is presented in figures 7.4-7.7 and the magnitude of the particle velocity calculated as previously defined

$$|A| = \sqrt{A_X^2 + A_Y^2 + A_Z^2} \tag{7.1}$$

where A_X, A_Y and A_Z are the particle velocities in the scan direction X, Y and Z respectively.

As can be seen from the figures 7.4-7.7, the different configurations led to the generation of elastic waves with different propagation patterns. The coil and permanent magnets were placed at the starting point of the scan and a linear sweep was performed to collect the reflected signal. The figures below include the previously analysed radiation patterns of the patch leading to the generation of guided waves in an isotropic plate when subject to the different configurations. The plots were included as a reference to understand the generation patterns observed on a CFRP plate. These results were initially presented in chapter 4. In the case of configuration 1 as shown in figure 7.4, there is a significant amplitude SH0 mode propagating in the Y direction, but also at other angles. The SH0 was identified based on the propagation velocity and by comparison to the data collected and presented in chapter 4. In addition, the laser system used to collect the data is capable of detecting motion in-plane and out-of-plane direction which helped in distinguishing the different generated waves components.

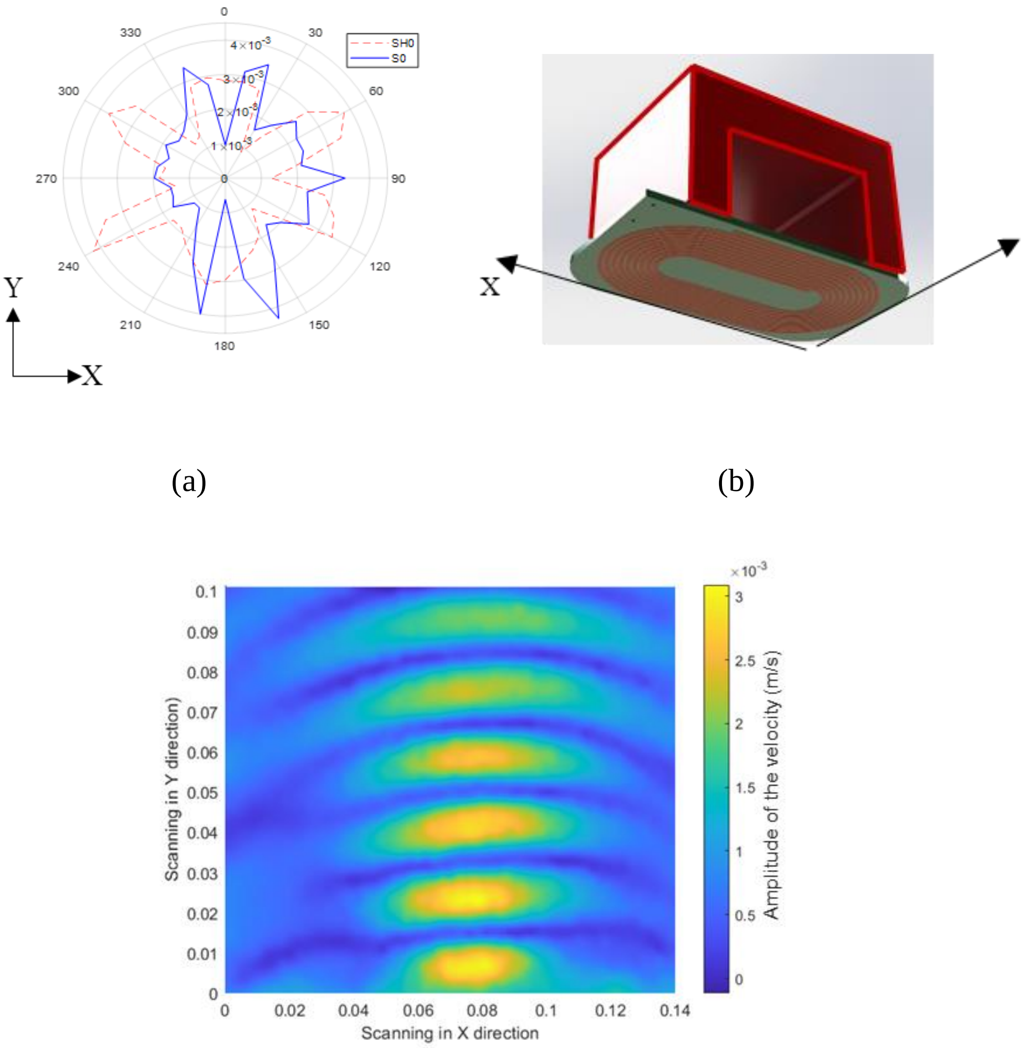

(a) (b)

(c)

Figure 7.4. *Elastic wave propagation patterns determined via Eqn. (7.1) from the Polytec vibrometer on a defect-free CFRP plate for Configuration 1 showing (a) the polar radiation reported in chapter 4, (b) coil and permanent magnet arrangement and scanned area showing the propagation of elastic waves*

The SH0 wave propagating in the Y direction is consistent with the Wiedemann generation mechanism. Note that the dynamic and static magnetic fields are applied in the Y and X direction respectively. From the patch scan, it can be seen that a high vibration amplitude vibration is concentrated in the X direction, associated with the SH0 wave. It should be noted, that all four configurations will generate more than one type of guided wave mode, generally with complicated directivity patterns. While these wave modes can in principle be separated due to their different group velocities, this figure just shows the overall amplitude via eqn. (7.1). These findings are consistent with the radial analysis conducted in chapter 4, as the SH0 amplitude is higher than the S0 mode amplitudes when the transducer is placed at the 0º angle.

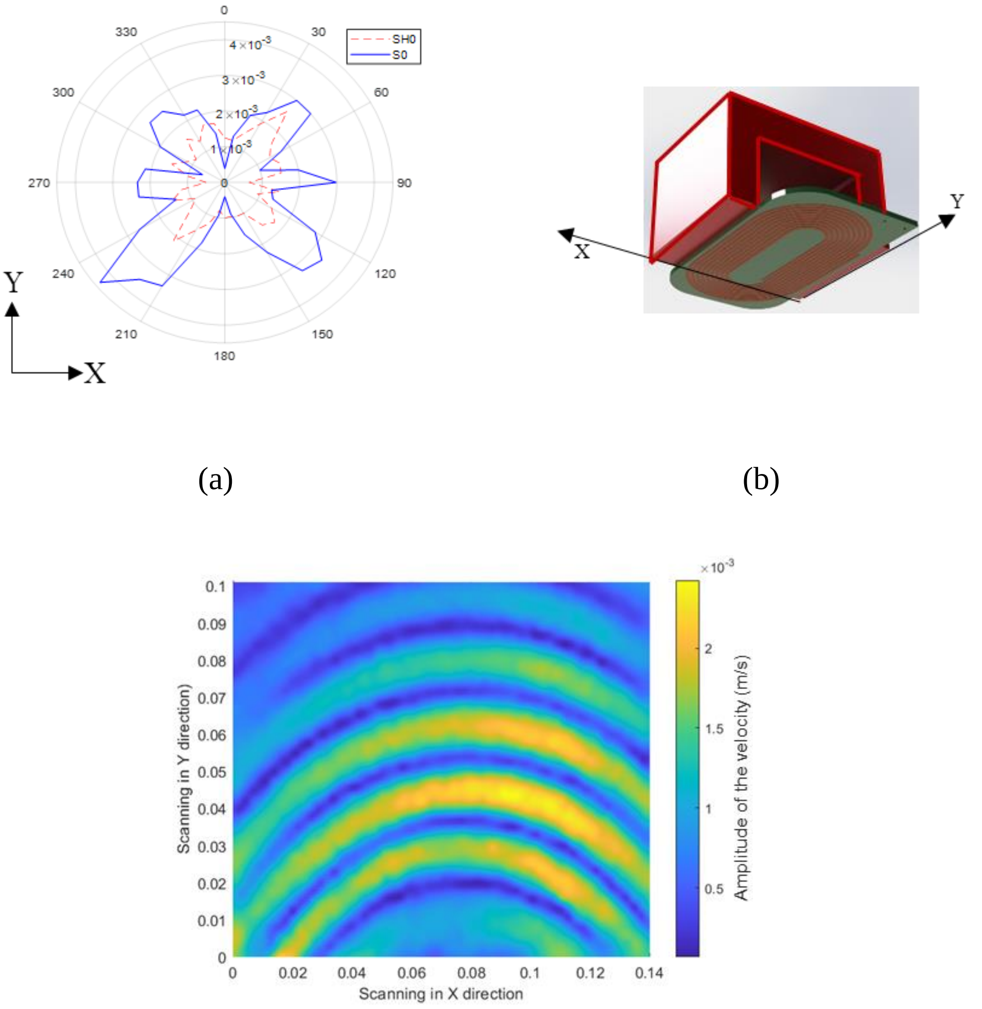

(a)

(b)

(c)

Figure 7.5. *Elastic wave propagation patterns determined via Eqn. (7.1) from the Polytec vibrometer on a defect-free CFRP plate for Configuration 2 showing (a)*

the polar radiation reported in chapter 4, (b) coil and permanent magnet arrangement and scanned area showing the propagation of elastic waves

On the other hand, configuration 2 (fig.7.5) generated a more divergent beam, noting that now forces are generated in the Z direction. For an in-plane static magnetic field on a ferromagnetic sample, one would generally expect the Lorentz force to almost cancel out the magnetisation force. The shape of the guided wave wavefront generated from the configuration 2 is propagating in an elliptical pattern, which is consistent with the patch vibration pattern presented in chapter 4 and is also seen in figure 4.10.

Configuration 3 led to fairly omnidirectional guided wave wavefront, which was generated through a combination of magnetostrictive and Lorentz forces, with the latter being generated parallel to the surface of the magnetostrictive patch transducer. In fact, the patch is subject to omnidirectional forces, which can be split into surface normal forces and shear forces. The force generated in the normal direction is contributing to the generation of S0 wave mode, while the shear forces are contributing to the generation of SH0 wave modes, and a normal incidence through thickness SH bulk wave. As can be seen from the radial directivity pattern in figure 7.6, the average amplitude of S0 and SH0 is fairly uniform, with both modes are being generated at all angles. Similar to the previous configurations, S0 and SH0 modes were detected using the 3D laser system and the travelling velocity in order to precisely distinguish both modes.

Finally, in configuration 4, the Lorentz forces generated have a complex spatial distribution as the angle of the dynamic field relative to the static field changes around the coil, and are mainly in the Z direction. As discussed in chapter 4 and was mentioned for configuration 2, the Lorentz forces are mostly cancelled out with the opposing magnetisation forces, leading to a vibration pattern mainly originating from magnetostriction forces.

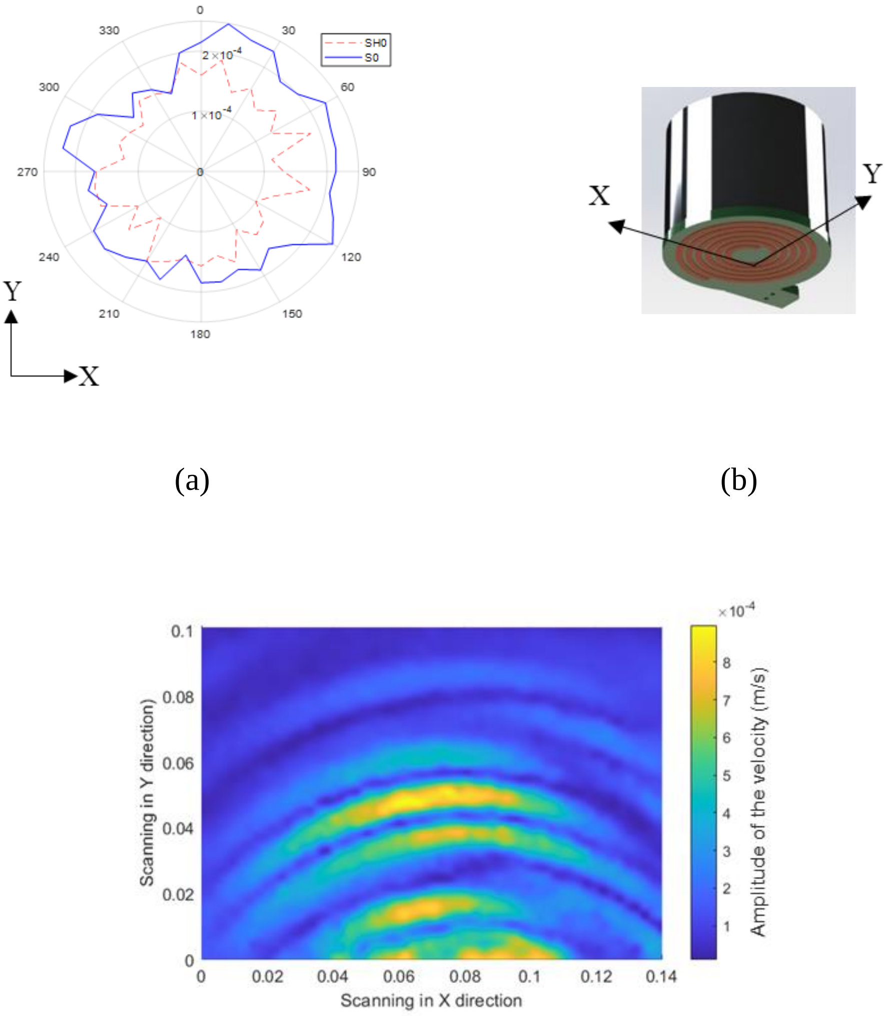

(a)

(b)

(c)

Figure 7.6. *Elastic wave propagation patterns determined via Eqn. (7.1) from the Polytec vibrometer on a defect-free CFRP plate for Configuration 3 showing (a) the polar radiation reported in chapter 4, (b) coil and permanent magnet arrangement and scanned area showing the propagation of elastic waves*

By analysing the forces resulting from the interaction of the static magnetic field and the dynamic magnetic field, it can be noted that the forces present in configuration 4 are similar to those in configuration 1: The twisting effect of the force in the patch during the excitation of the coil lead to the Wiedemann effect, which enhanced the generation of SH0 focused in the Y direction. In-plane forces are expected in the X direction, leading to the generation of the S0 wave mode. It can be seen from the figure

7.7, that S0 mode polar plot exhibits high amplitude focused lobes at an offset angle compared to the Y direction, while SH0 waves mainly propagate in the Y direction. In fact, the radiation pattern in configuration 4 is wider than with configuration 1, but narrower than that of configuration 2. These differences would affect the imaging outputs reconstructed later in the following sections. Note that the particle velocities of the wave displacements are similar for configurations 1, 2 and 4 (~ 2 x 10^{-3} m/s), while being significantly lower for configuration 3 (8 x 10^{-4} m/s).

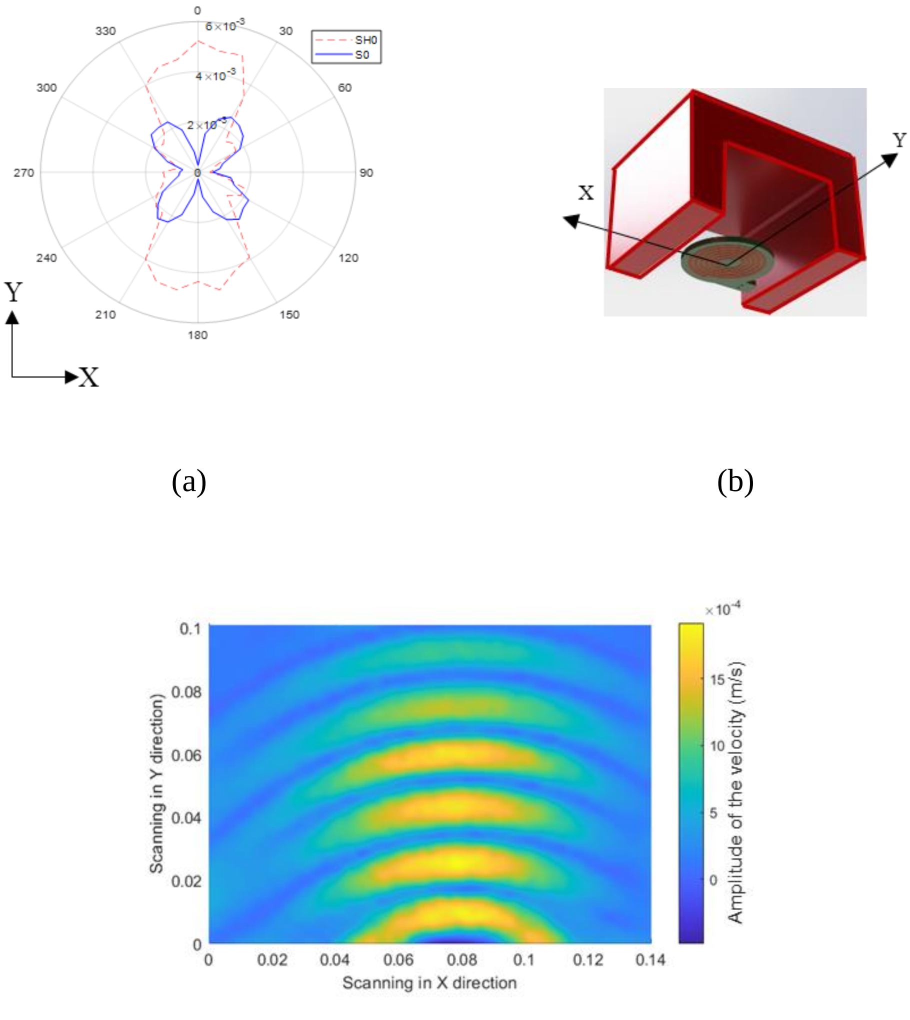

(a) (b)

(c)

Figure 7.7. *Elastic wave propagation patterns determined via Eqn. (7.1) from the Polytec vibrometer on a defect-free CFRP plate for Configuration 4 showing (a) the polar radiation reported in chapter 4, (b) coil and permanent magnet arrangement and scanned area showing the propagation of elastic waves*

Configurations 1 and 4 favour the generation of in-plane shearing or twisting forces in the X direction which led to the generation of SH0 waves propagating in the Y direction. In the case of configuration 2, the generation of the A0 mode was favoured in the Z (out of plane) direction. Finally, configuration 3 led to the generation of Lamb waves A0 and S0 as well as shear horizontal waves SH0

The elastic waves presented in figure 7.4 were further studied to identify the modes based on the time of arrival to distinguish S0, A0 and SH0. The amplitudes of the identified wave modes are used to analyse the wave amplitude decay, for which results are presented in figure 7.8.

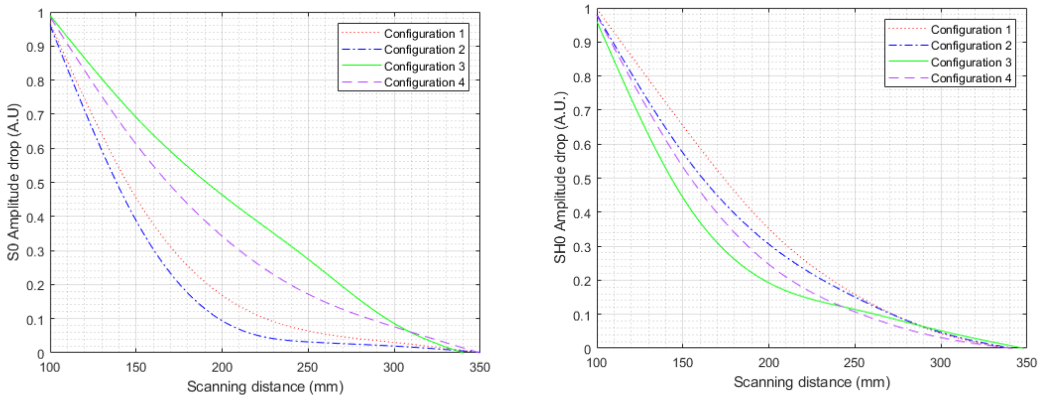

S0 SH0

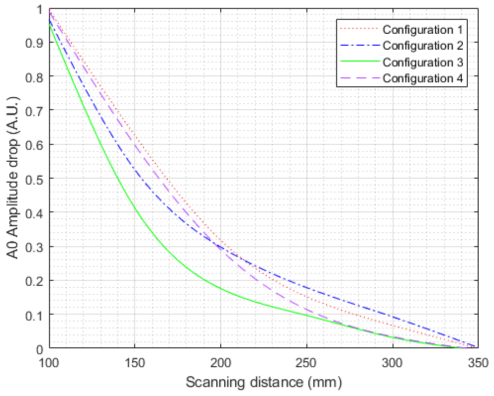

A0

Figure 7.8. *Guided ultrasonic waves amplitude drop for an elastic wave generated by a MPT attached to a defect-free CFRP plate collected for the: (a) Lamb waves symmetric mode, (b) shear horizontal wave mode and (c) Lamb waves antisymmetric mode*

The amplitude decay was analysed in function of propagation distance in the CFRP plate. It can be seen that in most cases a detectable amplitude of 10% of the initial maximum signal is preserved at distances of up to 250 mm from the centre of the transducer. In the case of the configuration 3, the wave amplitude for the A0 and SH0 modes are dropping rapidly as 60% of the amplitude is dissipated within the distance of 150 mm. It can be noticed that the S0 mode can be generated by configuration 1, even in the presence of high amplitude SH0 waves, and it can be enhanced by rotating the transducer slightly to 15º and configuration 3, which is consistent with the previous set of experiments. Although the amplitude of the S0 wave generated by configuration 3 is significantly lower than the amplitudes of the waves generated by the other configurations, configuration 3 can still be used for S0 measurements, within short propagation distances of up to 200 mm.

7.2.2. Effect of different magnetic configurations on the detection of a defect

The following set of experiments were designed to investigate the detectability of a simulated defect using the different configurations of static magnetic field and dynamic magnetic field when applied to a magnetostrictive thin patch attached to a CFRP plate. The sensors were placed at 100 mm distance from the defect, and a linear sweep performed by moving the transmitter/receiver pair along the magnetostrictive strip patch at 1 mm steps as shown in the figure 7.2.a. The reflected signal amplitude from the defect and received by the sensor is plotted in figure 7.9.

It can be seen that the four configurations give different results. By using configuration 1, the defect location can be detected precisely, as this configuration generated a SH0 guided wave mode with narrow beam. Conversely, configuration 2 (using an SH0 mode signal) returned a wider detection aperture with a steep increase in the reflected signal around the correct defect location. Configuration 3 provided the widest detection pattern for the defect from its fairly omnidirectional SH0 mode guided wave pattern. Configuration 4 returned a similar trend to configuration 1 for the SH0 mode but with a wider detection aperture. Using configuration 4, the defect can be detected from a longer distance as the pattern is wider compared to configuration 1.

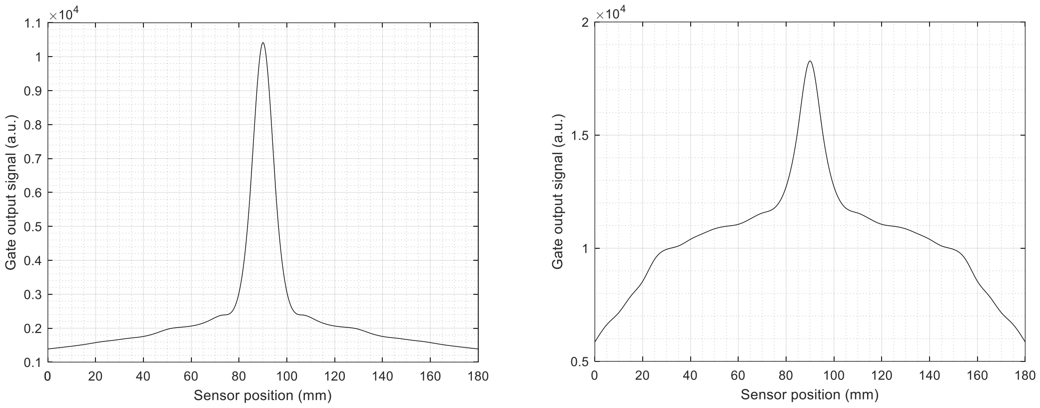

Configuration 1 Configuration 2

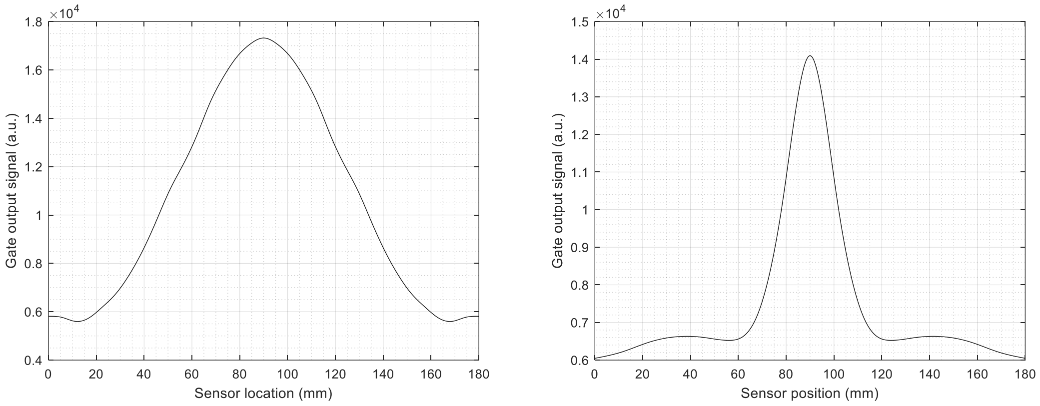

Configuration 3 Configuration 4

Figure 7.9. *Defect scanning and detection using a 1 mm linear sweep. The data collected using 2 similar configurations of coils, permanent magnetic and magnetostrictive patches. The analysed reflected wave is SH0*

Similarly, by adopting the A0 mode to detect the defect, it can be seen that configuration 1 returned good results in terms of detectability as the beam was narrow which led to a precise detection of the lateral position of the defect. as seen in figure 7.10. Configuration 2 provided a more complex reflected signal which led to the detection of the defect but in a slightly offset location to the real defect. Configuration 3 and 4 led to the imagining of the defect with lower lateral and vertical resolutions, this is mainly due to the fact that the guided waves beam is wider which contributed to a flattened defect rather than a circular image which is the true representation of the flaw.

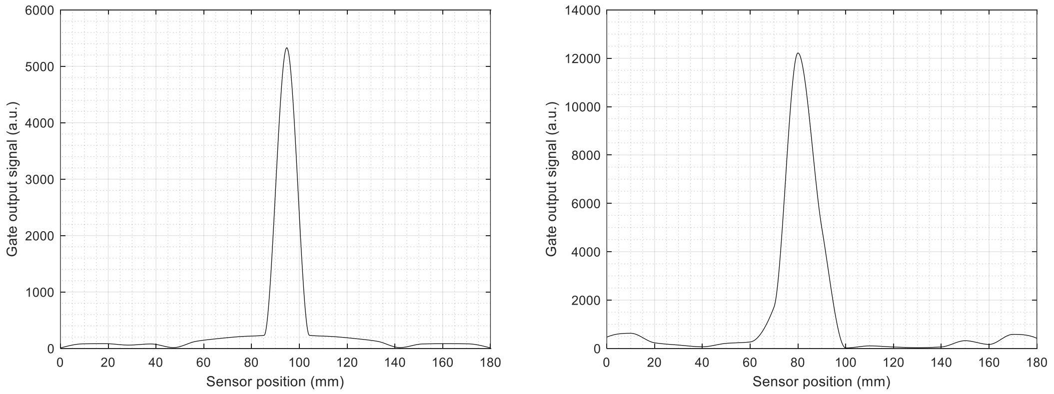

Configuration 1 Configuration 2

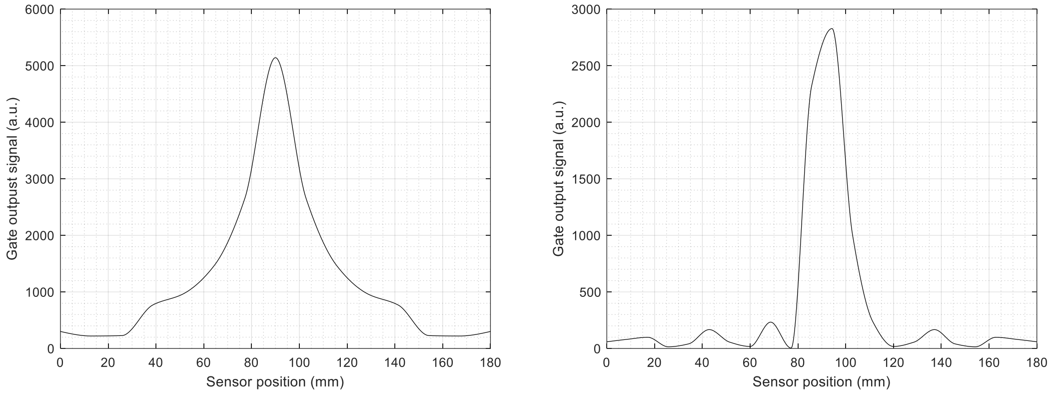

Configuration 3 Configuration 4

Figure 7.10. *Defect scanning and detection using a 1 mm linear sweep. The data collected using 2 similar configurations of coils, permanent magnetic and magnetostrictive patches. The analysed reflected wave is A0*

The above shows that a magnetostrictive patch system has great flexibility in terms of defect detection using different guided wave modes, each of which has different characteristics.

7.2.3. Defect detection in a CFRP plate using the SAFT technique

By compiling the reflected signals from the defect, an image of the defect can be reconstructed using the SAFT method, using different combinations of dynamic magnetic field and static magnetic field. A tracking gate was available to select the signal from a given wave mode as the transducer pair was scanned along the magnetostrictive strip. An example of how the gate was used is shown in figure 7.11 for configuration 1, showing how the SH0 and A0 modes could be detected.

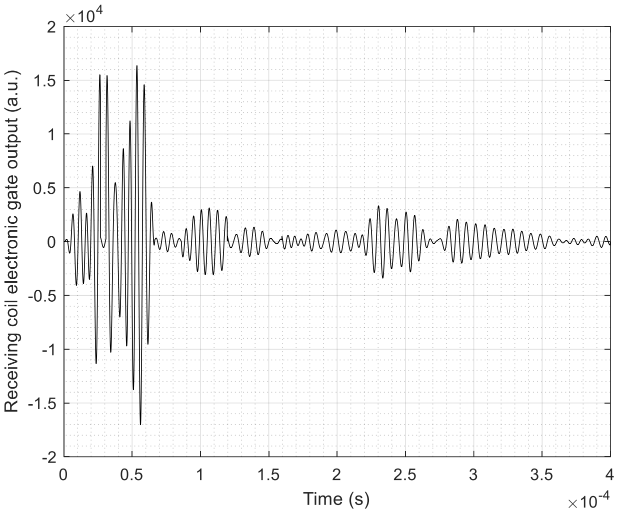

(a)

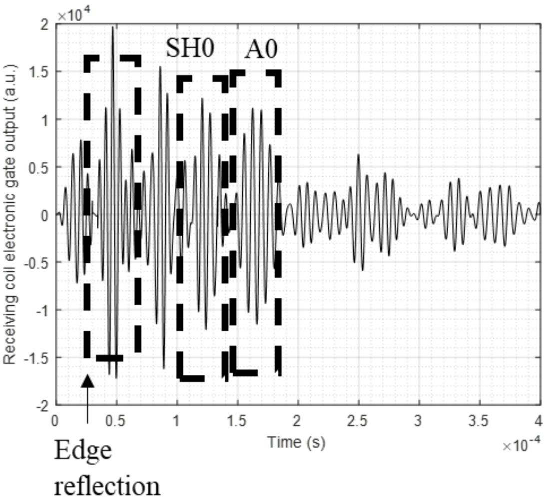

(b)

Figure 7.11. *Collected signal from the Innerspec DAQ when the transducers and the sensor are placed (a) at the far point of the linear sweep (starting point) and (b) directly opposite the defect location, showing reflected waves and the tracking gates used to select them. This data was collected using configuration 1.*

It can be seen that, in addition to the main signals, there are multiple reflections that are either scattered from the edges of the plate. In order to overcome the issue, a tracking gate was used with the aim to analyse the progression of the reflected amplitude. An initial assumption was made with regards to the defect; if the signal is reflected from the defect, the amplitude variation will be similar to the amplitude variations presented in figures 7.9 and 7.10. In the case of edge reflections, a variation of the amplitude when the sensors are performing the linear sweep will be detected as shown in figure 7.10. The electrical noise generated through the RF system and the DAQ system is assumed to remain constant during the overall test. This approach allowed the identification of the elastic waves reflected from the defect and the ones reflected from the edges and thus the waves reflected from the SH0 and the A0 are marked in the figure 7.11.

This approach allowed the enhancement of the SAFT imaging as, by identifying the relative arrival times of the reflected signal from the defect (either SH0 reflected signal or A0 reflected signal), the electronic gates of the DAQ could be placed to monitor the defect reflected signal while suppressing all other signals.

SAFT imaging was used to reconstruct the artificial defect in the CFRP plate for configurations 1-4 section and are presented in figure 7.12 for the SH0 wave mode and figure 7.13 for the A0 mode respectively. The yellow spot in the figures below represents the defect location. It is a representation of when the reflected signal from the defect is at its maximum.

As can be seen from the figure 7.12., configuration 1 provided an image of the defect with an accurate location but the shape of the defect is slightly altered. This is due to the fact that aperture of the generated elastic waves is narrow and thus the collected data didn't include information about the hidden area behind the defect with respect to the transducer. Configuration 2 generated a more complex image, probably due to the complex behaviour of the reflected waves and interference between the incident travelling wave and the reflected wave from the defect. Configuration 3 provided a more precise imaging for the defect in the Y direction (the direction of wave travel, but the amplitude of the reflection was lower. The precision was due to the fact that the configuration 3 led to the generation of a quasi-omnidirectional waves which allowed the capture of more details when performing the linear scan. Configuration 4 generated a high amplitude SH0 beam, which led to a better image than the other three configurations in both the X and Y directions.

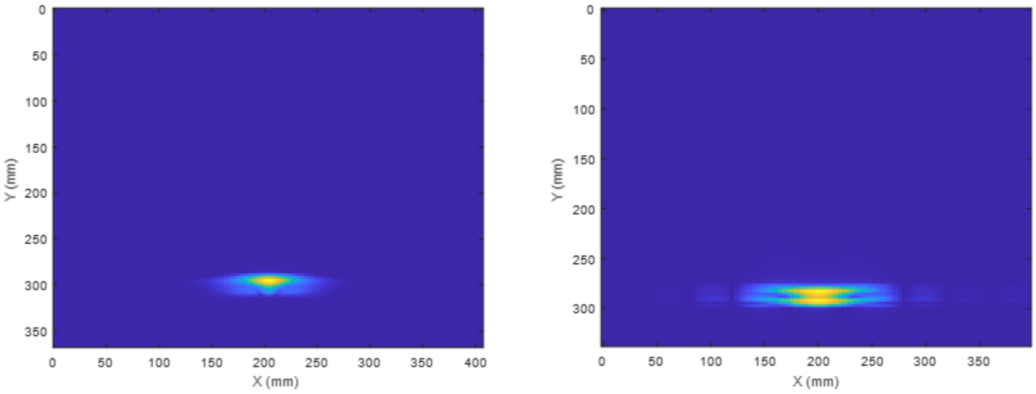

Configuration 1

Configuration 2

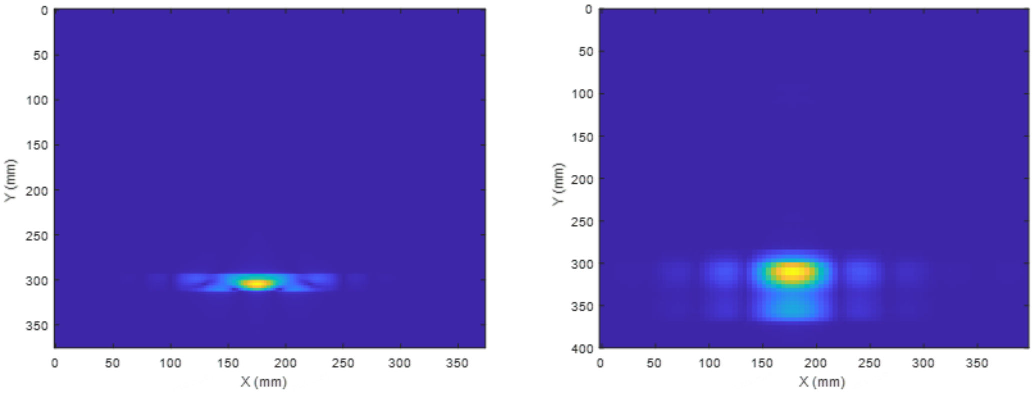

Configuration 3

Configuration 4

Figure 7.12. *SAFT images of the artificial defect in the CFRP composite plate using the reflected signal from the shear horizontal waves SH0 showing the effect of the different configurations on the reconstructed image.*

Defect images were reconstructed using the A0 mode. As can be seen from figure 7.13., using configuration 1 located the circular defect at the correct location with an estimated width of ~20 mm, close to the real dimensions. In the case of configuration 2, the image of the defect is more homogeneous compared to the defect image when SH0 mode reflect waves were used, although it is more of an elliptical shape (as was the case with configuration 3). Both configurations 1 and 2 provide a wide angular range for imaging. Configuration 4 led to a defect image, again with an elliptical shape.

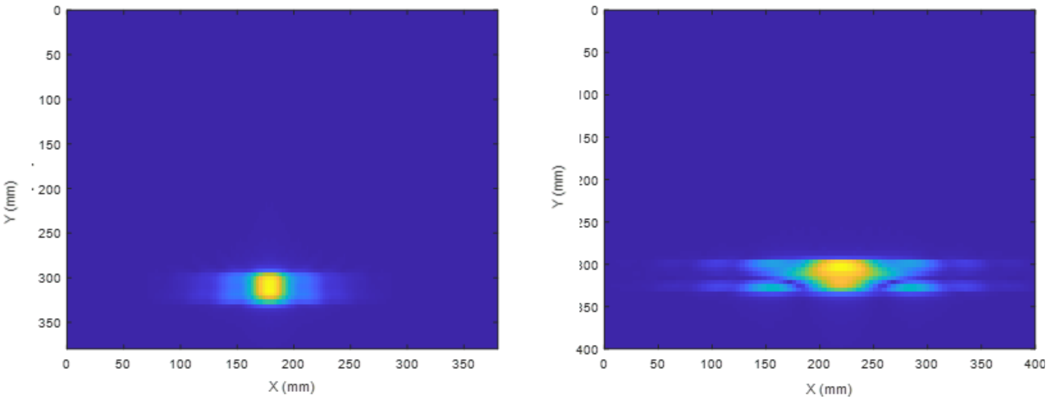

Configuration 1

Configuration 2

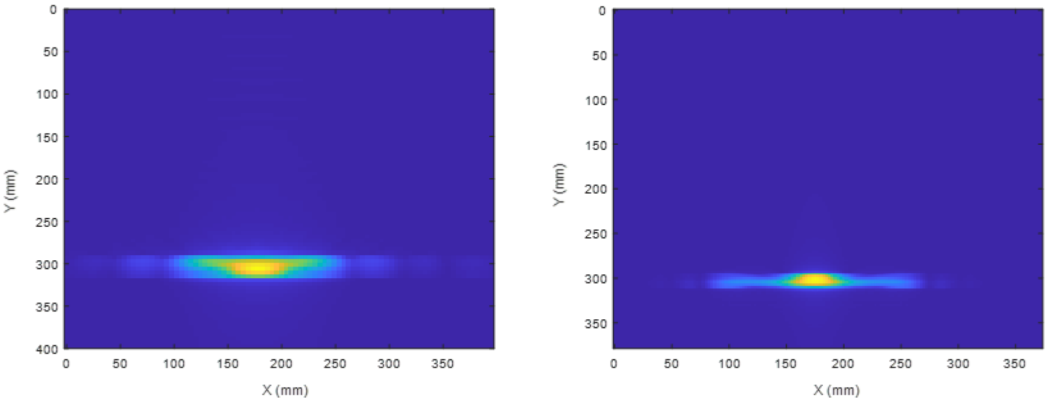

Configuration 3

Configuration 4

Figure 7.13. *SAFT images of the artificial defect in a CFRP composite plate using the reflected A0 signal, showing the effect of the different configurations on the reconstructed image.*

By using the SH0 mode and the A0 mode ultrasonic guided waves, the defect can be detected in a first instance and then to some extent, crudely imaged via SAFT. The combination of configuration 1 and the A0 mode produced a good image of the artificial defect. This specific combination is used in the next case study where an industrial GFPR including a delamination was inspected.

7.2.4. Case study: SAFT imaging for a delamination in a GFRP industrial plate

The GFRP plate sample was scanned using the transducers of configuration 1, and the SAFT image of the delamination defect, which was a square defect 70mm×25mm, present in a GFRP plate a using A0 guided waves was constructed. The signal received in two different locations is presented in the figure 7.814, where the presence of the defect is easily recognised in this much larger sample, noting that the edge reflections are not so much of a problem in this case as they are outside the temporal sampling window. In a similar way to the previous experiments, the transducer and the sensors were used to perform a linear sweep with a 2 mm spatial step size, and the reconstructed SAFT image is presented in figure 7.15 while the reflect signal is presented in figure 7.14.

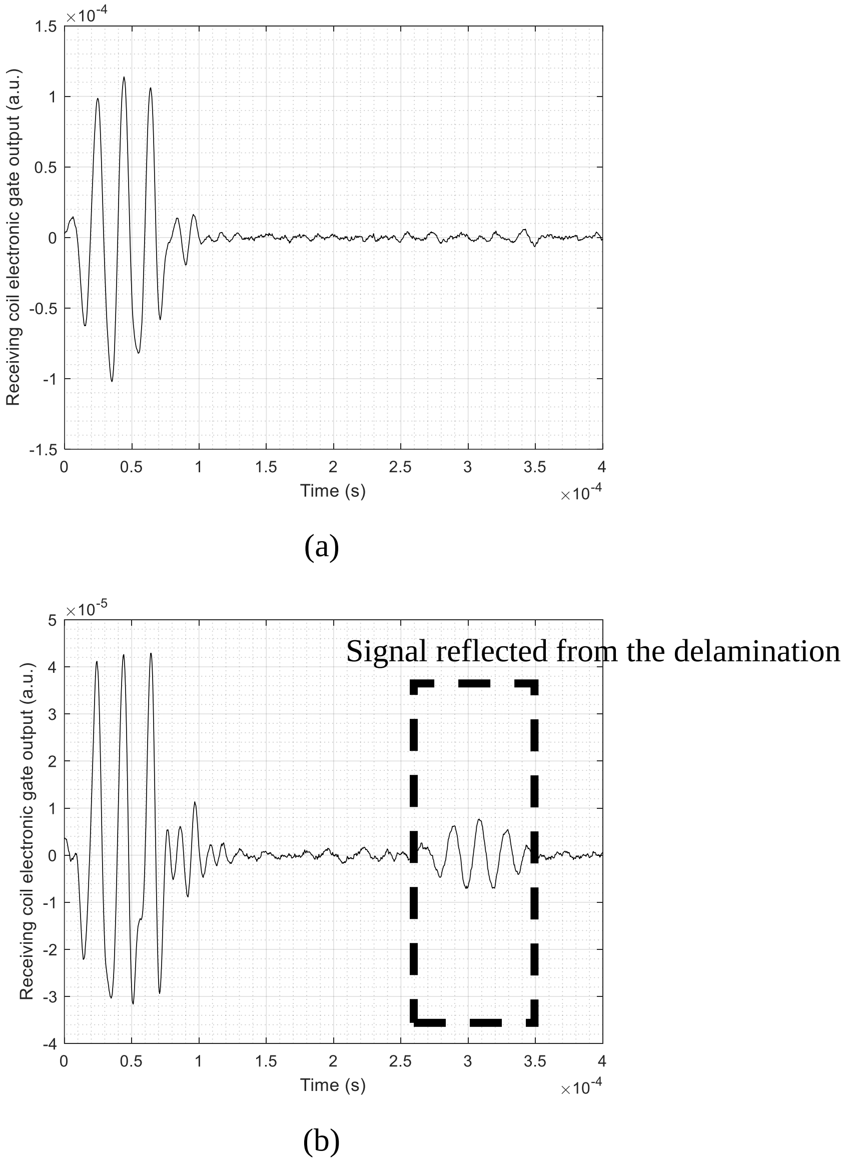

Figure 7.14. *Collected signal showing the tracking gate set for the A0 mode when the transmitter and receiver pair were placed (a) away from the location of the delamination and (b) directly in line with it.*

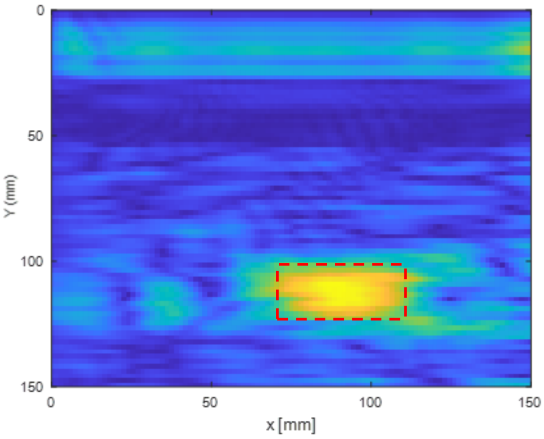

Figure 7.15. *SAFT images of the delamination defect existing in a GFRP composite plate reconstructed using the reflected signal from Configuration 1 and the A0 mode.*

As can be seen from the figure, the transducers using the magnetostrictive patches were able to provide an indicative image of the defect, and a fairly accurate location of the delamination. In fact, the location of the delamination was previously detected using commercially available systems as its location was initially unknown. The SAFT reconstruction shows that the location was identified correctly. In terms of sizing, the image shows a good agreement between the detected delamination and the real dimensions with fairly high resolution in the lateral direction (the direction parallel to the scanning direction) while lower resolution was reconstructed in the direction perpendicular to the direction of the scan. This is due to the fact that configuration 1 generated a narrow beam and the linear scans were only performed in one direction.

7.3. Discussion

Configuration 1 was seen to lead to the generation of elastic waves in a narrow and focused beam, and allowed energy to be focused into a more concentrated direction, which led to a higher level of reflected signal from a defect. In fact, when using configuration 1 to generate A0 mode, the reconstructed SAFT image for the defect was returning the highest resolution. This configuration permitted the detection of the defect when a linear scan is performed. In fact, as the SH0 mode beam is significantly directed toward the defect when aligned with the defect, the location of the defect can be more precisely identified along the X axis. In addition, the beam allowed a high imaging resolution in the same direction as the transducer linear sweep but not in the direction perpendicular to the direction of the scan. The issue was resolved when configuration 1 was used to detect the defect using the Lamb wave A0 mode. The latter combination provided a fairly optimal imagining of the defect both in the X direction and the Y direction. Configuration 2 allowed the generation of a wider beam compared to configuration 1, the detection of the defect using the linear sweep was achievable from further distances away from the defect during the linear scan. The maximum reflected amplitude is recorded when the transducer is placed in direct line with the defect. Although the defect was detectable from longer distances, the image reconstructed using the SAFT based on the propagation of SH0 mode was of complex behaviour. This is assumed to be due to the reflected signal and interference of the signal with the defect.. When switching the combination so that SAFT is used based on A0 wave and configuration 2, the reflected waves interference can be resolved leading to a defect image which is relatively elliptical. The image reconstructed returned a lower resolution imaging to the defect. Although the location of the defect can be detected using configuration 2, yet, the precise characterisation of the damage is relatively low and challenging.

Configuration 3 allowed the generation of elastic waves in a quasi-omnidirectional pattern. The elastic waves generated were propagating in quasi-circular patterns. This radiation patterns allowed the detection of the defect from a further location. The reflected signal from the defect was detected from early sweep points and the maximum amplitude was recorded in the case where the transducer is aligned with the defect. As configuration 3 generated a wide beam of elastic waves, the resolution of the defect imaging in the X direction was lower compared to the accuracy of imagining in the Y direction. This is due to the fact that in the case of wide-beam aperture, the details located behind the defect location can be captured and analysed. Configuration 3 associated with the analysis of SH0 wave modes led to the reconstruction of an image of the defect manifesting as an ellipse. Similarly, when the configuration 3 used in conjunction with the Lamb waves A0 mode, the defect is yet considered elliptical but the resolution in the Y direction is enhanced.

Configuration 4 led to the generation of fairly wide beam aperture for the generation of elastic waves in composite structure. This configuration returned the best imaging results in the case shear horizontal waves are used. The width of the aperture allowed good resolution in both X direction and Y direction. The details of the region surrounding the defect were captured with good level of precision. The configuration 4 used to generate Lamb waves A0 modes and then the SAFT method to reconstruct the defect led to a lower resolution following the Y direction.

The different elastic waves beams generated by the different configurations were mostly related to the performance of the magnetostrictive patch as most of the waves were captured at specific angles. The steering effect due to the generation of elastic waves within a CFRP plate was minimal in these measurements as the observed wave beams was similar to the radiation patterns collected in chapter 4 when the patch was applied to an isotropic non-magnetic plate. However, steering can be significant and expected in the case of using a unidirectional composite plate as then the fibres will be concentrated and aligned in specific direction which will limit the performance of the magnetostrictive patch in the direction which is perpendicular to the main direction of the fibres. In this case, the SAFT algorithm may be affected by the steering phenomenon.

In the case of the analysis shown in figure 7.8, all configurations allowed the generation of shear horizontal SH0 waves and Lamb waves A0 and S0. The distance of the travelling waves was around 200 mm for most of the configurations while maintaining a detectable level of received waves at around 10% for a 3 mm thick CFRP plate.

A delamination was used as a case study to validate the use of magnetostrictive patches to detect defects within a GFRP plate and then reconstruct the image of the defect using the SAFT technique. The flaw incorporated within the plate was detect and the SAFT provided the location and sizing of the delamination.

Throughout the thesis, there was a gradual progression in the development of magnetostrictive patch transducers by initially testing isotropic materials and analysing key parameters that may influence the ultrasonic waves generation using a magnetostrictive patch. An additional challenge was proposed within this chapter by the use of composite plates instead of isotropic plates. Composite materials are orthotropic or anisotropic materials by nature. This fact can affect the generation patterns of ultrasonic waves, especially in the case of highly-anisotropic material such as unidirectional lay-ups. The plates that were used in this work reduced the anisotropy by adopting the configuration [0º 90º 0º 90º]. The initial experiments without the defect were used to investigate the effect of the material on the generation of elastic waves. It was found that although it may limit the generation, the patch already presented specific radiation patterns at specific angles as shown in the chapter 4 and the current chapter. The magnetostrictive and Lorentz forces tended to be generated in specific directions, so that the testing was conducted at specific angles to maximize the magnitude of the generated signal. It is important to mention that in the case of unidirectional composite structures, the radiation of the generated waves may differ from the results reported in this chapter, as elastic waves will be mostly concentrated along the direction of the main fibres. In addition, the guided wave modes will be affected by the design of the composite plate being inspected as some modes can be favoured in specific direction and other modes will be attenuated in other directions. This is due to the material properties which will add an extra layer of complexity in determining the directivity of the generated waves.

7.4. Conclusions

In this chapter, a series of experiments were conducted to investigate the use of magnetostrictive patches both as a wave generation mechanism using the Joule effect and as a reflected waves detection using the Villari effect. Some of the configurations used led to the generation of Lorentz forces but these forces were not within the scope of this chapter. The main focus was to understand the capabilities of magnetostrictive forces as a transduction mechanism to generate ultrasonic guided waves in composite structures. The different configurations analysed in the previous chapters were also used to control the generation patterns of the Lamb waves A0 and S0 modes and the shear horizontal waves SH0 modes. An analysis of the wave amplitudes drops and the defect detection capabilities were presented first. These findings showed that by controlling the input parameters such as the direction and the amplitudes of the applied static magnetic field and the dynamic magnetic field, the amplitude and beam profile can be controlled.

This set of experiments used a magnetostrictive patch transducer which was attached to the structure and which may have affected the performance of the vibration of the patch. In fact, a tape was used to bond the patch to the structure. The tape is a detachable tape that would allow the patch to be removed. The bonding was performed in order to ensure good contact between the patch and the sample. It also allowed the maintaining of the contact in both the out-of-plane and the in-plane directions. As multiple guided waves were expected, contact in all directions was required. This is slightly different to the situation when a PZT is used. In fact, when wave modes with out-of-plane component are generated, a gel can be used to generate the wave while in case of shear component, a bonding material such as glue would be necessary. In the case of a magnetostrictive patch transducer, multiple modes can co-exist, as a rigidly-attached layer allows both out-of-plane motion and in-plane motion.

The use of different configurations combined with the findings from the previous chapters showed that by using each of the configurations, A0, S0 and SH0 modes can be generated and detected. This approach would allow the detection of different modes, if present, when the waves are reflected from the defect. In addition to that, the ability to generate multiple waves modes might allow the cross-referencing between the SAFT images constructed using the A0 modes and the defect image reconstructed using the SH0 wave modes.

Finally, SAFT imaging combined with magnetostrictive patch transducers showed that the defect within a composite structure can be partially characterised and more reliably detected. In fact, the flexibility offered by the variation of both the direction of applied fields and the excitation frequency proved that elastic waves can be generated using magnetostrictive patches in challenging materials such as CFRP and GFRP plates, and that images of the defects included in these structures can be reconstructed.

The use of SAFT is beneficial to assess a defect within a composite plate. Yet, due to the data collection process which is linear from a single side, the resolution in the direction of the sensor sweep was more accurate than that in the lateral direction. Further consideration needs to be given in order to provide an accurate image of what is happening behind the defect. Some of the methods to overcome such a challenge would include the use of wide-aperture transducers generating elastic waves at an angle, or by conducting an additional scan where the sweep is performed in the direction perpendicular to the original scan.

References for Chapter 7

[1] Gholizadeh, S., 2016. A review of non-destructive testing methods of composite materials. *Procedia structural integrity*, *1*, pp.50-57.

[2] Lizaranzu, M., Lario, A., Chiminelli, A. and Amenabar, I., 2015. Non-destructive testing of composite materials by means of active thermography-based tools. *Infrared Physics & Technology*, *71*, pp.113-120.

[3] Sicard, R., Goyette, J. and Zellouf, D., 2002. A SAFT algorithm for lamb wave imaging of isotropic plate-like structures. *Ultrasonics*, *39*(7), pp.487-494.

[4] Engstrand, C. and Kline, R., 2005, April. Application of SAFT to layered, anisotropic media. In *AIP Conference Proceedings* (Vol. 760, No. 1, pp. 1151-1158). American Institute of Physics.

[5] Kline, R.A., 1999. SAFT imaging in anisotropic media. In *Review of Progress in Quantitative Nondestructive Evaluation* (pp. 913-918). Springer, Boston, MA.

[6] Skjelvareid, M.H., 2012. Synthetic aperture ultrasound imaging with application to interior pipe inspection. (Doctoral dissertation, University of Tromsø).

[7] Lukomski, T., Stepinski, T. and Kowal, J., 2012. Synthetic aperture focusing technique with virtual transducer for immersion inspection of solid objects. *Insight-Non-Destructive Testing and Condition Monitoring*, *54*(11), pp.623-627.

Chapter 8: Conclusions

8.1. Key findings

The work reported in this thesis focused on delivering a deeper understanding of how the magnetostriction phenomena in thin ferromagnetic materials could be applied to NDE. Magnetostriction is a feature of ferromagnetic materials when subject to externally applied magnetic fields, and it was interesting to see whether removable patches would provide an alternative to existing methods of generating and receiving guided waves. Conventionally, piezoelectric transducers or conventional magnetostrictive patches are used to generate elastic waves in metallic and composite structures for inspection and monitoring purposes. Alternatively, EMATs offer flexibility in terms of design, and sensitivity to a particular wave mode can be controlled and enhanced. A key disadvantage of EMATs is that they only operate in the vicinity of a conductive sample, or a conducting patch applied to a non-conductive sample. CFRP plates are low conductivity samples and directly generating elastic waves through the electromagnetic transduction mechanism is challenging. MPTs were previously used to generate and detect guided waves but limited work was investigating the effect of the excitation parameters to provide a better understanding on how, by controlling those parameters, magnetostriction can be enhanced and thus generation and detection using MPTs can be improved.

The magnetostrictive patch transducers described in this thesis can be attached to the surface of a structure without altering its mechanical or chemical properties, and can be later removed. The magnets and coils used to excite these patches are similar to those used in EMATs. Here, though, the magnetostrictive patches allow these elements to perform on both conductive and insulating materials, with a reasonable sensitivity and bandwidth. Magnetostriction is a mechanism that leads to higher sensitivities than can be obtained by using a similar copper or aluminium patch in conjunction with an EMAT.

The use of the magnetostrictive patches will lead to new NDE inspection strategies, especially in composite structures. As long as the patch adheres properly to the surface, generation and detection of guided waves can occur, using changes in the coil’s dynamic field and the applied static field to optimise sensitivity to a particular guided wave mode. By improving the design of the wave generation mechanism, the cost of an inspection can be reduced, as multiple wave modes can now be generated through the use of the same system. Another pertinent point is the wide operational frequency range offered by the patches especially at lower frequencies, where piezoelectric transducers often operate across a relatively narrower frequency range due to difficulties in damping the piezoelectric element.

The thesis investigated three main features. Initially, the investigation of different magnetic field configurations was conducted to understand such an approach on the generation of elastic waves in an isotropic material. Then, a deeper analysis of the changes and their effects of the key parameters controlling the magnetostriction in ferromagnetic patches was conducted. Lastly, a magnetostrictive patch was used to generate Lamb waves and shear horizontal guided waves, to inspect two composites samples. The last task performed was to validate the findings of the previous experiments in detecting and imagining a defect within a composite structure.

8.1.1. Effect of different magnetic field configuration on magnetostriction in patches

By modifying the configuration of dynamic and the static magnetic fields, it was shown that the vibrations of a patch could be altered when it was excited by a coil and permanent magnet. The effect of four different configurations, labelled 1 – 4 was described.

- Configuration 1 had in-plane orthogonal static and dynamic magnetic fields
- Configuration 2 had the coil rotated by 90º so that the two in-plane fields were parallel to each other
- Configuration 3 had an out-of-plane static magnetic field while generating an omnidirectional in-plane dynamic magnetic field.
- Configuration 4 had an in-plane static magnetic field together with an in-plane radial dynamic field.

A set of experiments indicated that the vibration of the patch was highly dependent upon the applied magnetic field orientations. Initial findings in Chapter 4 showed that the main vibration areas were the zones directly located under the permanent magnetic and the coil. By observing the elastic waves generated in the patch soon after excitation using a vibrometer, it was shown that the vibrations in the patch were altered by changing the configuration. This indicated that the magnetic field characteristics for the chosen combination of permanent magnets and coils were dominating the response of the patch, and not the natural vibrational modes of the patch. Some configurations led to the generation of a directional beam while others had a more complicated response.

Subsequent experiments conducted within the same chapter looked at the radiation of the S0, A0 and SH0 ultrasonic guided waves. The results showed that in most configurations all modes can be generated with detectable amplitudes.

- Configuration 1 led to a complex generation pattern for S0, A0 and SH0 wave modes. Through the radiation patterns, a mode selection can be obtaining by rotating the sensor to specific angles. Although by this approach, a single mode cannot be suppressed, yet, a guided waves mode can be enhanced compared to other modes.
- Configuration 2 which is similar to configuration 1, led to the generation of a complex pattern for S0 and SH0. Nevertheless, the use of this configuration allowed the generation of quasi-directional A0 wave mode pattern. By rotating the sensor by 90º, a unidirectional, relatively high-amplitude A0 wave mode can be generated, and used for inspection purposes.
- Configuration 3 can be considered the most generic configuration in terms of A0, S0 and SH0 radiation patterns. In fact, this configuration led to the generation of omnidirectional S0, A0 and SH0 wave modes. This type of configuration can be used to run fast inspections, where the generated waves are travelling in a fairly uniform patterns in all directions.
- Configuration 4 demonstrated that a directional SH0 mode could be generated in with reasonable directionality, making it a good system for the bidirectional generation of the SH0 mode. The radiation pattern analysis showed also that the peak amplitude for the different modes can be obtained at an offset angle

to transducer for the S0 mode, while a more complex A0 mode radiation pattern can be obtained.

In practice, these observations are important, as different guided waves modes radiated at different angles can be obtained by changing the magnetic field configuration. This flexibility is rarely found in any other transducer system, as the response can be tuned to a particular dominant mode while suppressing other modes to enhance the signal-to-noise ratio. For example, an omnidirectional wave generation configuration could be used to conduct an initial scan with the aim to investigate any defects developed in proximity to the sensor. Later, in the case where a defect is detected, a more focused beam generating configuration could be used to enhance the reflected signal from the region of interest.

8.1.2. The effect of varying other parameters

The second batch of experiments described in Chapter 6 was designed to provide insights on the effect of variating the excitation frequency for different amplitudes and directions of the static and magnetic fields. This used an electromagnet, allowing the static field strength to be adjusted, and a racetrack coil to generate an in-plane dynamic magnetic field in a particular direction. It was shown that by using low amplitude fields, the magnetostriction effect was not the main driving effect for the vibration of the patch, as it was found that natural frequencies of the patch may have had an effect on the vibration amplitude. These occurred at low frequencies (90-110 kHz), which it is thought corresponded to one of the vibrational modes of the plate. By increasing the magnitude of the dynamic magnetic field, the operational range could be widened, where the particle velocities within the magnetostrictive patch are significant. In fact, these findings led to the conclusion that the patch vibrational behaviour can be controlled by modifying the input parameters, such as the excitation frequency, the amplitude and the direction of the dynamic magnetic field and the static magnetic field. A second observation was made as part of these experiments: In the case where low-amplitude orthogonal static and dynamic magnetic fields were in-plane, particle velocity amplitudes were initially higher in the direction of the dynamic magnetic field. When the magnitude of the static magnetic field was then increased, vibrational amplitudes became higher in the direction of the static magnetic field. In practice, these findings could be used to optimise the radiation of ultrasonic energy in a particular direction along a plate for NDT purposes.

8.1.3. Defect detection using different magnetic field configurations on a magnetostrictive patch transducers

The results reported in Chapter 7 of the thesis demonstrated that different configurations could be used to generate a set of guided wave modes with known directionality, and that these could be used to detect defects in both CFRP and GFRP plates using SAFT reconstruction methods. This used linear strips of magnetostrictive patch material along which a transmitter/receiver pair could be scanned. It was shown that by careful choice of the magnetic field configuration (both static and dynamic), a set of modes could be generated and reflections from defects identified. These could then be input into a SAFT reconstruction process, and images obtained. This was done for a flat-bottomed hole machined into a quasi-isotropic plate, and for a delamination defect in a CFRP plate. Both defects were identified and an image reconstructed. This needed the wave modes to be identified using their known velocities in each plate, and then their arrival time estimated and the signal for a given mode gated out from the rest of the signals in the plate. In the case of the CFRP sample, multiple edge reflections were present, but the system was able to identify the mode and reconstruct an image. The defect in the GFRP plate was also successfully imaged.

In practice, quasi-omnidirectional wave generating configurations could be used to perform a rapid linear scan to inspect wide areas. In the cases where a defect is suspected, a more focused wave generating combination could then be used to precisely identify the location of the defect. By alternating between different combinations, imaging using SAFT could be performed to produce images of the defect reflecting its size and location within the structure.

Compared to piezoelectric transducers, the use of magnetostrictive patches allows the expansion of EMAT-type techniques into the inspection of non-conducting industrial materials. These patches will offer a great alternative to existing technologies used to generate ultrasonic guided waves in composites. In fact, the use of the core components of EMATs such as the coil and the permanent magnet would lead to greater flexibility in terms of design, compared to commercially-available PZTs. In addition to that, the experiments conducted showed that by modifying the key aspects of the applied magnetic fields (dynamic magnetic field and static magnetic field) the operational range of the ferromagnetic patch can be expanded to cover a wide range of frequencies. The patches used in the thesis can be attached and removed easily without the need to use coupling agents to ensure optimum transduction efficiency.

8.2. Future work

The work conducted in the thesis offers alternative options to commercially available techniques in the NDT of composites. It could be expanded even further by an investigation into the following aspects:

(i) Different shapes of patches could be used to change directivity. For example, using patches in the form of a long thin strip would allow more directionality in certain directions. This would need the static and dynamic fields to be expanded to cover the lateral extent of the patch. Also, if the patch was in the shape of a thin arc, some focussing of guided waves might be possible

(ii) The work could be expanded to consider multiple patches, regularly spaced in the direction of guided wave travel. This could then lead to the creation of the equivalent of periodic permanent magnet (PPM) EMATs, allowing particular modes to be selected via the definition of a particular wavelength. The fact that a particular configuration could generate more than one mode could make this a very flexible NDT system.

(iii) Phased arrays could be considered, again using multiple patches and suitable drive electronics to help steer guided waves.

(iv) This work was particularly focussed on the use of guided wave for long-range NDE inspection. One area of future work could be to investigate longitudinal and shear propagation in thicker samples. Examples could be the thick GFRP composites used in ships and submarines, where low frequencies are needed for improved penetration.

Finally, the work reported within this thesis is a contribution to the current industrial practices. In fact, the use of EMATs and magnetostrictive patches is increasing within industry but they still have many challenges to address. The work conducted showed that the signal can be controlled and enhanced by modifying the input parameters which can significantly reduce the cost of inspection and offer alternative options for imaging compared to existing technologies which may be time-consuming and expensive. The work reported still requires optimization to make it suitable for an industrial environment, both at the patch level and the driving electronics level, which can also be a component of future work.